NUMERICAL SIMULATIONS AND MODELING OF EQUILIBRIUM AND
NON-EQUILIBRIUM TURBULENT FLOWS ON ROUGH SURFACES

By

Sai Chaitanya Mangavelli

A DISSERTATION

Submitted to
Michigan State University
in partial fulfillment of the requirements
for the degree of

Mechanical Engineering—Doctor of Philosophy

2024

ABSTRACT

Wall-bounded turbulent flows in many engineering applications are subjected to spatial and/or temporal acceleration and deceleration and surface roughness due to factors such as corrosion. The first part of the report aims to understand: (1) the coupled effect of roughness and mean-flow acceleration on wall-bounded turbulence and (2) to how does the turbulence response depends on the roughness topography, especially for multi-scale roughness. To that end, direct numerical simulations (DNS) are performed on periodic half-channel flows subjected to an impulse acceleration of the bulk velocity. Two different roughness topographies: a semi-uniform sand grain roughness and a multiscale turbine-blade roughness are compared with a baseline smooth-wall case. The flow developed from a transitionally rough flow at the initial equilibrium state to a fully rough flow at the new equilibrium state. Comprehensive analyses are carried out for the single-point statistics of all three components of an instantaneous flow quantity in the presence of a rough wall: the space-and-phase-average, the spatial heterogeneity of the phase-averaged perturbations (i.e. form-induced/dispersive fields), and the turbulent fluctuations. It is observed that, while the smooth-wall case undergoes a reverse transition toward the quasi-laminar state as a results of the strong acceleration, on the rough walls the reverse transition process is prevented. Instead, the turbulence near a rough wall rapidly recovers the equilibrium state, owing to an instantaneous augmentation of the form-induced perturbations as a result of the acceleration. The roughness texture plays a role in determining the rate of recovery of the near-wall turbulence to the new steady state. The effect of the form-induced perturbations on turbulence production, previously thought to be negligible for equilibrium boundary layers, is found to be significant in a strongly accelerating flow. In addition, the approximate scaling of the form-induced velocity on the velocity at the edge of roughness sublayer is identified.

In the second part of the report, the structures of both the turbulent and form-induced fields are characterized; the dynamic interactions between these two components are identified and quantitatively compared. A second mechanism through which the form-induced velocities and stresses indirectly affect the Reynolds stress isotropy through modifying pressure fluctuations is identified. The form-induced perturbations of the Reynolds stresses, rarely studied in the literature, are found to play an important role in preventing the reverse transition on rough walls. In addition, results showed that the structural response of turbulence to the acceleration on the multiscale roughness displayed similarities with that on a smooth wall: turbulent eddies are noticeably elongated in the streamwise direction, indicating local process of reverse transition even on a rough wall. Evidences suggested that this is due to strong form-induced shear, which linearly stretched the turbulent eddies instead of non-linearly modifying the eddies through augmented turbulence production.

The findings above suggest that a key part in the dependence of non-equilibrium turbulence

response on the roughness texture is the form-induced quantities, whose production is known to be attributed to the work of mean flow against the roughness pressure drag (quantified by the equivalent sandgrain height, k_s). Hence, the third part of the report focuses on analyzing and modeling the dependence of the roughness-sublayer mean-velocity profile $U(y)$ and k_s on the roughness texture, based on data-driven machine-learning approaches. Gaussian Process Regression (GPR) and Neural Networks (NN) are trained on a comprehensive database of half-channel flows over different rough surfaces consisting of new or existing numerical/experimental datasets of mean velocity profiles or k_s. Feature sensitivity analyses using both systematic selection of rough features and principal component analyses (PCA) consistently identified an optimal (minimal) set of important features for the prediction of $U(y)$, including slope, magnitude and skewness of height variations, spatial correlation, and element inclination. For $U(y)$ prediction, the GPR model is shown capable of accurate prediction for the majority of test cases with a maximum error (across y) less than 10% and a L_2 error less than 0.5%. For the k_s prediction, an existing NN method is extended to include two-point features (i.e. correlation lengths), which is shown to significantly improve the prediction. A PCA analysis showed that the majority of variation of the roughness topography in currently available datasets is mostly captured by three principal components, which depend on a set of single- and two-point features. In addition, the relatively small contribution from element inclination to the principal components indicates a need for more datasets with systematically varied roughness inclinations. These results suggest the importance of surface correlation lengths, which are not usually used in roughness modeling, in both $U(y)$ and k_s predictions. The sets of important features identified for $U(y)$ and k_s are found roughly consistent, due to similar physics (i.e. time-mean flow separation around roughness elements) determining the two quantities.

The current work provides improved understanding of the turbulence response in non-equilibrium accelerated flows on rough walls. Scaling relations (of total drag and time-mean velocity fields) of the roughness-sublayer flow are identified, which will inform future physics-based roughness models. The flow dependency on the roughness texture is characterized with machine learning techniques and state-of-the-art numerical/experimental datasets. The important roughness features that play a role in determining non-equilibrium flows response are identified for a wide range of rough surfaces, which will provide guidance on future generation of new rough surfaces for additional datasets and improve the physical understanding of individual roughness topographical features. Findings of the modeling and topography-dependency analyses of the roughness-sublayer flows carried out herein can be extended to non-equilibrium flows according to the identified scaling of RSL mean flows. Future directions are identified to complete the understanding of non-equilibrium wall turbulence in other roughness regimes and separating flows.

ACKNOWLEDGEMENTS

TABLE OF CONTENTS

LIST OF TABLES

LIST OF FIGURES

CHAPTER 1
INTRODUCTION

1.1 Background and Motivation

Turbulent flows are characterized by three-dimensional (3D), chaotic motions. Such type of flows are widely seen in applications such as blood flow, flow around turbine blades, ships and airplanes. Early studies on wall bounded turbulent flows are focused on those bounded by smooth walls. However, complications like corrosion, debris, cavities roughen the smooth surfaces. Roughness is known to affect the performance efficiency of machines. For example, the study by [5] showed a drop of 1.25% in efficiency for a Francis turbine subjected to turbulent flow. This can have a significant economical impact since the efficiency of a typical turbine is higher than 90%. As another example, [6] studied the effect of biofilm fouling for a ship relevant conditions in a boundary layer flow. The friction drag is shown to increase by more than three times compared to a similar smooth-wall flow. Efforts to smooth the surfaces are both time consuming and expensive. So, an accurate method of modeling of the roughness effects in turbulent flows is needed.

Additionally, turbulent flows in engineering applications usually displayed temporal and/or spatial variations due to external factors like pressure gradients and surface curvature. These flows are "non-equilibrium" if a similarity solution of the velocity cannot be found. It is also seen that the roughness either augmented the flow separation in APG/decelerration or acted against the stabilizing effects of FPG/acceleration on the wall-bounded turbulent flow. Moreover, these coupled effects are not well understood for multiscale roughness, requiring a detailed analysis using reliable simulations. Hence, this thesis studied the wall-bounded turbulence over multi-scale roughness subjected to temporal acceleration of mean flow using direct numerical simulations (DNS). The study aimed to develop a physical understanding of these coupled effects of roughness texture and unsteadiness in turbulence. The study also aimed at expanding this understanding to wide range of rough surfaces using data-driven machine learning techniques. This is crucial in developing models for rough-wall turbulent boundary layers and can be integrated with RANS solvers to offer a computationally inexpensive alternatives to direct numerical simulations and time consuming and expensive experiments. The current work is only applicable to rough surfaces that fall in the fully rough regime (flow pattern in the vicinity of roughness is independent of Reynolds number).

1.2 Literature Review

This section summarizes the literature on wall-bounded turbulent flows subjected to wall roughness and spatial or temporal acceleration or deceleration. First, the focus is given to the effect of roughness in a fully developed turbulent flows. Next, non-equilibrium flows over roughness are discussed, followed by a summary on strategies to treat roughness in turbulence modeling.

1.2.1 Turbulent flows over rough surfaces

To estimate the amount of hydrodynamic drag generated by roughness, [7] and [8] conducted experimental studies on turbulent pipe flow with sand papers. The results are summarized in the form of Moody diagram. Reviews of the effect of roughness on the mean flow and turbulence are given by [9], [10] and [11] in general, as well as by [12] in atmospheric applications.

The effect of the roughness on the mean velocity is as follows. The roughness alters the logarithmic velocity profile,

$$U^+ = \frac{1}{\kappa} \ln(y^+) + 5.0 - \Delta U^+, \tag{1.1}$$

where $\kappa = 0.41$ is the von Kármán constant, the subscript + denotes normalization in wall units (friction velocity, u_τ, and the viscous length scale, $\delta_\nu = \nu/u_\tau$) and ΔU^+ is the roughness function, which represents the momentum deficit (or increase of wall shear stress) due to roughness. The roughness function is dependent on the roughness Reynolds number (k^+, where k is a characteristic roughness height) and the roughness topography. The roughness Reynolds number determines the extent to which roughness affects the near-wall flow. If $k \gg \delta_\nu$ (or $k^+ \gg 1$), then k is the only important length scale near the wall. It follows that

$$\Delta U^+ = \frac{1}{\kappa} \ln(k_s^+) + C, \tag{1.2}$$

where C is the intercept of logarithmic profile and $k_s = \alpha k$ (where α is a constant) is the equivalent sandgrain height of the roughness in the limit of high k^+. k_s is defined as the height of the sandgrain roughness of [7] that would yield the same ΔU^+ as the roughness in question, which is usually very different from sandgrains. The regime of $k_s^+ \gg 1$ is referred to as the "fully rough regime", where the flow pattern around the roughness protuberances are fully developed (independent of k^+). For flows with typically $k_s^+ \in (5, 70)$, they are in the "transitionally rough regime". In this region, the roughness function is not a logarithmic function of k_s^+; it depends not only on k_s but also on δ_ν. When $k_s^+ < 5$, the flow is usually similar to that on a smooth wall. This is referred to as "hydraulically smooth regime".

The overall effect of roughness on the near wall turbulent statistics in various type of wall bounded flows are summarized below. A more isotropic Reynolds stress tensors are observed near the wall in the presence of roughness than on a smooth wall [13]. An intensification in the wall normal fluctuations (v') is seen, for example, by [14]. The roughness generally affects only the near-wall turbulent statistics upon normalizing by wall units [15; 16]. This near-wall region is known as the roughness sublayer (RSL). According to [17], the roughness sublayer ranges from 3 to $5k_s$, depending on the fluid quantity examined. Roughness weakly affects the turbulent structures outside roughness sublayer [18].

Many studies showed that the roughness effects on near-wall turbulent statistics are dependent on the roughness topography. For example, [19] studied different roughness topographies and found

that the ratio of k_s/k depends on the roughness texture. Using different roughness topographies (rod and mesh) with the same k_s, [20] showed that the topography affects turbulent energy budget and velocity spectra. [21] showed that the turbulent length scales on a 2D transverse square bars is larger than a corresponding 3D roughness. As a result, the roughness sublayer on the 2D roughness is thicker than that of the 3D one.

Most of the above studies focused on roughness made up of uniformly distributed elements. However, in realistic flows roughnesses are typically non-uniform and multiscale, including length scales that may be much larger than the boundary layer thickness. [22] showed that landscape topography and bathymetry are similar to fractal geometries, characterized by a power-law decay in the height power spectra. [23] and [24] conducted experiments on multiscale roughness in turbulent boundary layers. They both observed that the large spatial heterogeneity of the rough surfaces led to formation of secondary flows or streamwise rollers, which extended far into the boundary layer, accompanied by low and high speed regions. Detailed analysis of the dependency of the secondary flows on the spanwise spacing of roughness in wall bounded flows can be found in a large number of studies, for example, [25]. These large-scale motions are also observed by [26] in turbulence boundary layer exposed to spanwise alternating and varying height sand grit paper roughness. These time-mean, secondary motions are observed due to alternating upward and downward fluid motions around high and low roughness peaks, respectively. Turbulent length scales, Reynolds stresses, and the mean velocity showed strong spatial dependencies.

With advancement in computer processing power, rough-wall flows are studied using direct numerical simulations (DNS) and large eddy simulations (LES). DNS solves the Navier-Stokes equations resolving all the scales of motions down to the Kolmogorov scale. LES models the small scales with the help of a subgrid-scale model and resolved the scales inside and above the inertial sub-range only. The modelling of roughness in numerical studies is often done using immersed boundary (IB) method. It allows the use of a simple Cartesian grid for both the fluid and solid domains, where a localized body force ensures that the velocities at the fluid-solid interface is set to the solid velocity. Among others, [27] provided a review on the method.

Seminal numerical studies on how roughness topography influences fully developed wall-bounded flows are summarized below. The early numerical studies by [28] on square rods using DNS observed the dependency of the wall friction on the roughness topography. Further studies by [29] on 3D square and circular roughnesses revealed a strong connection between the roughness function and the wall normal turbulent velocity (v'). The study on different arrays of cube type roughness by [30] using LES showed that the arrangement affects the details of the organized turbulent motions but not the types of the motions. [31] and [32] studied influences of the roughness in a turbulent boundary layer. The roughness significantly affected the shape of near-wall streaky motions by shortening the length of low-speed streaks. One characteristic effect of roughness is to

3

reduce the integral length scale in the streamwise direction. [33] confirmed this observation in a turbulent boundary layer subjected to realistic (turbine-blade) roughness. Also, they showed that the roughness led to a transfer of energy from large scales to small scales via redistribution of turbulent kinetic energy (TKE), defined as sum of the kinetic energies of turbulent motions in all three directions. Using DNS of turbulent channel flows, [34] compared uniform sand grain roughness and multiscale turbine-blade roughness and observed the dependency of conditionally averaged turbulence motions on the roughness topography. The large wavelengths in multiscale roughness induced large quasi-streamwise vortices that shared similarities to those on a smooth wall. [35] studied a turbulent channel flow with a random roughness. Analysis of the right-hand-side of the turbulent pressure Poisson equation showed the dominance of the 12 component of the rapid source term around the roughness peak and the 23 component of slow term at the roughness trough. These terms are considered to arise due to the shear layer and quasi-streamwise vortices, respectively. This gave an insight into the flow features that are responsible for the pressure fluctuations, which contributes to TKE redistribution and the Reynolds stress anisotropy.

In the roughness sublayer, the presence of roughness leads to spatial heterogeneity in the time- or ensemble-averaged variables of the turbulent flows. [36] introduced a double average (DA) decomposition to separate the mean-flow spatial heterogeneity from the turbulent fluctuations. The variable representing this heterogeneity in the velocity is referred to as the "dispersive" or "form-induced" field. The work of pressure drag against the mean velocity is considered the main source of this field. The alteration of near-wall turbulence behavior in the presence of roughness can be partially attributed to the form-induced velocities, which introduced additional turbulent-kinetic-energy (TKE) production mechanisms [36; 37; 38]. Earlier observations of the form-induced velocities are made by [39]. DNS on uniform cubical-type roughness showed dominance of the form-induced stresses over the Reynolds stresses near the roughness. The strength of the fields is shown to be dependent on the roughness topography [40]. Despite earlier observation that the form-induced TKE production is negligible [41], [40] showed that the two components of the total production (the part due to Reynolds stress, P_m, and that due to dispersive stress, P_w) are individually significant, though their sum may be small in the canonical flows tested. It remains unclear, however, whether in non-canonical flows such as non-equilibrium wall turbulence, the turbulence production by form-induced velocities can still be ignored.

1.2.2 Non-equilibrium turbulent flows

Current understanding on non-equilibrium wall bounded flows over smooth and rough-walls is summarized below. Both spatially and temporally developing flows will be discussed.

1.2.2.1 Smooth-wall flows

Non-equilibrium spatially developing turbulence are summarized below. First, the focus is given to accelerating flows (or those with favorable pressure gradients, FPGs). Early studies showed that

4

the smooth-wall flow underwent a reverse transition toward a quasi-laminar state due to a delay in the response of Reynolds stresses to the mean-flow acceleration [42]. The friction coefficient value and mean velocity profiles may revert to a laminar-like state. [43] conducted experimental studies on a flat-plate boundary layer with FPG and observed a reduction in the wall-normal momentum transfer in the quasi-laminar state. This is associated with the sweep events (fourth quadrant) being replaced by the third quadrant events. Numerical simulations of a spatially developing boundary layer by [44] show dampening of p' fluctuations and subsequent reduction in TKE redistribution in the quasi-laminar flow. Elongation and stabilization of near-wall streamwise velocity streaks and vortices are also observed as a consequence of lower energy transfer from u' to v' and w' velocity components [45; 46]. In addition, the increase in streamwise and spanwise extents of near-wall turbulent structures relative to the boundary layer thickness is observed by [47] for a turbulent boundary layer subjected to FPG. The flow recovered quickly once the FPG is removed. On the other hand, adverse pressure gradient (APG) or free-stream deceleration may lead to reduction in the wall shear stress and subsequent separation of the flow [48; 49; 50; 51]. In the outer layer, APG energizes the large-scale structures unlike FPG flows (where the outer-layer response lags behind the near-wall one) [52; 53]. Similarly, for high-Re, APG turbulent boundary layers, APG is shown to enhance both the small-scale and large-scale energy containing structures in the outer layer.[54].

Compared to boundary layer flows subjected to spatial acceleration/deceleration, temporally accelerated/decelerated flows share some common features, when viewed using the concept of the equivalent convection velocity [55]. For example, [56] studied the response of a transient channel to an impulse acceleration. The flow underwent a process similar to the reverse transition toward the quasi-laminar state in a spatially developing flow. Various phases are identified. The initial phase is characterized by a decrease of friction coefficient and long streaky structures near the wall. As the flow recovered, turbulence spots are formed near the wall, which disturbed the stability of long streaks and eventually merged and established a new steady state.

1.2.2.2 Rough-wall flows

Studies of rough-wall spatially accelerating flows showed that the roughness acts against the effects of FPG on the turbulence. The experimental study by [57] on rough-wall quasi-equilibrium boundary layers subjected to mild acceleration showed intensified turbulent intensity around roughness elements, which prevented the reverse transition as seen in smooth wall. [44] and [58] studied flat-plate boundary layers with sand grain roughness exposed to spatial acceleration. The more isotropic Reynolds stress tensor in the presence of roughness is found, attributed to the additional production mechanisms due to the form-induced fields. Similar flow responses are seen in temporally accelerated flows by [59], who studied a periodic channel in response to an impulse acceleration with a pyramid-type roughness. The rough wall prevented the reverse transition. The long streaky velocity structures are replaced by strong counter rotating hairpin vortices around

roughness elements. These vortices subsequently break down, in a rapid transition to a new equilibrium state. This behavior is similar to roughness-induced laminar to turbulent transition. The additional TKE production mechanisms due to the form-induced fields are also studied by [60] and [61] in oscillatory channel flows with rough walls. The magnitude of the TKE production is shown to be dependent on the roughness size and the phase of the oscillatory flow and could reach significant values, unlike in canonical flows (e.g. fully developed channels) where the production is found negligible. Recent experimental study of a 2D cylindrical rod roughness subjected to wall suction is done by [62]. A downward shift of the velocity profile in the outer part of boundary layer is observed. This aided the shedding of the roughness-induced vortical structures and hence prevented the quasi-laminarization. The effect of sand grain roughness on turbulent boundary layers subjected to APG are studied by [51]. The roughness is shown to lead to an earlier separation and a larger separation bubble due to a higher momentum deficit.

From the above review, it is established that the roughness counteracts the FPG effects and, to some extent, augments the APG effects in wall bounded flows. However, this understanding is generally limited to distributed roughness elements of the same geometry or a narrow length-scale range. It is not clear how would turbulence respond to mean-flow acceleration/deceleration (in either space or time) on a multiscale roughness. Also, the coupling of the effects of roughness and unsteadiness on turbulence is not well understood. Physical knowledge of this kind is crucial for modeling of non-equilibrium turbulence bounded by realistic roughness.

1.2.3 Modelling of rough-wall flows

Often, roughness is not resolved in engineering predictions, since it is small compared to the length scale of the problem. Commercial codes used in practice often rely on Reynolds-averaged Navier-Stokes (RANS) simulations and incorporate a one- or two-equation eddy-viscosity models. The Reynolds stress tensor in the RANS equation requires closure. The approach of the eddy-viscosity models is to model the Reynolds stress tensor as a function of mean velocity with the help of an eddy viscosity. In the fully rough regime, the hydrodynamic drag is dependent only on a single parameter of roughness (k_s). Existing roughness closures in RANS models usually involve modifying the turbulent scales at the wall based on calibrated functions of the local k_s^+ value.

A major focus of engineering roughness modeling is on the prediction of k_s based on features of the roughness texture alone (and not on flow quantities). k_s depends on not a single geometrical property of surface roughness, but on a collection of different properties. For example, [19] studied the dependence of k_s on the root mean square (rms) and skewness of the roughness height fluctuations. In addition, the dependency on the "effective slope" (i.e. the mean slope magnitude of the surface) is studied by [63] and [64], among others. [65] performed DNS of sinusoidal roughnesses in a pipe flow. The roughness function is shown to be dependent on both the effective slope and average height of roughness. Another study by [66] explored the dependency on three

6

different areas of roughness elements (total roughness reference area, frontal area and windward wetted surface area). In addition, [64], among others, showed that the separation between the fully and transitionally rough regimes is also topography dependent. The DNS by [67] on irregular rough surfaces in the transitionally rough regime showed a dependency of the roughness function on the rms of roughness height, frontal area ratio, skewness, and streamwise correlation length. Readers are referred to [68] for a comprehensive review of the dependency of drag on roughness topography for turbulent flow on canonical, rigid roughness. [69] also offered a comprehensive summary on the dependency of k_s on roughness features. The study concluded that measures of size, frontal area and coverage of roughness as minimum independent parameters required for its prediction. However, even for the fully rough regime alone, there is no universal prediction of k_s for arbitrary surface topographies.

With the advancement in the processing powers, it is now possible to develop more universal k_s models with the help of Machine Learning (ML). [4] trained Deep Neural Networks and Gaussian Process Regression model to predict k_s based on $o(10)$ geometrical features for 45 different rough surfaces. [70] trained Convolutional Neural Networks to predict momentum and heat transfer, by employing a visual mapping between height distribution of rough surfaces and local skin friction and Nusselt Number. 80 grit blasted rough surfaces are generated using DNS at $Re_\tau = 180$. The trained algorithm predicted the skin friction and Nusselt number with maximum errors up to 8.1% and 2.9%, respectively.

Some alternative approaches are also proposed to model the roughness effects on the mean flow and turbulence. [71] offered a comprehensive review of modelling the force term using discrete element approach. This force term is prescribed to be proportional to the square of double-averaged mean velocity in the fully rough regime. Furthermore, the proportionality constant is a function of k_s^+ and wall-normal distance. [72] modeled the roughness effects using an external forcing term related to the roughness height and the density of element distribution. Other alternate approaches include the following. [73] performed DNS of turbulent channel flow on a hexagonally packed hemispherical roughness. The observed interactions between the large-scale outer layer structures and the near-wall small scale fluctuations are used to build a model of the roughness effects on the near-wall, higher-order statistics of velocity fluctuations. [74] proposed an approach that explicitly modeled the geometry of the roughness wake. The model allowed accurate prediction of the drag over a cuboidal roughness. Recent study by [75] over a few different rough surfaces developed a data-informed wall function of velocity inside the roughness sublayer, to be used for equilibrium and non-equilibrium flow RANS models when the roughness layer is resolved.

However, large uncertainties are observed when the roughness closures, typically developed for equilibrium flows, are used for non-equilibrium turbulence. [76] compared various RANS closures with or without wall functions for a strongly accelerating boundary layer with roughness. The wall

functions (without a resolved wall region) are found to perform poorly, while closures that resolved the wall region gave considerable discrepancies from the DNS results. [77] showed the failure of engineering turbulence models in predicting the flow separation induced by adverse pressure gradients and reverse transition induced by favorable pressure gradients. Furthermore, the utility of k_s is limited to equilibrium wall turbulence where a logarithmic velocity layer is present and is characterized by a slope similar to the smooth-wall value. In non-equilibrium flows such as those with pressure gradients, the logarithmic layer varies or becomes non-existent and, consequently, k_s cannot be defined [78]. Additionally, [78] questioned the existence of outer-layer similarity in non-equilibrium flows with evidences from past literature supporting both sides of the argument. The outer-layer similarity states that the roughness affects the near-wall region only. If it does not apply, modeling of outer-layer effect of roughness would be needed in addition to modeling of the friction velocity or the near-wall flows. Furthermore, even though an accurate k_s model can be built, it may yield accurate wall shear stress but does not guarantee an accurate prediction of mean velocity in the roughness sublayer (RSL), which would have significance in, for example, prediction of the separation point in strong-APG flows where a correct prediction of the RSL mean velocity is important.

An alternative approach of roughness modeling is to model the RSL mean-velocity profile, coupled with a RANS closure above the RSL. An example is the approach of [75]. [75] proposed a composite $U(y)$ model inside the RSL. The model consists a zero-velocity zone in the vicinity of the wall and a upper zone that blends the lower zone with the outer layer based on a cubic polynomial. The model is calibrated for four different rough surfaces in an open channel flow and shown to reproduce well the mean velocity profiles. An advantage of the model is that a logarithmic layer is not required, allowing it to be used in non-equilibrium flows. However, it is not clear how the mean velocity profile varies as a function of roughness texture, limiting the application of this model.

One objective of the modeling portion of this thesis is to extend the RSL $U(y)$ modeling to a significantly wider range of rough surfaces, based on machine learning (ML). This type of RSL modeling not only provides a potential approach for modeling non-equilibrium turbulent boundary layers, but also allows investigation of the dependencies of the RSL mean flow on various roughness characteristics. This is of interest for understanding (1) form-induced stress production (as the mean velocity contribute to one major source term) and (2) momentum and heat/mass transport within RSL, which is important for, for example, environmental flows including those within urban or aquatic canopies. Another objective is to extend the deep neural network used by [4] to a wider range of rough surfaces covering bar-type roughness, pitty surfaces (with negative skewness of height fluctuations), among others.

1.3 Research objectives and outline

The above mentioned limitations of the state-of-art understanding of non-equilibrium rough-wall turbulence prompted the following research objectives.

1. Identify how roughness and its different textures influence the wall turbulence response to a mean-flow acceleration, as an example of non-equilibrium boundary layers.

2. Perform detailed analyses of both the turbulent and the form-induced components of the velocity in the non-equilibrium accelerating turbulence.

3. Based on the physical insights learned above, propose data-driven (machine learning) models of the roughness sublayer, with a secondary objective to identify the roughness geometrical features that are most important in influencing the turbulent response.

Roughness-resolved DNS will be used to provide datasets for both the fundamental analyses and modeling. Periodic half-channel flows, either fully developed or transient accelerated, are used. Aspects of the transient flows are similar to spatially-developing boundary layers, to which the transient flows may be considered as a computationally low-cost alternative. In addition, the use of periodic half-channel flows allows the inclusion of multiscale roughness with length scales much larger than the boundary layer thickness, up to the channel length/width. The rest of the thesis is outlined as follows.

1. In Chapter 2, DNS of half-channel flows in response to an abrupt increase in the bulk velocity is studied. The simulation methodologies are described. Two different roughnesses are imposed on the wall. Comprehensive analyses are carried out for single-point statistics of all three components of an instantaneous flow quantity in the presence of a rough wall: the space-and-phase average, the spatial heterogeneity of the phase-averaged perturbations (i.e. form-induced field), and the turbulent fluctuations. The ways how the turbulence response (to acceleration) is affected by the roughness texture are identified. In addition, RSL-flow and drag scalings are examined, to provide insights in drag and velocity modeling in roughness-unresolved predictions.

2. Chapter 3 identifies the importance of the form-induced fields ($\widetilde{u}_i$) in non-equilibrium accelerated turbulence. This motivated a detailed study in Chapter 3 on other ways how $\widetilde{u}_i$ may dynamically affect the turbulence structure and other mechanisms important in Reynolds stress transport (including production of pressure fluctuations and TKE redistribution), besides the additional TKE production well studied in the literature.

3. The previous chapters establish the importance of the form-induced velocity in affecting the mean flow and turbulence response in non-equilibrium wall-bounded flows. Recall that a main component of the production of form-induced kinetic energy is the work of mean flow $U(y)$ against the pressure drag (representative by k_s) [38]. Hence, one motivation of Chapter 4 is to identify the dependencies of the RSL $U(y)$ and k_s on various roughness

9

features. In addition, ML models of the two quantities are developed based on a state-of-the-art rough-wall-flow database to model the RSL $U(y)$ and k_s for a wide collection of surfaces. Machine learning techniques such as principal component analysis (PCA), Gaussian Process Regression (GPR) and Deep Neural Network (DNN) are used, along with systematic feature elimination studies, to identify the most important roughness features for RSL $U(y)$ and k_s, as well as to predict these quantities.

4. Chapter 5 summaries the findings of the thesis, followed by proposed areas of future work.

CHAPTER 2
EFFECTS OF SURFACE ROUGHNESS TOPOGRAPHY IN SINGLE POINT STATISTICS OF TRANSIENT CHANNEL FLOWS

2.1 Introduction

This chapter of the thesis will be also referenced in the text as [2]. Wall roughness plays an important role in many engineering and environmental applications and a large body of work had been carried out to gain understanding of the dynamics of turbulent flows over rough walls. In addition, wall-bounded flows are often subjected to external disturbances such as freestream pressure gradients and unsteadiness, some of which have been studied extensively. Reviews of the literature in these topics are provided in Chapter 1.

Many aspects of turbulent flows in the vicinity of walls with different kinds of roughness have been examined. However, understandings are generally limited to effects of roughness in equilibrium wall turbulence (e.g. fully developed, steady channels and ZPG boundary layers). The effects in time- and/or space-varying flows have received limited attention. This study focused on an important transient-flow phenomenon—the suppression of quasi-laminarization by surface roughness—with emphasis on the role played by the roughness geometry. To this end, we characterized the response of wall-bounded turbulence to an abrupt mean-flow acceleration in a channel flow, using a configuration similar to that of [59]. Unlike a spatially accelerating boundary layer, where the roughness wavelengths are constrained by the length scale of the mean velocity variation, a transient channel-flow simulation can accommodate roughness wavelengths as long as the channel itself, because of the use of a periodic streamwise boundary condition.

Direct numerical simulations are conducted in transient half-height channel flows, in which abrupt increases in mass flow rate are imposed on an initially steady-state flow. The behavior of turbulent flow over two surfaces with different roughnesses is compared to that in the baseline case of smooth-wall flow. In this chapter, Sec. 3.2 introduced the governing equations and details of the numerical solution, roughness geometries, and simulation parameters. Section 3.4 compared the results of the smooth-wall and the two rough-wall cases for both the initial steady state (before the transient started, Sec. 2.3.1) and the recovery after the transient is imposed. Transient flow comparisons are carried out for the mean velocity (Sec. 2.3.2), form-induced velocities (Sec. 2.3.3), the Reynolds stresses (Sec. 2.3.4), and the Reynolds stress budgets (Sec. 2.3.5).

2.2 Methodology

2.2.1 Governing equations

The incompressible flow of a Newtonian fluid is governed by the equations of conservation of mass and momentum:

$$\frac{\partial u_i}{\partial x_i} = 0, \tag{2.1}$$

$$\frac{\partial u_j}{\partial t} + \frac{\partial u_i u_j}{\partial x_i} = -\frac{\partial P}{\partial x_j} + \nu \nabla^2 u_j + F_j, \tag{2.2}$$

where: x_1, x_2 and x_3 (or x, y and z) are, respectively, the streamwise, wall-normal and spanwise directions, and u_j (or u, v and w) are the velocity components in those directions; $P = p/\rho$ is the modified pressure, ρ the density and ν the kinematic viscosity. The term F_j in Equation (2.2) is a body force of the immersed boundary (IB) method used to impose non-slip/penetration boundary conditions at the rough surface, which is well-resolved by the grid. The method is based on the volume-of-fluid approach [1]; its detailed implementation in the in-house fluid solver and validation are described in [38] and [79]. Specifically, the volume fraction occupied by the fluid $\phi(x, y, z)$ in each grid cell is calculated during pre-processing. It is used to calculate the force $F_1(x, y, z, t)$ at each time step, to decrease the momentum in each grid cell by a fraction of $(1 - \phi)$. The F_1 values are non-negligible in the boundary cells of roughness, and are negligible elsewhere. The simulations are performed using a well-validated code that solved the governing equations (2.1) and (2.2) on a staggered grid using second-order central differences for all terms, second-order accurate Adams-Bashforth semi-implicit time advancement, and MPI parallelization [80].

In the roughness sublayer, the presence of roughness elements led to spatial heterogeneity in ensemble-averaged variables. Such heterogeneity is separated from turbulent fluctuations using a double-averaging (DA) decomposition [36],

$$\theta(x, y, z, t) = \langle \overline{\theta} \rangle (y, t) + \widetilde{\overline{\theta}}(x, y, z, t) + \theta'(x, y, z, t), \tag{2.3}$$

where θ is a local, instantaneous flow variable, $\langle \theta \rangle$ is the intrinsic spatial average in the (x, z)-plane, $\langle \theta \rangle (y, t) = 1/A_f \int_{A_f} \theta \, dA$ (where A_f is the area occupied by fluid at elevation y), $\overline{\theta}$ denoted the ensemble average (the 'mean' component), $\theta' = \theta - \overline{\theta}$ is the turbulent fluctuation from $\overline{\theta}$, and $\widetilde{\overline{\theta}} = \overline{\theta} - \langle \overline{\theta} \rangle$ is the dispersive (or form-induced) fluctuation. A superficial spatial averaging is also used; it is defined as $\langle \overline{\theta} \rangle_s (y, t) = 1/A_f \int_{A_o} \theta \, dA$, where $A_o = L_x L_z$ is the total horizontal area of the simulation domain and L_{x_i} is the domain size in x_i.

The streamwise component of the IBM body force, $F_1(x, y, z, t)$, can be integrated in the wall-normal direction to yield the total hydrodynamic drag at a (x, z) location and a time t, including both viscous and pressure drags. The wall shear stress τ_w is then calculated as the ensemble-averaged

12

total drag per domain horizontal area:

$$\tau_w(t) = \frac{\rho}{L_x L_z} \int_{\mathcal{V}} \overline{F}_1(x, y, z, t) \, dx \, dy \, dz, \tag{2.4}$$

where $\mathcal{V}$ represented the volume of the simulation domain. The friction velocity is then obtained as $u_\tau(t) = \sqrt{\tau_w/\rho}$. This method of τ_w calculation is validated by [38] in a fully developed channel flow over sandgrain roughness by comparing with the total drag calculated from the mean momentum balance.

2.2.2 Rough surfaces
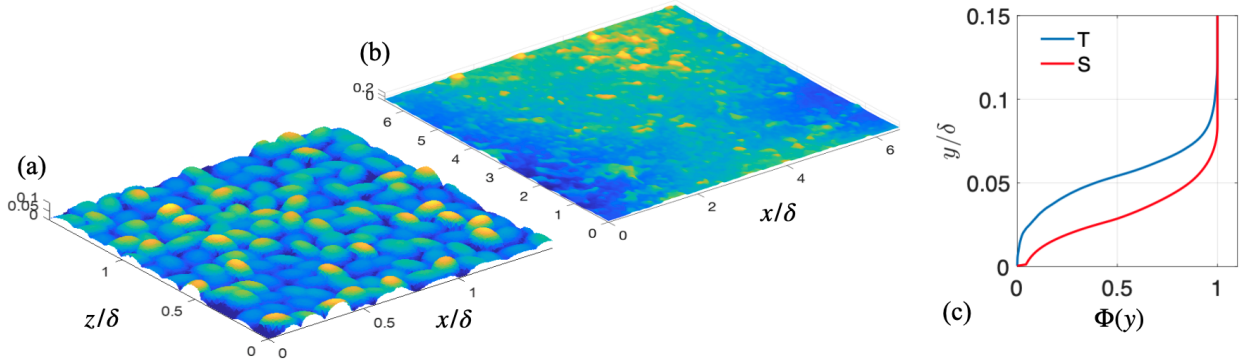
Figure 2.1 A fraction of sandgrain (a, case S) and turbine-blade (b, case T) rough surfaces colored by height. (c) Variation of roughness geometry functions along y.

Two quite different surfaces roughnesses are considered: one synthetic sandgrain roughness 'S' (Fig. 2.1a), and one replicated from a surface scan on a hydraulic turbine blade 'T' (Fig. 2.1b). Flow over these two surfaces is studied in fully-developed half-height channels by [40], who compared details of their surface-geometric parameters.

Figure 2.1(c) compared the roughness geometry functions between the two roughnesses. It increased with y and reached its maximum value of 1 at $y = k_c$. The power spectrum and the probability density functions (PDFs) of local surface height fluctuations $k(x, z) - \langle k(x, z) \rangle_o$ are compared in Fig. 2.2. Here, operator $\langle \cdot \rangle_o$ denoted averaging across the wall-parallel plane. The 'sandgrain roughness' surface S is created as a uniform distribution of randomly oriented ellipsoids of the same geometry [1]. Its roughness height distribution is characterized by dominant wavelengths much smaller than the channel half-height δ; the spectral decay occured only for scales smaller than the grain size. In contrast, surface T yielded an approximate power-law decay of the power spectrum with a slope of -2, indicating similarity to a fractal geometry. The initial turbine roughness scan is mirrored in both x and z to produce the final T surface that satisfied periodic boundary conditions in x and z. When these roughness height distributions are compared with δ, surface S may be considered a homogeneous roughness, whereas surface T is heterogeneous (with important features at scales larger than δ). The PDFs of height fluctuations show that both

13

roughness geometries are characterized by rather evenly distributed height values with respect to the average height. Case S shows slight bias toward lower height values.
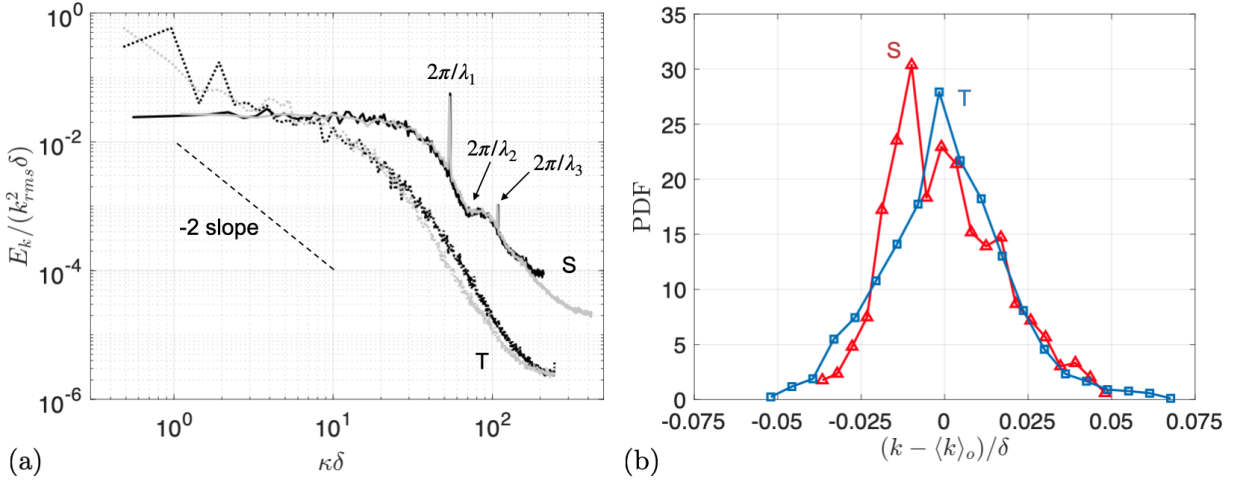
Figure 2.2 (a) Power spectrum of surface height fluctuations in cases S (——) and T (···) with wavenumbers κ in x (black) and z (grey). For S, λ_1, λ_2 and λ_3 are the three semiaxes of an ellipsoid grain [1]. (b) PDFs of surface height fluctuations for cases S and T; normalization is done such that area below curve is one.

Surface	R_a/δ	k_c/δ	k_{rms}/R_a	s_k	k_u	ES_x	ES_z	$(L_x, L_z)/\delta$
SM	0	0	0	0	0	0	0	(12, 6)
S	0.014	0.09	1.05	0.48	2.97	0.43	0.44	(12, 6)
T	0.014	0.13	1.17	0.20	3.49	0.10	0.08	(12, 12)

Table 2.1 Geometrical parameters of the sandgrain (S), turbine roughness (T) and the smooth wall (SM). δ is channel half height; Ra is first-order moment of height fluctuations; k_c is maximum peak-to-trough height (crest height); k_{rms}, s_k and k_u are the root-mean-square, skewness and kurtosis of height fluctuations; ES_{x_i} is the effective slope in x_i; L_{x_i} is the domain size in x_i.

Geometrical parameters of the two surface roughnesses are compared in Table. 3.2. Both surfaces shared the same first-order moment of height statistics (R_a), and have very similar (with 10% difference) RMS roughness heights (k_{rms}), but quite different values of maximum peak-to-trough height (k_c, also called crest height), skewness (s_k) and effective slope (ES) in x or z. $k_c/\delta \leq 0.13$ for both cases. A smooth-wall baseline case 'SM' is used for purposes of comparison.

2.2.3 Simulation Parameters

Simulation parameters for all cases are listed in Tables 2.2 and 2.3. The initial and final steady states are denoted using subscripts '0' and '1', respectively. Parameters such as the Reynolds numbers and roughness crest heights are chosen to ensure that the transient and the final states of each flow corresponded to the Reynolds-number-independent fully rough regime of flow for both rough surfaces. The final steady state is reached at different times for different flow statistics; after the steady state is reached, the value of a flow quantity does not vary in time any more. Note that during the transient some quantities cross the final steady-state values before the steady state

14

is reached; these quantities include the frictional coefficient, dispersive stresses, and streamwise Reynolds stress, among others.

Surface	Re_{b0}	$Re_{\tau 0}$	Ra/δ	k_c/δ	$k_{s,\infty}^+$	$(\Delta x^+, \Delta y_{min}^+, \Delta z^+)$
SM	4,000	244	0	0	0	(4.0, 0.9, 2.0)
S	4,000	320	0.019	0.08	21	(5.0, 1.2, 2.5)
T	4,000	294	0.019	0.12	10	(3.4, 1.1, 3.4)

Table 2.2 Simulation parameters in the initial steady state (denoted by subscript '0'). Superscribe '+' indicates normalization by wall units (u_τ and viscous length scale $\delta_\nu = \nu/u_\tau$).

Surface	Re_{b1}	$Re_{\tau 1}$	Ra/δ	k_c/δ	$k_{s,\infty}^+$	$(\Delta x^+, \Delta y_{min}^+, \Delta z^+)$
SM	12,000	626	0	0	0	(9.8, 2.3, 4.8)
S	12,000	1023	0.019	0.08	76	(15.3, 3.7, 7.6)
T	12,000	858	0.019	0.12	23	(10.1, 3.3, 10.1)

Table 2.3 Simulation parameters in the final steady state (denoted by subscript '1').

Here, $k_{s,\infty}$ is the corresponding equivalent Nikuradse sandgrain height in the fully rough regime, defined by [10]. The values of $k_{s,\infty}^+$ in Tables 2.2 and 2.3 for both surfaces are deduced from the ratio $k_{s,\infty}/k_c$ determined in the study of [64], where a Reynolds number sweep is performed for each surface to identify the critical roughness Reynolds number $k_{s,cri}^+$ corresponding to the lower limit of the fully rough regime. In the final steady state, the values of $k_{s,\infty}^+$ are 76 and 23, for S and T respectively, while the respective values of $k_{s,cri}^+$ are found to be 60 and 20 [64]—lower than the steady-state values of $k_{s,\infty}^+$—indicating that fully-rough flow had been achieved. Considering that both rough surfaces share the same value of Ra and slightly different Re_τ, the observation that case S yields a much higher value of $k_{s,\infty}^+$ indicated that it generates significantly more hydrodynamic drag than case T.

The domain sizes in x and z are $(12\delta, 6\delta)$ for cases SM and S, and $(12\delta, 12\delta)$ for case T. For case T, a larger spanwise domain is required to accommodate larger spanwise roughness wavelengths. For all cases, L_x are chosen similar to that used by [56] for a similar smooth-wall transient flow setup. In the study by [56], a similar u_{b1}/u_{b0} ratio of 2.6 is used, but the Reynolds numbers is much lower ($Re_b = 2825$ compared to 7404 herein). They found that $L_x/\delta \approx 12$ is sufficient for accommodating large-scale motions according to the two-point velocity correlations. For the rough cases, the near-wall u_i' coherence lengths are expected to be shorter than on a smooth wall. It is validated for cases S and T that the two-point correlation of u' at streamwise separation of a half of the domain size falls below 0.1 at $y/\delta = 0.3$ for all t^*.

The numbers of grid points are $(768, 273, 768)$, $(768, 263, 768)$ and $(1024, 259, 1024)$ in (x, y, z) for cases SM, S and T, respectively. The mesh is uniform in x and z while refined near the wall in y. At the final steady state (the more critical one for spatial resolution between the two steady states), $\Delta y_{min} < 0.3$ for SM and Δy^+ falls between 0.6 and 1.7 in the layer below

roughness crest for the rough cases. The stretching ratio of the non-uniform y grid is kept below 0.03. The grid sizes normalized by the local Kolmogorov lengthscale $\eta(y, t)$ are, for SM, S, and T cases respectively, 3-7, 4-9, 2-6 in x and 1-2, 2-4, 2-6 in z, throughout the transient. $\Delta y/\eta$ values are much smaller than those in x and z. For a curved channel flow, scales smaller than 15η are found to contribute to most of the dissipation [81]. Therefore the spatial resolution herein is believed to be sufficient to resolve the dissipative scales of turbulent motions. This is also supported by the small residuals found in Reynolds stress balances as discussed later in Sec. 2.3.5.

Aside from the requirement to resolve the small-scale motions, a rough-wall simulation also required resolution of the roughness geometry. For the sandgrain roughness, the spatial resolution of the grain geometry is 8 and 16 points per grain in x and z, which is slightly higher than the resolution used by [38] (case R1 therein). For the turbine blade roughness, there is no single surface length scale and so an equivalent 'roughness element' size is defined based on the Taylor microscale of surface height fluctuations λ as in [64]. λ is resolved by 10 points in both x and z, same as in [40]. For the rough-wall cases, $y = 0$ is chosen at the lowest trough elevation of the surface. The virtual origin, d—defined as the centroid of the y-profile of averaged drag distribution [82]—is used to offset the wall-normal profiles when comparing results between different cases.

The flow configurations used are similar to those of [56]. A strong temporal acceleration is achieved by imposing a temporally varying streamwise pressure gradient, which is adjusted at each time step to produce a prescribed ramp-like linear increase in the mass flux from u_{b0} to u_{b1} (where u_b is the instantaneous bulk velocity). At time $t^* \equiv tu_{b0}/\delta = 0$, the mass-flow rate is subjected to a ramp increase (during a short time interval $\Delta t u_{\tau 0}/\delta = 0.08$) to achieve $Re_{b1} = 3Re_{b0}$. The flow is then allowed to develop until a new equilibrium state is reached. This ramp-like acceleration is strong enough to cause departure from equilibrium above a smooth wall. A half-height channel is simulated, with symmetric boundary conditions applied at the top boundary, to reduce the computational cost as compared to a full channel. Periodic boundary conditions are applied in x and z.

For each case, the transient simulations are repeated with different initial conditions (obtained from a separate fully developed half-height channel simulation at $Re_{\tau 0}$ for each case). The transient simulation is repeated 20 times for SM and S and 40 times for T. The flow statistics at each t^* are calculated from ensemble averaging. The adequacy of the number of ensembles from which averages are constructed is tested by halving it, which led to changes of around 0.5% in the mean streamwise velocity and less than 4.5% in the Reynolds stresses.

2.3   Results

2.3.1   Initial steady state flows
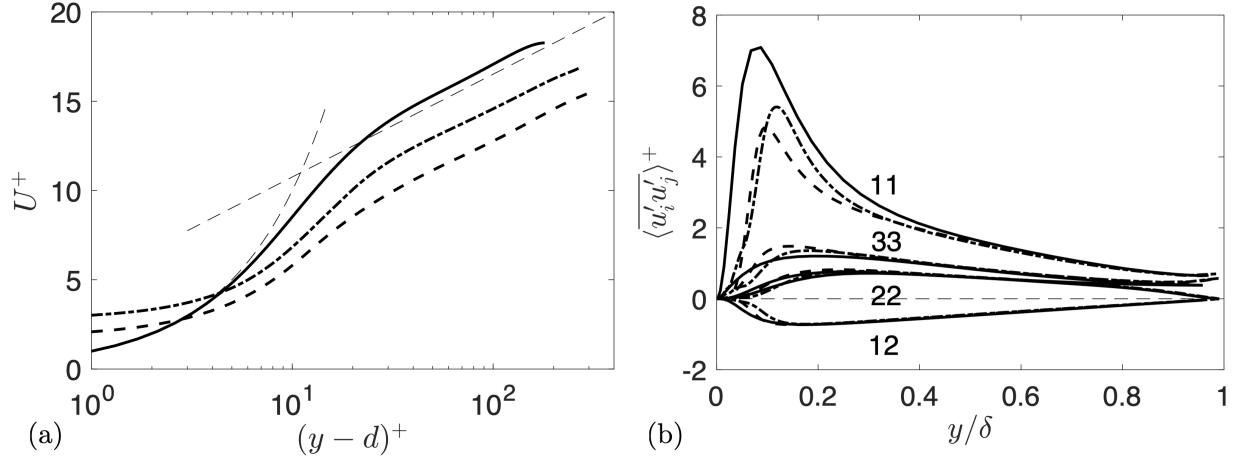
Figure 2.3 (a) DA streamwise velocity, (b) Reynolds stress components at $t^* = 0$, for SM (———), S (---) and T (-·-) cases. $d = 0$ for SM. In (a), thin dashed lines are $U^+ = (y - d)^+$ and $U^+ = 1/0.4 \log(y - d)^+ + 5.0$.

At $t^* = 0$, the wall-normal profile of the DA streamwise velocity $U \equiv \langle \overline{u} \rangle$ in wall units is shown in Fig. 2.3(a) for all cases. The smooth-wall profile compares well with the classical law-of-the-wall, except that the logarithmic intercept B is measured as 5.5 (assuming the von Kármán constant is 0.4), within the range of values that are typically observed (within 5% of 5.2 according to [83]). [84] fitted parameters for the logarithmic law based on available data in the literature and observed that B falls between 5 and 6 for channel flows at displacement thickness Reynolds numbers (Re_{δ^*}) between 300 and 2,000; the present smooth-wall case (SM) gives a Re_{δ^*} of 715, which falls in this range. Compared to case SM, the presence of roughness yielded a velocity deficit (ΔU^+) in the logarithmic region as expected. Case S gives a higher ΔU^+, consistent with the knowledge that surface S led to higher drag generation than surface T [40].

Figure 2.3(b) compared all non-zero components of the Reynolds stress tensor among all cases. The outer-layer similarity is demonstrated for all tensor components. The near-wall layer (where no matching is observed between rough and smooth cases) corresponds to the RSL, defined herein as the near-wall region where the dispersive perturbations are significant with respect to the local mean momentum (see Sec. 2.3.3). In the RSL, similar observations are made as those by [40] for the same rough surfaces at a higher Reynolds number of $Re_\tau = 1000$, including a stronger 11 component and weaker 22 and 33 components of the Reynolds stress tensor in Case T compared to S.

The Reynolds stresses at the channel centerline depart slightly from those at the centerline in a full channel simulation. This is due to the symmetric boundary condition at the top boundary used herein to simulate a half-height channel. Specifically, here v' is imposed to be zero at $y/\delta = 1$. The turbulence kinetic energy is redistributed to u' and w', which is probably the reason for the slightly

17

elevated 11 and 33 Reynolds stress components at $y/\delta = 1$. Similar phenomena are observed by [1].

2.3.2 Temporal variation of ensemble-averaged velocities
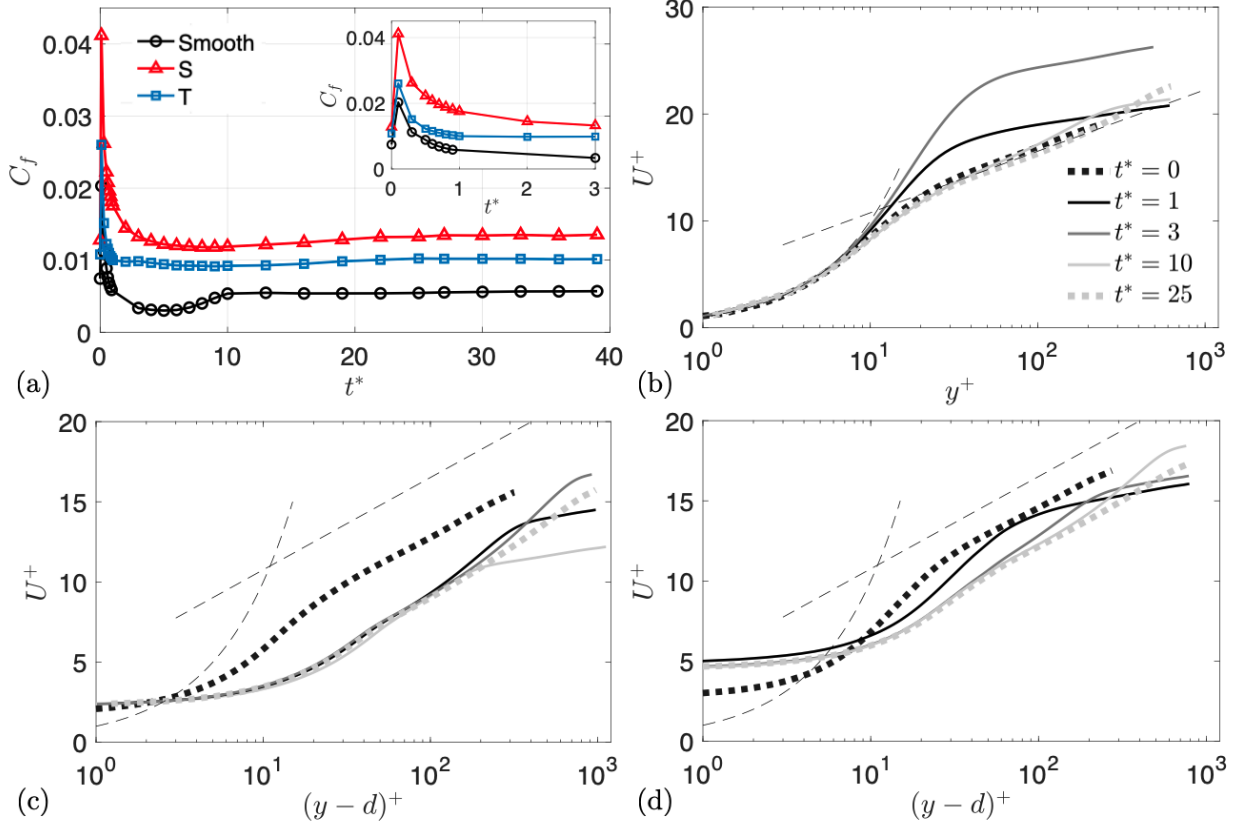
Figure 2.4 (a) Temporal variation of C_f for all cases; inset magnifies the plot at small t^* values. Streamwise DA velocity normalized by instantaneous wall units in (b) smooth case and cases with surface S (c) and surface T (d). ---: $U^+ = (y - d)^+$ and $U^+ = 1/0.4 \log(y - d)^+ + 5.0$.

First, the friction coefficient is obtained by normalizing the instantaneous τ_w with the initial bulk velocity,

$$C_f(t) = \frac{\tau_w(t)}{\rho u_{b0}^2/2},\tag{2.5}$$

and plotted in Fig. 2.4(a). In all cases C_f underwent a sudden increase immediately after $t^* = 0$ in response to the impulse increase of u_b. Following this jump, C_f decreased rapidly as the flow starts to recover. In the smooth-wall case the $C_f(t)$ curve showed a dip (lower than the long-time value) with a minimum C_f found at around $t^* = 5$. For this flow in the corresponding t^* range, [56] observed elongated low-speed streaks, laminar-like mean velocity profiles (also shown in Fig. 2.4b), more anisotropic Reynolds stress tensor (also shown later in Fig. 2.9), and increased TKE production with a frozen pressure strain term (also shown later in Fig. 2.14). These phenomena are indicative of a reverse transition process toward a quasi-laminar state discussed for spatially developing turbulence under a strong freestream acceleration (see e.g. [42] and [44]). The new

18

steady state is reached at $t^* \approx 10$ for the smooth case. In the presence of roughness, there is no appreciable dip in C_f regardless of roughness geometry, indicating that the flows do not undergo reverse transition. Absence of quasi-laminarization on a rough-walled boundary layer subjected to strong streamwise acceleration is also reported by [58]. Also notice that C_f is lower for case T compared to case S throughout the transient.

The DA streamwise velocity profiles U against y (offset by the virtual origin d), both normalized by instantaneous wall units, are plotted in Fig. 2.4(b-d). The value of d stays almost invariant in time for both rough cases throughout the transient: $d/\delta \approx 0.045$ and 0.058 for cases S and T, respectively. On the smooth wall, U^+ departs significantly from the logarithmic law-of-the-wall during reverse transition ($t^* < 5$). Initially, the U profile is characterized by a thickened viscous sublayer and an increase of the von Kármán constant κ, as shown at $t^* = 1$. At $t^* = 3$, the profile became laminar-like, indicating that the flow is in the quasi-laminar state. The logarithmic profile is recovered after the re-transition. For both rough cases, κ also increased temporarily. For case T, this is shown at $t^* = 1$, while for case S, this happened between $t^* = 0$ and 1 and is not shown in the figure. On T roughness, the increase of κ is shown at $t^* = 1$. A higher κ is also observed for spatially developing boundary layer on the sandgrain roughness [58]. Such phenomenon and the difference between cases S and T are explained in Sec. 2.3.4. Lastly, we observed that the logarithmic region recovered faster in case S than in case T. These observations on κ in cases S and T will be explained in Sec. 2.3.4.

The U profiles with linear y axis are compared in Fig. 2.5 in the near-wall region. For all cases, immediately after the impulse acceleration the near-wall rate of shear ($\partial U/\partial y$) increased rapidly to values similar to the final steady state. [85] showed that a constant roughness geometry function, $\Phi(y) \equiv A_f(y)/A_o$ led to an exponential U profile up to the crest height, while a monotonically increasing $\Phi(y)$ as the crest is approached—as in the present cases—lead to a linear velocity profile. Quasi-linear U profiles below k_c are indeed observed for both cases S and T throughout the transient. Notice that for case T the sampling of large surface wavelengths is not as sufficient as the small wavelengths in case S, leading to slight undulation of the quasi-linear $U(y)$ profile below k_c for case T.

In a developing flow, the hydrodynamic drag is more directly connected to the near-wall velocity than to the bulk velocity [58]. A measure of the near-wall velocity scale is the velocity at the edge of the RSL, $U_R(t) \equiv U(y_R, t)$, where y_R is the thickness of the RSL, to be further discussed in Sec. 2.3.3. The RSL is defined herein for all t^* as the near-wall region where $\langle \widetilde{u}^2 \rangle^{1/2}/U < 0.1$, similar to the approach used by [86] (except for a different threshold value used). Throughout the course of the transient, y_R/k_c takes values (1.10 ± 0.13) and (1.05 ± 0.10) for cases S and T, respectively. In other words, the RSL thickness varied weakly in time.
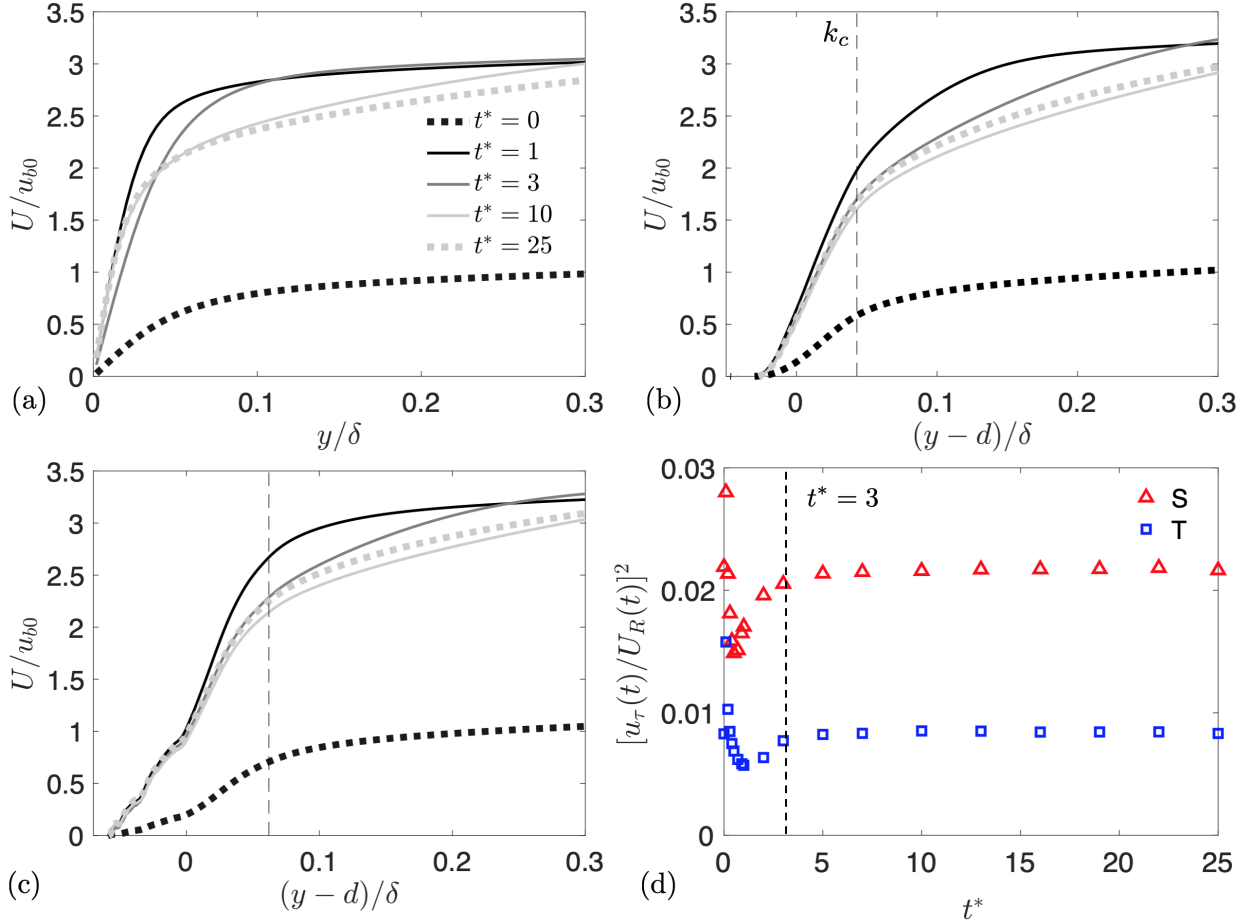
Figure 2.5 (a-c) U profiles against y in linear scaling, for cases SM (a), S (b) and T (c). (d) Instantaneous u_τ normalized by the instantaneous value of the velocity scale at the edge of the roughness sublayer, U_R.

Figure 2.5(d) showed the ratio $[u_\tau(t)/U_R(t)]^2$ for the two rough cases. After $t^* \approx 3$, both cases gave a constant ratio, indicating that the near-wall flows are fully developed even though the U profile shape farther from the wall still varied in time as shown in Fig. 2.5(b-c). For $t^* < 3$, the variation of $u_\tau(t)/U_R(t)$—including the initial spike at $t^* = 0$ and the later dip—showed the non-equilibrium response of the near-wall $\overline{u}(\vec{x}, t)$. The minimum $u_\tau(t)/U_R(t)$ occurred at $t^* \approx 0.5$ and 1.0 for cases S and T, respectively. These time instances are much later than the mean mass flow rate ramp up which ends at $t^* = 0.08$. The observation that the minimum $u_\tau(t)/U_R(t)$ is reached at an earlier t^* in case S than in case T is consistent with the earlier recovery of Reynolds stresses inside the RSL discussed in Sec. 2.3.4. The ratio $u_\tau(t)/U_R(t)$ depended on individual variations of u_τ and U_R in time. The $C_f(t)$ variation (Fig. 2.4(a)) described the variation of u_τ magnitude (as U_∞ is constant for $t > 0$). The $C_f(t)$ comparison showed that u_τ recovers more slowly on S than on T. Yet, the U_R variation is faster on S than on T, contributing to earlier recovery of RSL turbulence on S.

20

2.3.3 Temporal variations of dispersive stresses
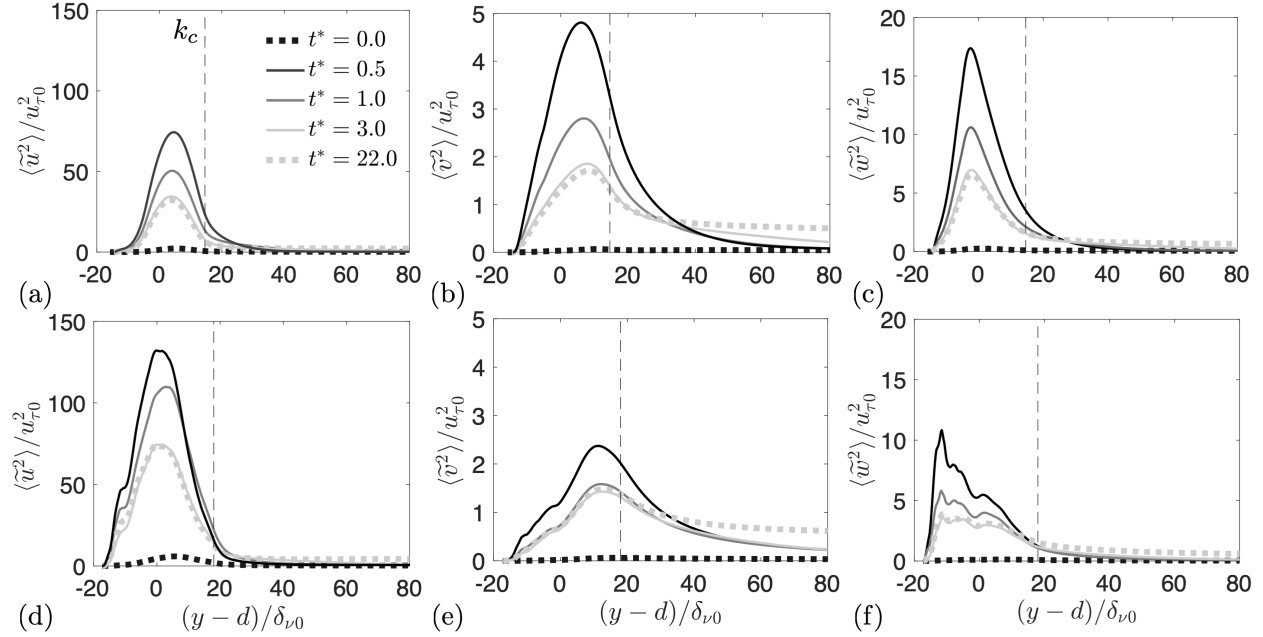
Figure 2.6 Wall-normal profiles of normal components of the dispersive stress tensor (normalized by $u_{\tau 0}^2$) for (a-c) case S and (d-f) case T.

Figure 2.6 compared normal dispersive stresses for cases S and T at different times. In both cases, significant magnitudes of normal dispersive stresses are confined in a near-wall layer. All components increased immediately after the impulse acceleration, rapidly reaching the maximum values before $t^* = 0.5$. These maximum values are considerably higher than the values in the final steady state. After $t^* = 0.5$, all components rapidly decreased, reaching the steady-state values at $t^* = 3$. Notice that the stress profile shapes do not change significantly during the transient; the peak elevations vary only weakly. Figure 2.6 also showed that the RSL thickness, y_R, is not significantly affected during the transient.

Figure 2.5(a) showed that the peak values of $\langle \widetilde{u}^2 \rangle$ slight increased at large times ($t^* > 10$) for both cases. This is probably connected to the development of large scale secondary motions (high and low momentum regions) induced by spanwise roughness heterogeneity [23; 24], toward a higher-Reynolds-number new equilibrium state. Our earlier DNS study [87] of open channel flows at a Re_τ of 1000 showed that the present roughness geometries with similar k_c/δ lead to large secondary motions of the time-averaged flow. These motions are reflected in the non-zero values of $\widetilde{u}$ in the outer layer. These motions developed even for case S, which does not show dominant spanwise wavelength larger than δ.

The main difference between the two rough cases is that case T is characterized by a higher dispersive stress anisotropy (with more intense $\widetilde{u}$ and weaker $\widetilde{v}$ and $\widetilde{w}$). The temporal variations of peak values of the wall-normal profiles of dispersive stress are compared in Fig. 2.7(a)-(c). It is shown that the rapid initial increase and subsequent decrease in peak values take place rather

21

synchronously for both cases, except for $\langle \widetilde{v^2} \rangle$, which recovers at $t^* \approx 1$ in case T, compared to $t^* \approx 3$ in case S.
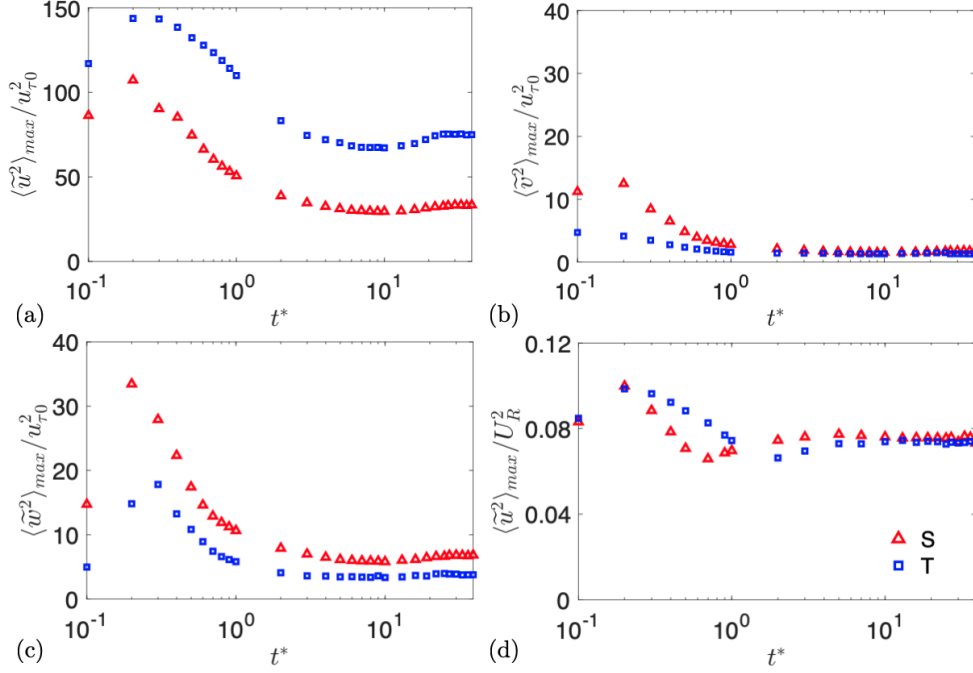
Figure 2.7 Time variation of wall-normal peak value of (a) streamwise, (b) wall-normal, (c) spanwise components of dispersive stress tensor, normalized by $u_{\tau 0}^2$. (d) Peak value of streamwise component normalized by instantaneous U_R^2.

For both rough cases, $u_\tau(t)^2/U_R(t)^2$ in Fig. 2.5(d) and near-wall dispersive stresses in Fig. 2.7(a-c) approached steady-state values at almost the same time of $t^* = 3$. This may be explained by the dependence of u_τ^2 (or the total drag) on roughness-scale flow separations, which are associated with intense $\widetilde{u}_i$ perturbations. To demonstrate such dependence, the variation of the $\langle \widetilde{u^2} \rangle$ peak value normalized by U_R^2 is plotted in Fig. 2.7(d). One observed that the large variation (72% of the maximum value in time) of $\langle \widetilde{u^2} \rangle_{\text{max}}$ scaled using $u_{\tau 0}$ in Fig. 2.7(a) became much weaker (34% of the maximum value in time) when scaled using the instantaneous U_R. The residual time variation in Fig. 2.7(d) is attributed to the non-equilibrium transient process, and possibly to the transition from the initial transitionally rough flow to a later fully rough flow.

Given that the $\langle \widetilde{u_i^2} \rangle(y)$ profile shape varied little throughout (Fig. 2.6), normalizing the profile values using U_R^2 would yield dispersive stress curves that are rather invariant in time. This suggested that most of the temporal variations of $\langle \widetilde{u_i^2} \rangle(y)$ is absorbed by $U_R(t)^2$.

In other words, the mean flow pattern $\overline{u}_i(\vec{x})/U_R$ inside the sublayer appears to stay close to equilibrium during the transient.

2.3.4 Temporal variations of Reynolds stresses
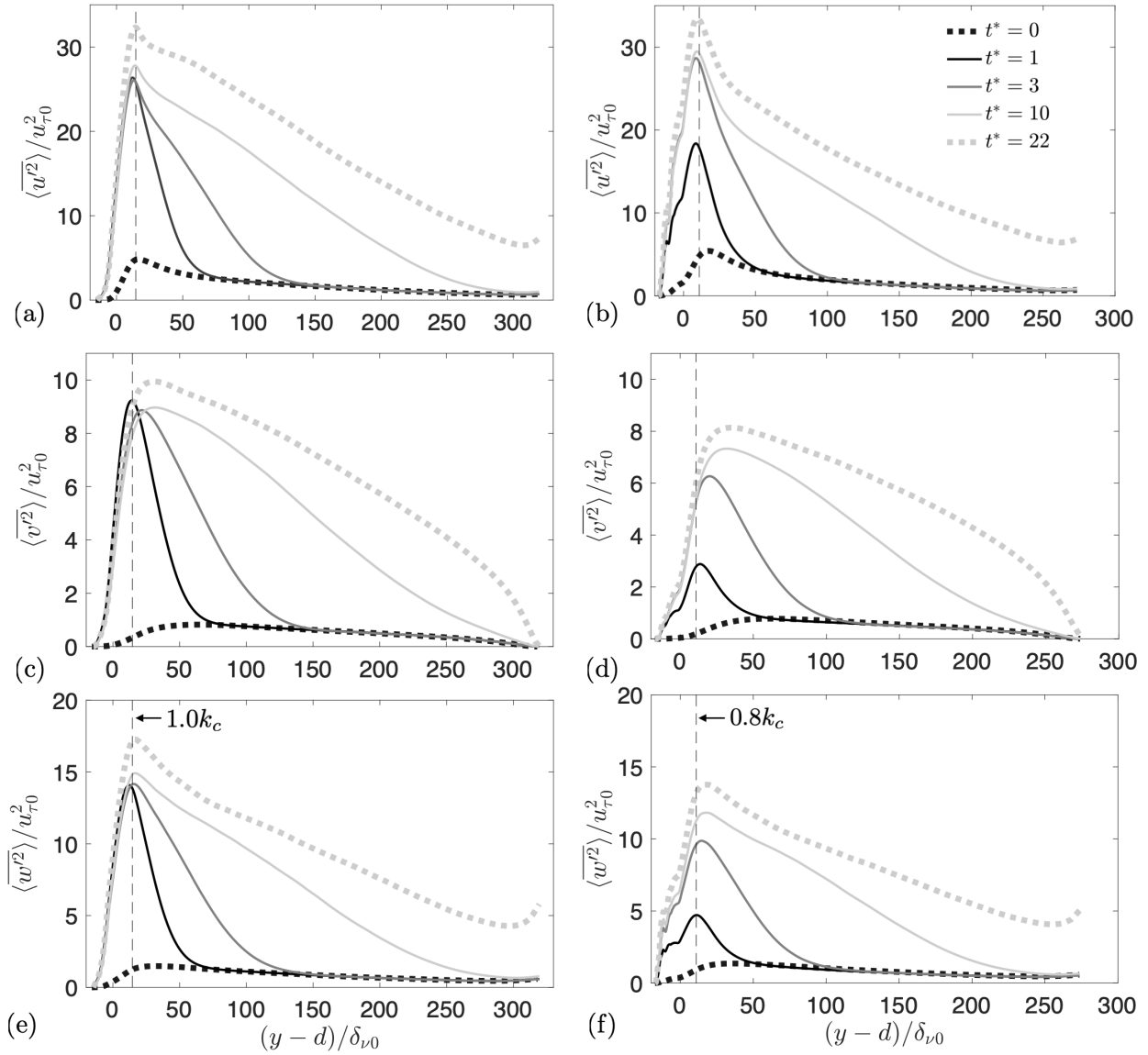
Figure 2.8 Wall-normal profiles of Reynolds stresses, at representative times for S (a,c,e) and T (b,d,f) cases.

For a transient accelerating channel on a smooth wall, [56] showed that $\langle \overline{v'^2} \rangle$ and $\langle \overline{w'^2} \rangle$ are frozen in the initial stage of transient, leading to a quasi-one-dimensional turbulence. Similar observations on a smooth wall are also made by various researchers from spatially developing boundary layers under strong acceleration.

The variation of Reynolds stresses on the two rough walls are shown in Fig. 2.8. The Reynolds stresses are normalized with $u_{\tau 0}$, to show variations of the stress magnitude. Unlike the smooth case described by [56], on the present rough walls all components increase rapidly towards the new steady state, starting from the near-wall region. During the rapid augmentation of Reynolds stresses, the peak elevations of all normal components in case S appear to coincide at $1.0 k_c$. This

indicated that the new turbulence generation immediately after the acceleration occurs at the crest height and is closely linked to the dynamics of flow around tall roughness protuberances. Similarly, for case T, the augmented streamwise Reynolds stress peaked constantly at $0.8k_c$ for T roughness. However, for this roughness the peaks of wall-normal and spanwise Reynolds stresses moved from $0.8k_c$ toward the crest height at late times, probably due to the wide variation in local roughness peak heights brought by the surface heterogeneity. Between the two rough cases, close to the wall all normal Reynolds stresses increased faster in the S case than in T. In both cases, the development of the outer layer profiles lags significantly behind that of the near-wall profiles; the equilibrium states in the outer layer are achieved at around $t^* = 22$.

Figure 2.9 tracked the time variation of the peak value of Reynolds stress profiles. A dependency on the roughness geometry is evident. For the smooth case, $\langle \overline{v'^2} \rangle$ and $\langle \overline{w'^2} \rangle$ peak values remain almost frozen for a significant period of time till $t^* \approx 5$ (corresponding to the stage when C_f decreases), while $\langle \overline{u'^2} \rangle$ peak increased. For $t^* > 5$, $\langle \overline{v'^2} \rangle$ and $\langle \overline{w'^2} \rangle$ rapidly increase, marking the phase of retransition. The streamwise fluctuations overshoot over the steady-state value before the new equilibrium state is reached. This is associated with both the newly generated TKE predominantly resting in u' and the retransition process. Overshoots (though weaker) are also observed for other normal Reynolds stress components. Theses observations are consistent with those described by [56]. A drastic difference brought by the presence of roughness is the rapid increase of all normal Reynolds stress components starting at the beginning of the transient. All normal components increase much faster for surface S. The combination of Figs. 2.8 and 2.9
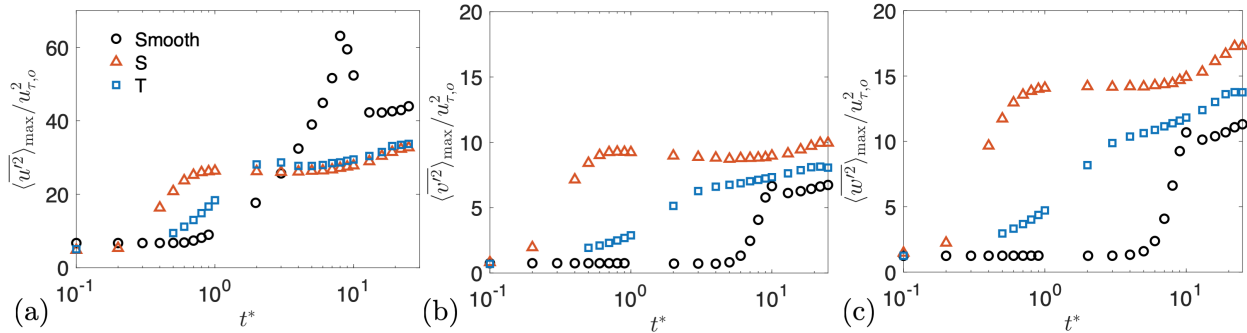
Figure 2.9 Time variation of wall-normal peak value of (a) streamwise, (b)wall-normal and (c) spanwise normal components of Reynolds stress tensor (normalized by $u_{\tau0}^2$).

reveals two stages of Reynolds-stress recovery from an abrupt acceleration on rough walls: (1) an initial stage of rapid recovery of Reynolds stresses inside the RSL as shown in Fig. 2.8, together with a rapid variation of u_τ / U_R (Fig. 2.5(d)) toward the steady state (till around $t^* = 1$ in case S and $t^* = 3$ in case T); and (2) a second stage ($t^* > 1$ for case S and $t^* > 3$ for T) marked mainly by the variation of the outer-layer Reynolds stresses.

Figure 2.10 showed the variation of anisotropy parameter (or the streamwise energy partition

parameter) defined by [88] as

$$K^*(y, t) = \frac{2\overline{\langle u'^2 \rangle}}{\overline{\langle v'^2 \rangle} + \overline{\langle w'^2 \rangle}}. \tag{2.6}$$

As an overall measure of the Reynolds stress anisotropy, K^* quantified the distribution of TKE among streamwise fluctuations and those in the other two directions. Profiles of K^* for all cases are compared in Fig. 2.10 at several t^*. For the smooth case in the early stage ($t^* < 3$), K^* increased rapidly near the wall from its initial steady-state profile, indicating flow development toward quasi-one-dimensional turbulence. On the rough walls, in contrast, the Reynolds stress anisotropy monotonically decreased, recovering to the long time values well before $t^* = 3$; the subsequent slow recovery of outer-layer Reynolds stresses does not alter the anisotropy. The difference between the initial and final steady states for the rough cases is because the flows are not fully rough at $Re_{\tau 0}$. Compared to case S, case T yielded higher Reynolds stress anisotropy for all t^*.
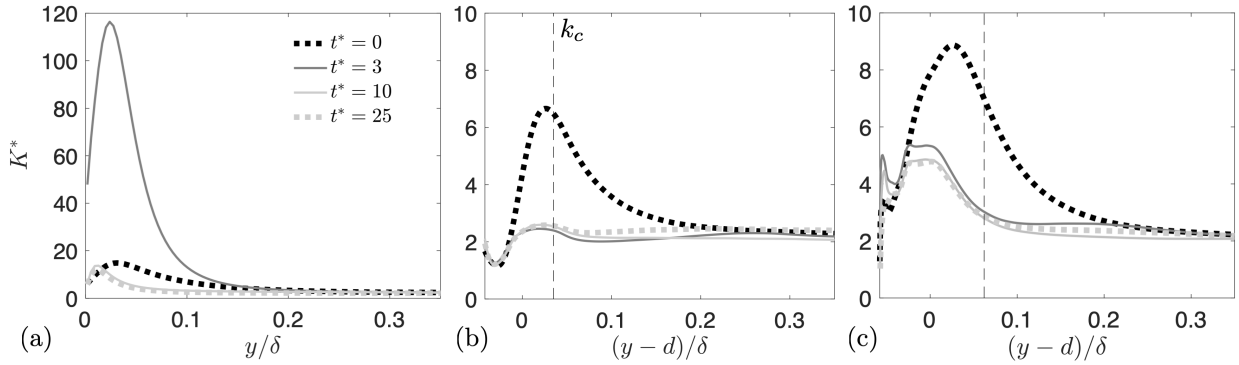
Figure 2.10 Variation of anisotropy parameter K^* at various t^* for (a) smooth-wall, (b) S and (c) T cases. $\cdots$ Steady states.

Figure 2.11 compared the dispersive shear and the Reynolds shear stresses. For both roughnesses, in the initial and final steady states $\langle \widetilde{u}\,\widetilde{v} \rangle$ is significantly weaker than $\langle u'v' \rangle$. During the transient, however, $\langle \widetilde{u}\,\widetilde{v} \rangle$ becomes significant below k_c, sometimes surpassing the Reynolds shear stress. Thus, the dispersive shear stress can be dynamically important for mean-flow response in a developing flow. We note also that the dispersive shear stress becomes positive (with small magnitudes) for a brief time at the beginning of the transient. It remains an interesting question for future work as to what contributes to this phenomenon.

We now explain the earlier observations on the logarithmic slope of U profiles shown in Fig. 2.4, namely, the increase of κ in rough-wall cases at early t^* and the faster recovery of κ for S than for T. On a smooth wall, the increase of κ under a favorable pressure gradient is explained by [89] as a result of departure of the velocity scale of attached eddies from the scale of u_τ, i.e.

$$\frac{\kappa}{\kappa_o} = \frac{u_\tau}{U_T}, \tag{2.7}$$

25

where κ_o is a universal von Kármán constant measured from canonical flows with zero pressure gradient, y_c is the critical y at which the near-wall sublayer 'becomes unstable' [90], $U_T \equiv \sqrt{\tau(y_c)/\rho}$ is the critical velocity scale of the sublayer (i.e. velocity scale of the attached eddies), and $\tau(y)$ is the total shear stress. By fitting smooth-wall data with a widerange of streamwise pressure gradients,

(a)   (b) $(y-d)/\delta_{\nu 0}$
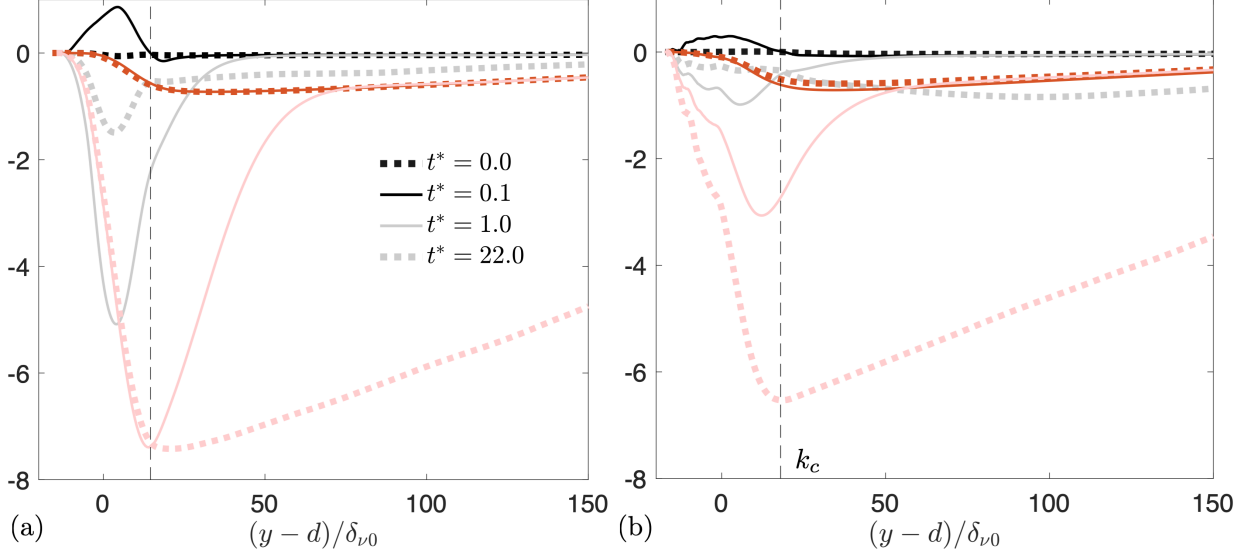
Figure 2.11 Wall-normal profiles of dispersive (black and grey) and Reynolds (red and light red) shear stresses, normalized by $u_{\tau 0}$ for cases (a) S and (b) T cases.

[89] identified y_c^+ to be around 10 to 14. With the presence of rough wall herein, we take $y_c = k_c$ for simplicity; a supporting argument for this choice is that the negative peak of combined Reynolds and dispersive shear stress is located at around k_c for both S and T for all t^* (Fig. 2.11). This stress is then considered to set the velocity scale of the attached eddies. After the impulse acceleration, u_τ is higher than its steady-state value (Fig. 2.4(a)), while $\tau(k_c) \approx \rho\langle\overline{u'v'}\rangle(k_c) + \rho\langle\widetilde{u}\widetilde{v}\rangle(k_c)$ is lower than its steady state value. Since in the steady state, $\tau(k_c) \approx u_\tau^2$ [58], this means $\kappa/\kappa_o > 1$ according to Eq. (2.7). In addition, the faster recovery of κ on S roughness is due to the fast recovery of its $\tau(k_c)$ to the steady state value—as early as $t^* \approx 1.0$ (Fig. 2.11(a)); at this point Eq. (2.7) yields $\kappa/\kappa_o \approx 1$.

Results in this section show that turbulence inside the RSL develops rapidly to the new steady state, while the outer layer varied slowly. The role of roughness geometry came in by affecting the rate of response of turbulence inside the RSL and, in doing so, affecting the rate of recovery farther from the wall.

2.3.5   Temporal variations of Reynolds stress budget balances

The budget equation of the normal Reynolds stresses $\langle\overline{u'_\alpha u'_\alpha}\rangle_s$ (no summation on Greek indices) in a transient half-height channel flow on a rough wall is extended from the equation for a fully-

26

developed open-channel flow on a rough wall [37] and reads

$$
\frac{\partial \langle \overline{u_\alpha'^2} \rangle_s}{\partial t} = \underbrace{\left[\underbrace{-2\langle \overline{u_\alpha' v'} \rangle_s \frac{\partial \langle \overline{u}_\alpha \rangle}{\partial y}}_{P_s} + \underbrace{P_w + P_m}_{P_s^f} \right]}_{} \underbrace{- \left\langle \frac{\partial}{\partial x_j} \widetilde{u_\alpha' u_\alpha'} \widetilde{u}_j \right\rangle_s}_{T_w} \underbrace{- \left\langle \frac{\partial}{\partial x_j} \overline{u_\alpha' u_\alpha' u_j'} \right\rangle_s}_{T_t}
$$

$$
\underbrace{-2 \left\langle \overline{P' \frac{\partial u_\alpha'}{\partial x_\alpha}} \right\rangle_s}_{\Pi} \underbrace{-2 \frac{\partial \langle \overline{P' u_\alpha'} \rangle_s}{\partial x_\alpha}}_{T_p} \underbrace{+\nu \left\langle \frac{\partial^2 \overline{u_\alpha'^2}}{\partial x_j \partial x_j} \right\rangle_s}_{T_\nu} \underbrace{-2\nu \left\langle \overline{\frac{\partial u_\alpha'}{\partial x_j} \frac{\partial u_\alpha'}{\partial x_j}} \right\rangle_s}_{\epsilon}, \qquad (2.8)
$$

where the terms on the right-hand-side are, respectively, shear production due to shear of DA velocity (P_s), additional shear production due to shear of the form-induced velocities (P_s^f, as the sum of the wake production $P_w = -2\langle \widetilde{u_\alpha' u_j'} \partial \widetilde{u}_\alpha / \partial x_j \rangle_s$ [36] and a correction term $P_m = -2\langle \overline{u_\alpha' u_j'} \rangle \langle \partial \widetilde{u}_\alpha / \partial x_j \rangle_s$ [37]), transport due to form-induced velocities (T_w), turbulent transport (T_t), viscous transport (T_ν), pressure strain rate (Π), pressure transport (T_p), and viscous dissipation (ϵ). The interface cells are not included in performing the spatial averaging in the present IBM framework. If the interface cells are also included, an additional term $2\langle \overline{F_\alpha' u_\alpha'} \rangle_s$—with a small magnitude of 4% of P_s peak value appears due to the IBM body force, but the nature of the balance is not affected. This point is discussed by [40]. For the smooth case, Eq. (2.8) still applies with the form-induced terms P_s^f and T_w equal to zero. For all cases the residuals of Eq. (2.8) obtained in the steady states are up to 1% of the peak value of P_s. Here, the budget balance refered to the left-hand-side and right-hand-side of Eq. (2.8) being equal. The balance applied to all t^*.

The budget terms in the smooth case are discussed first. Figure 2.14 showed the sources terms of u' energy ($P_{s,11}$) and of v' energy (pressure work, $\Pi_{22} + T_{p22}$) at several time instances: (1) the initial state, (2) $t^* = 3$ (quasi-laminarization stage) and (3) $t^* = 5$ (near the onset of retransition). Figure 2.14(a) showed that $P_{s,11}$ increased steadily throughout the quasi-laminarization stage, leading to intensification of u' (i.e. $\partial \langle \overline{u'^2} \rangle_s / \partial t > 0$) immediately after $t^* = 0$. In comparison, the pressure work remained almost frozen in the quasi-laminarization stage. Consequently, the v' intensity remained around the initial level in this stage, as shown at $t^* = 3$ in Fig. 2.9. A similar slow response of pressure work for w' energy is also observed (not shown). The delay in increase of v' and w' intensities together with the immediate augmentation of u' led to the much increased Reynolds stress anisotropy and quasi-one-dimensional turbulence during quasi-laminarization.
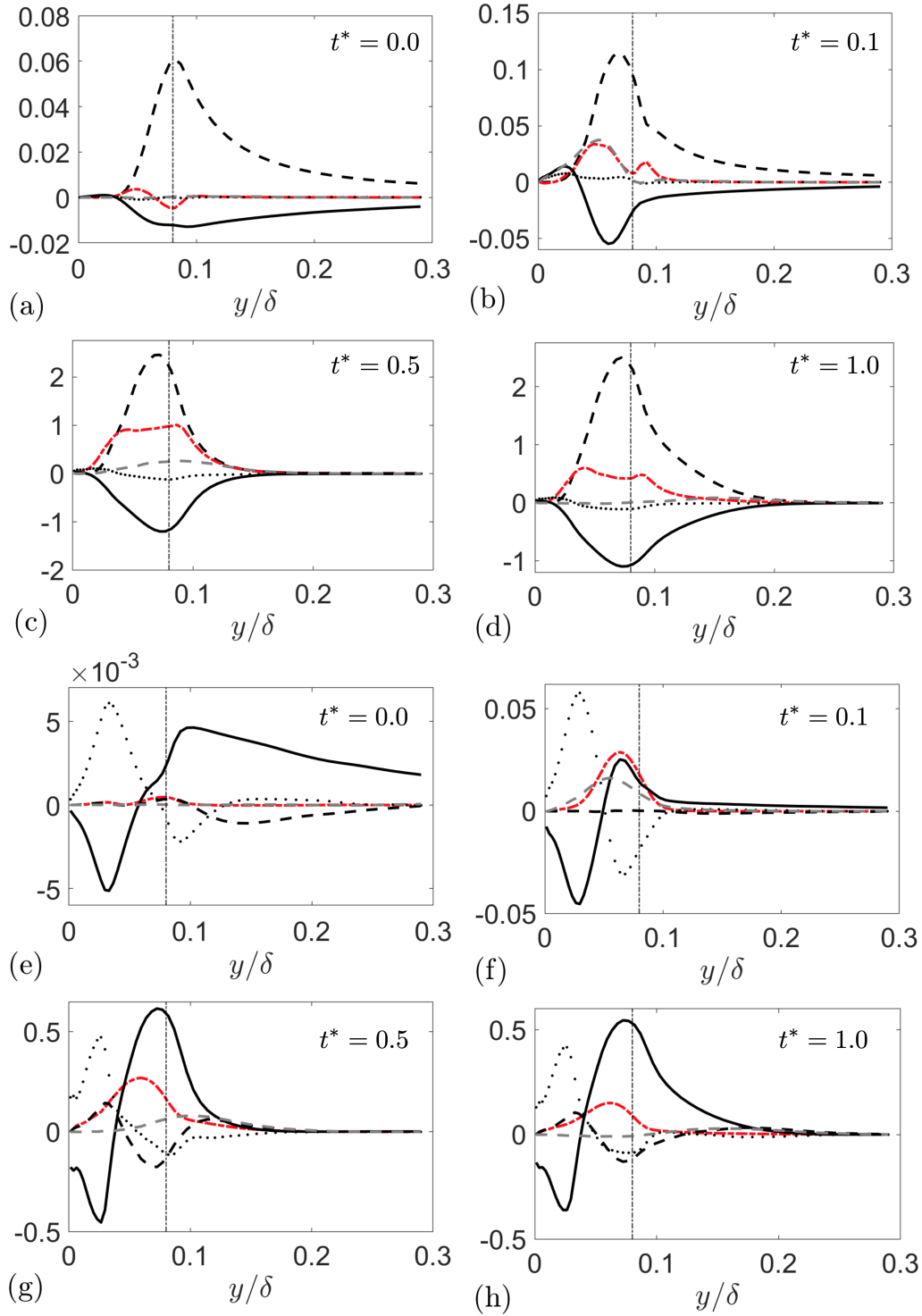
Figure 2.12 Budget balance for $\langle \overline{u'^2} \rangle_s$ (a-d) and $\langle \overline{v'^2} \rangle_s$ (e-h) in case S. Budget terms are normalized by u_{b0} and δ. Vertical line indicates $y/k_c = 1$. $---$ (gray) $\partial/\partial t$ term; $-\cdot-$ P_s^f; —— Π; In (a-d), $---$ (black) P_s; in (e-f), $---$ (black) T_t, $\cdots$ T_p.
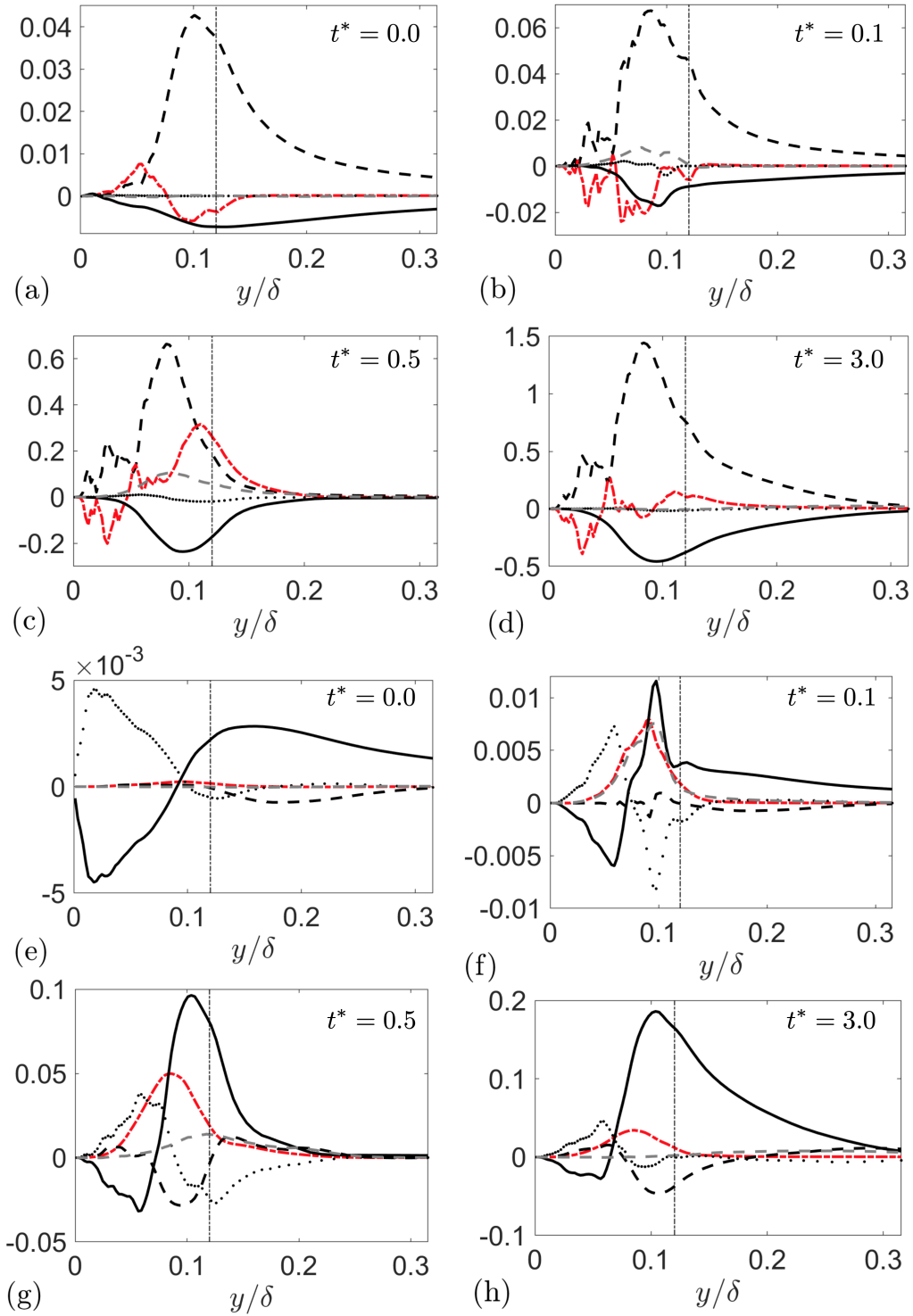
Figure 2.13 Budget balance for $\langle \overline{u'^2} \rangle_s$ (a-d) and $\langle \overline{v'^2} \rangle_s$ (e-h) in case T. Budget terms are normalized by u_{b0} and δ. Vertical line indicates $y/k_c = 1$. --- (gray) $\partial/\partial t$ term; --- P_s^f; ——— Π; In (a-d), --- (black) P_s; in (e-f), --- (black) T_t, ⋯ T_p.

29

In the presence of roughness, a different balance from that in the smooth case is observed immediately after $t^* = 0$. Figure 2.12 showed the budget for u' and v' energy for case S, at four characteristics time instances: $t^* = 0$, $t^* = 0.1$ and 0.5 (two instances in the stage of rapid development of RSL turbulence), and $t^* = 1$ (after the RSL is fully developed). Comparison with the balances at $t^* = 25$ (not shown) suggested that the near-wall balance recovers to the steady state at $t^* \approx 1.0$. For the streamwise Reynolds stress, P_s^f took positive values with significant magnitudes in both the transient and the final steady state, though the magnitudes are smaller compared to the magnitudes of P_s and Π in most of the RSL. The time-rate-of-change term remained positive (indicating augmentation of u') till $t^* \approx 1.0$. For the wall-normal Reynolds stress, P_s^f also took significant magnitudes. At $t^* = 0.1$, P_s^f is of similar magnitude as Π. At this time, the time-rate-of-change of $\langle \overline{v'^2} \rangle$ is positive and peaks roughly at the elevation of the P_s^f peak. At later times (shown at $t^* = 0.5$ as an example), the Π magnitude overtook that of P_s^f. The steady state is recovered at $t^* = 1$ for the near-wall balance of v' energy also. The subsequent recovery of outer-layer budget terms did not modify the nature of the balance.
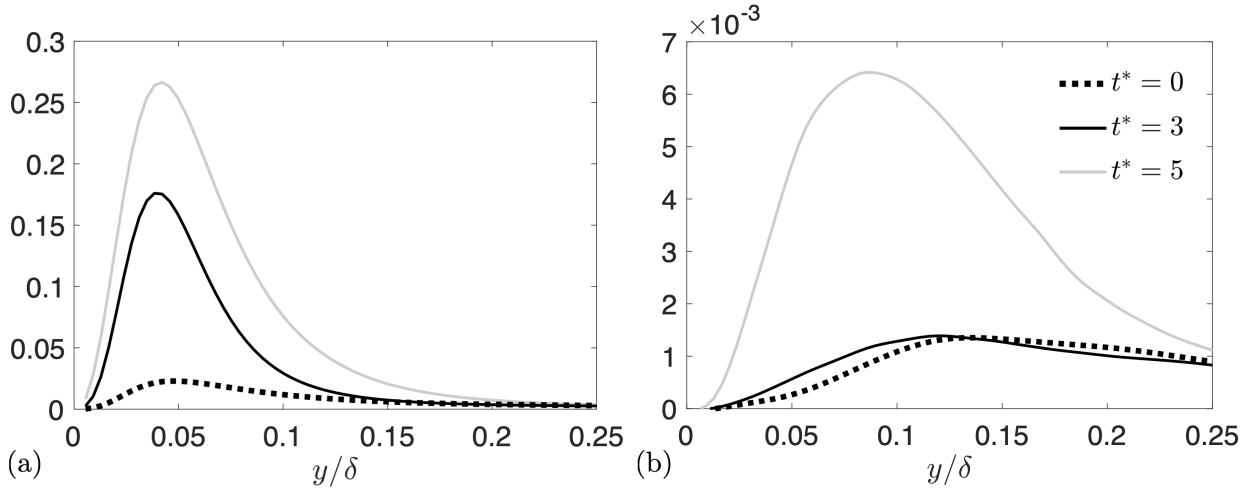
Figure 2.14 Reynolds stress budget terms in the smooth-wall case, normalized by u_{b0} and δ. (a) Shear production for $\langle \overline{u'^2} \rangle_s$ and (b) pressure work for $\langle \overline{v'^2} \rangle_s$.

The same budget terms are shown in Fig. 2.13 for case T, also at four characteristic time instances. The first three of the four t^* instances are chosen to be the same as in Fig. 2.12, while the last time is chosen at a slightly later time of $t^* = 3$, at which RSL became fully developed for case T. For the streamwise Reynolds stress, P_s^f showed a rather complex pattern, as its sign changed for different y and t^*. Recall that P_s^f represented the amount of kinetic energy transferred from $\widetilde{u}_i$ kinetic energy (or 'wake kinetic energy', WKE, termed by [36]) at scales larger than turbulent eddies to the TKE by shear production. Such complex dependence of the sign of P_s^f on the wall-normal distance and time may suggest a competition between TKE-to-WKE and WKE-to-TKE transfers. On a multiscale roughness, it is possible that both very large u' scales and very small $\widetilde{u}_i$ scales exist, contributing to local energy transfer from TKE to WKE. For the wall-normal Reynolds stress, case

30

T also yielded large magnitudes of P_s^f in the initial stage of RSL development, although $P_s^f \ll \Pi$ in the steady states. In both cases, P_s^f remained positive for all t^* and all elevations for the $\langle \overline{v'^2} \rangle$ budget, indicating energy transfer from $\widetilde{v}$ to v' motions. This is probably because intense v' values (associated with small-scale active motions) occur typically at a scale smaller than the characteristic lengthscale of the time-mean velocity variation.

In summary, the similarities between the two rough cases included: (1) the immediate augmentation of P_s^f, especially important for $\langle \overline{v'^2} \rangle$ production; (2) the subsequent increase of Π, which later became the dominant source of $\langle \overline{v'^2} \rangle$ as P_s^f weakened in time; and that (3) the $\langle \overline{u'^2} \rangle$ budget balance is also modified by P_s^f, which took significant magnitudes during the transient.
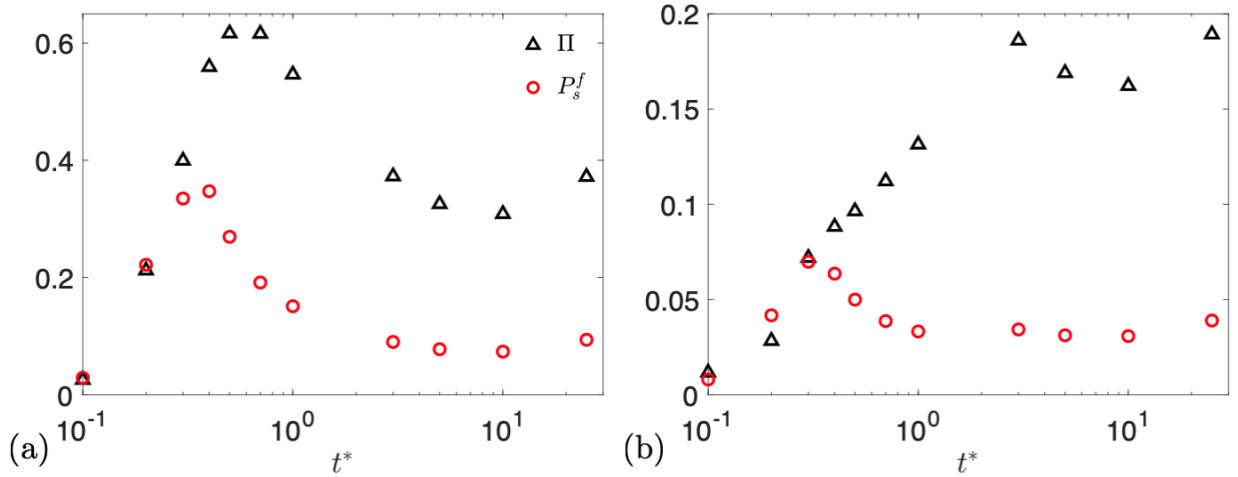
Figure 2.15 Temporal evolution of the positive peak values of Π and peak values of P_s^f (both normalized by u_{b0} and δ) in $\langle \overline{v'^2} \rangle$ budget in cases S (a) and T (b).
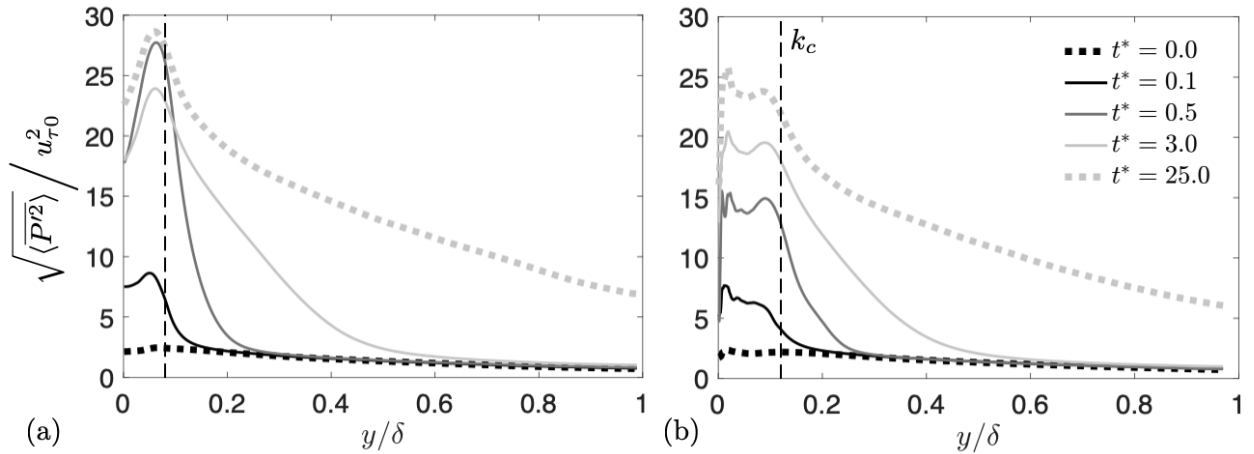
Figure 2.16 Wall-normal profiles of P' rms (normalized by $u_{\tau 0}^2$) for cases (a) S and (b) T at different t^*.

The main effect of the roughness geometry appeared to be reflected in different rates of recovery of the budget balance. Here, we focused on the $\langle \overline{v'^2} \rangle$ budget, as the temporal variation of its balance is more significant than that for $\langle \overline{u'^2} \rangle$. Figure 2.15 compared the temporal variation of the peak

values of Π and P_s^f for cases S and T. The sign of Π changes inside the RSL; the positive peak of Π is shown here to better represent the nature of this term being an overall source for $\langle v'^2 \rangle$. It is shown that for both surfaces P_s^f peaks at a similar t^* of around 0.3-0.4. This is because that P_s^f depended on $\partial \widetilde{u}_i / \partial x_j$, and that the time variations of the dispersive stresses between cases S and T are almost synchronous due to the approximate scaling of $\widetilde{u}_i$ on U_R. In contrast, Π increases and peaks at $t^* \approx 0.5$-0.7 for case S, while it peaked much later—at $t^* \approx 3$—for case T. To provide further explanation to the different timing of Π term recovery, Fig. 2.16 compared the time variation of the pressure fluctuation RMS profiles between S and T cases; a faster recovery of near-wall P' intensity is seen for case S. Specifically, the P' RMS values below k_c in case S almost reached their steady state values at $t^* = 0.5$, while in case T they continued to increase in large time.
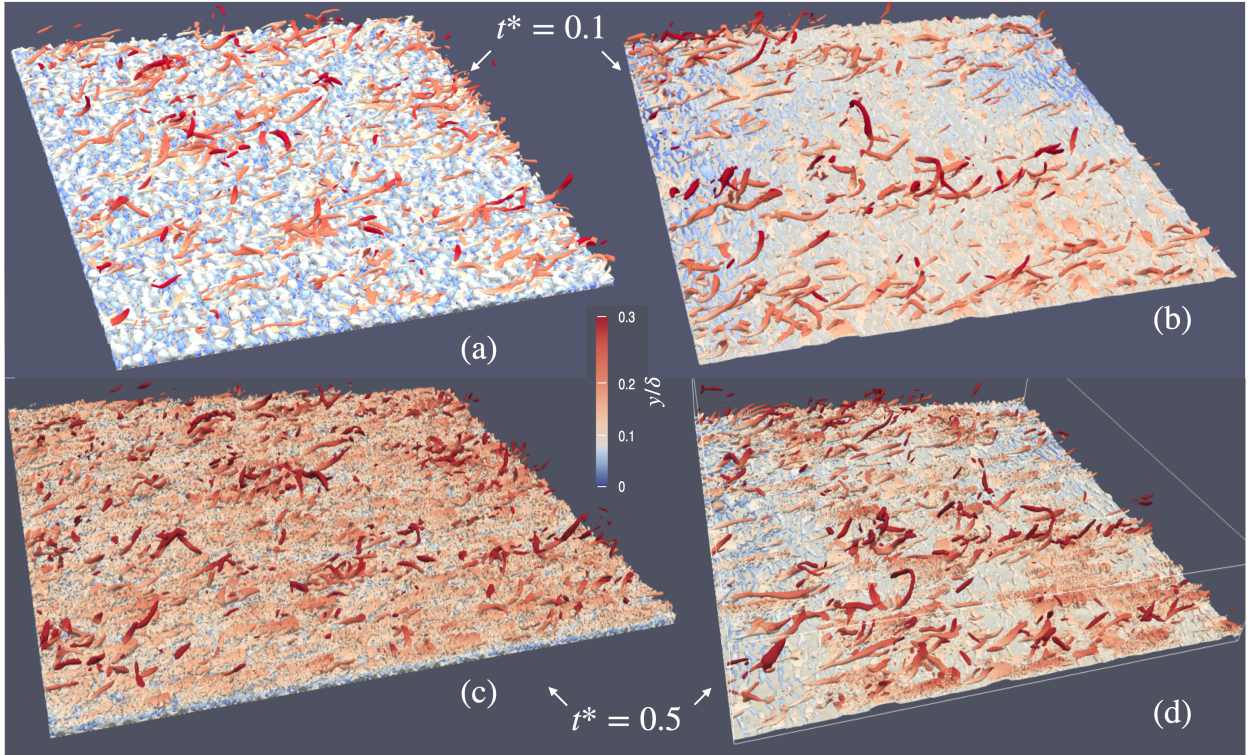
Figure 2.17 Q-isosurfaces at (a-b) $t^* = 0.1$ and (c-d) $t^* = 0.5$ for (a,c) case S and (b,d) case T colored by distance to wall and rough surface colored in white.

To provide insights as to why the P' intensity varied differently between cases S and T, Fig. 2.17 compared the coherent vortical turbulent motions visualized using the second-invariant of the velocity gradient tensor,

$$Q = -\frac{1}{2} \frac{\partial u_i}{\partial x_j} \frac{\partial u_j}{\partial x_i}. \qquad (2.9)$$

The generation of new turbulence of small scales during $0.1 < t^* < 0.5$ are evident. These motions are located at y of 0.1-0.2δ (in the vicinity of k_c). On surface S, these newly generated eddies are widespread in the horizontal plane, as the roughness protuberances are closely packed. On

surface T, in comparison, the distribution of these motions are more spotty, associated with more sparsely distributed high-slope roughness peaks. It is conjectured that the large wavelengths (with mild slopes) of surface T did not lead to flow separation or strong $\partial \widetilde{u}_i / \partial x_j$ that generated v' energy through P_s^f, while the sparsely distributed small-wavelength peaks produced turbulence, which then slowly spread to cover the whole horizontal domain. As the P' distribution is related to vortical motions, the P' RMS developed more gradually in case T.

2.4 Conclusions

Direct numerical simulations of the impulse response of half-height channel flows on a smooth wall and two rough surfaces to a step increase of bulk velocity are carried out. Two roughness geometries are included: a densely distributed sandgrain roughness (case S) and a multiscale turbine-blade roughness (case T). Both cases shared the same mean roughness height and developed from a transitionally rough flow to a fully rough one during the transient. Different flow responses between the rough and smooth cases, as well as between the two rough cases, are discussed. As seen in the existing literature of temporally and spatially accelerated flows, turbulence over a smooth wall underwent a quasi-laminarization process, characterized by high Reynolds stress anisotropy caused by a delayed response of the TKE redistribution to the acceleration. These phenomena are not observed in the presence of roughness.

On rough walls, the roughness sublayer layer (RSL) thickness stayed almost constant during the transient. Inside the RSL, the temporal variations of the form-induced fluctuation are largely absorbed when normalized by the instantaneous mean velocity at the edge of the RSL (i.e., U_R). This indicated that the ensemble-averaged flow ($\overline{u}/U_R$) in the sublayer stayed close to equilibrium during the transient.

Two stages of the turbulence recovery from an abrupt acceleration on a rough wall toward the new steady state are observed, including: (1) a short, initial stage of rapid recovery of hydrodynamic drag and increase of RSL turbulent intensities till their early recovery to the long-time values, and (2) a slower second stage marked mainly by the variations of the outer-layer Reynolds stresses. In the second stage, the Reynolds stress balance is similar to the steady state, while during the first stage a fundamental change of Reynolds stress balance is observed. In particular, the magnitude of the form-induced production P_s^f became much larger than in the steady state, strikingly so for $\langle \overline{v'^2} \rangle$. The result is a rapid augmentation of TKE and a decrease of Reynolds stress anisotropy, manifested by the generation of small-scale new turbulence in regions of intense form-induced shear. Also, in the first stage the total shear stress at roughness crest is significantly lower than the wall shear stress, leading to a reduced logarithmic slope of the mean velocity. The roughness geometry affects the rate of recovery of the RSL turbulence. A slower recovery of TKE redistribution (due to a slower amplification of pressure fluctuations) is seen in case T. This is associated with sparsely distributed small-wavelength roughness peaks, producing new turbulence which took time to spread and cover

33

the whole domain.

This work provides detailed explanations on how roughness suppressed reverse transition in a non-equilibrium accelerated turbulence. Results indicated that, unlike fully-developed wall bounded turbulence where outer-layer similarity applied and the roughness sublayer flow affected the value of u_τ only, in the present non-equilibrium transient flows the sublayer details played a more important role by determining the rate of flow recovery throughout the boundary layer.

CHAPTER 3
EFFECTS OF FORM-INDUCED VELOCITY IN TURBULENT HALF CHANNEL FLOWS

3.1   Introduction

This chapter of the thesis will be also referenced in the text as [91]. The existing studies summarized in Chapter 1 showed that the form-induced field played a role in affecting the turbulence response in the presence of roughness. Chapter 2 characterized the overall responses of the turbulent flows to the acceleration, focusing on the mean flow and single-point turbulence statistics. In addition, the form-induced fields ($\widetilde{u}_i$) are found to be much more important for the dynamics of a transient accelerating channel, compared to fully-developed channel flows or boundary layers as studied by [38], [40] and [37]. The resultant form-induced production becomes the dominant source of v' at the early stage of the transient, which played a major role in preventing reverse transition. Furthermore, the apparently synchronous growths of both the TKE pressure-strain term and the form-induced production at the early stage suggested a possible role of the form-induced quantities in affecting the TKE redistribution through the pressure-strain term.

To fully understand how the roughness geometry determined the particular turbulence response in a non-equilibrium transient flow, it is necessary to examine (1) how roughness and $\widetilde{u}_i$ affected turbulence structure (besides single-point turbulent statistics studied in Chapter 2) and (2) various mechanisms through which the form-induced quantities modified Reynolds stress transport. Specific questions of this chapter included the following.

1. How do the length scales of turbulent and form-induced fields vary in time? How are they affected by roughness topography?

2. How do the near-wall strain rate of the double-averaged velocities and that of the form-induced velocities vary in time? are they strong enough to linearly modify the shape of the turbulent eddies without affecting production (i.e. rapid distortion), similar to the quasi-laminarization process on a smooth wall?

3. How much do the turbulent and form-induced velocities affected the turbulent pressure fluctuations and, consequently, the TKE redistribution process as an important mechanism in the Reynolds stress transport?

The DNS data obtained in Chapter 2 are used for analyses herein. The organization of this chapter is as follows. The problem formulation is summarized in 3.2, an overview of turbulent statistics from 2 are shown in 3.3. Temporal variations of the length and time scales of turbulence and the form-induced velocities are studied in Sections 3.3.1 and 3.4.1, respectively. Various sources of the pressure fluctuations are compared in Section 3.4.2. Conclusions are provided in Section 4.4.

3.2 Problem formulation

Case	Re_{b0}	$Re_{\tau 0}$	$k^+_{s\infty,0}$	$(\Delta x^+, \Delta z^+)_0$	Re_{b1}	$Re_{\tau 1}$	$k^+_{s\infty,1}$	$(\Delta x^+, \Delta z^+)_1$
SM	4,000	244	0	(4.0, 2.0)	12,000	626	0	(9.8, 4.8)
S	4,000	320	21	(5.0, 2.5)	12,000	1023	76	(15.3, 7.6)
T	4,000	294	10	(3.4, 3.4)	12,000	858	23	(10.1, 10.1)

Table 3.1 Simulation parameters at initial ('0') and new ('1') steady states. '+' indicated normalization in wall units (i.e. u_τ and viscous length scale $\delta_v = \nu/u_\tau$). Δx_i is the cell size in x_i direction. $Re_b = u_b\delta/\nu$ and $Re_\tau = u_\tau\delta/\nu$. δ is channel half height.

A summary of the methodologies and simulation setups as reported in [2] is provided here. The readers are referred to that publication for further details.

The incompressible flow of a Newtonian fluid is simulated by solving the equations of conservation of mass and momentum. x, y and z are, respectively, the streamwise, wall-normal and spanwise directions of the half-channel flow, and u, v and w are the velocity components in those directions. p is the pressure, ρ is the density and ν is the kinematic viscosity. Periodic boundary conditions are applied in x and z domain boundaries, and symmetric and no-slip conditions are applied to the top and bottom boundaries, respectively. In the rough cases, an immersed boundary method is used to impose the no-slip and no-penetration boundary condition on the rough walls. It is based on the volume-of-fluid approach; its detailed implementation in the in-house fluid solver is described by [38] and [79]. The governing equations are solved on a staggered grid using second-order central differences for all terms, second-order accurate Adams-Bashforth semi-implicit time advancement, and Message-Passing Interface parallelization.

To conduct the present transient channel simulations, first a separate simulation is carried out for each case at the initial steady state with a bulk Reynolds number Re_{b0}, to generate statistics at this state and be used as initial conditions for the transient simulations. The transient simulations are then carried out, based on independent initial conditions, for around 20 times for each case to collect data for ensemble averaging at each time t. During a transient simulation, the variation of $Re_b(t)$ is imposed, equivalent to a rapid three-fold linear increase of the bulk velocity (u_b) that started at time $t = 0$ and lasted for a duration of $t^* = tu_{b0}/\delta = 0.08$ (see Figure 3.2a). u_b remained constant thereafter. This simulation setup is similar to that of [56], though with quantitative differences in the Reynolds number and the amount and rate of the velocity ramp-up.

Simulation parameters for all cases are listed in Table 3.1. The initial and final steady states are denoted using subscripts "0" and "1", respectively. "SM", "S", and "T" represent the smooth-wall, sandgrain, and a multiscale turbine-blade-roughness cases, respectively. The same time-variation of Re_b is imposed in all cases. Both rough cases started in transitionally rough regime at the initial steady state and became fully rough at the new steady state, as shown by the $k^+_{s\infty}$ values. Here, $k_{s\infty}$ is the equivalent Nikuradse sandgrain height in the fully rough regime of a rough surface; the

critical values of $k_{s\infty}^+$ for the present roughnesses corresponding to the lower limit of the fully rough regime are reported by [64].
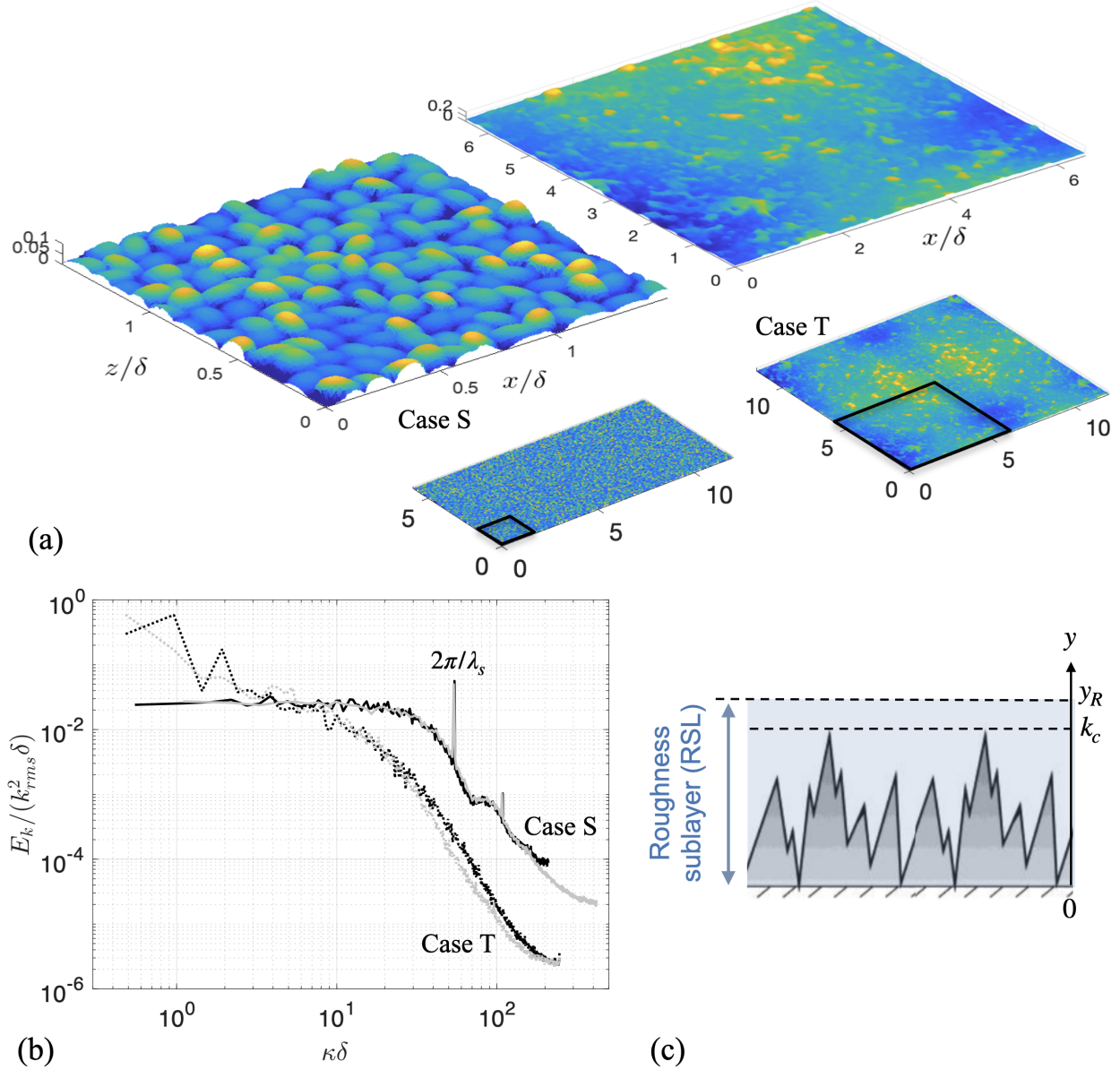
Figure 3.1 (a) Geometries of sandgrain (case S) and turbine-blade-roughness (case T) surfaces colored by height, with zoomed-in view. (b) Power spectral density of height fluctuations, with wavenumber κ in x (black) and z (gray). (c) Sketch of a rough surface showing various length definitions.

On a rough wall, the wall shear stress τ_w results from both the viscous and pressure drag due to roughness. It is calculated as

$$\tau_w(t) = \frac{\rho}{L_x L_z} \int_V \overline{f}_1(x, y, z, t) \, \mathrm{d}x \, \mathrm{d}y \, \mathrm{d}z + \mu \frac{\partial \langle \overline{u} \rangle_s}{\partial y}\bigg|_{y=0}, \tag{3.1}$$

where $f_1(x, y, z, t)$ is the streamwise component of the immersed boundary method body force, $\mathcal{V}$ is the volume of the simulation domain, and L_{x_i} is the domain length in x_i direction. For the two rough surfaces considered herein, the second term on the right-hand-side of Equation (3.1) is negligible. The friction velocity is then obtained as $u_\tau(t) = \sqrt{\tau_w/\rho}$. The corresponding friction Reynolds numbers are tabulated in Table 3.1; the sandgrain roughness (case S) produced higher wall friction than the multiscale roughness (case T). Grid sizes of the uniform mesh in x and z are shown in wall units in Table 3.1. In y, the grid is refined near the wall. At the final steady state (i.e. the more critical one for spatial resolution between the two steady states), $\Delta y^+_{\text{min}} < 0.3$ for SM and between 0.6 and 1.7 in the layer below roughness crest for the rough cases.

Surface	R_a/δ	k_c/δ	k_{rms}/R_a	s_k	k_u	ES_x	ES_z	y_R/k_c
S	0.014	0.09	1.05	0.48	2.97	0.43	0.44	1.10 ± 0.13
T	0.014	0.13	1.17	0.20	3.49	0.10	0.08	1.05 ± 0.10

Table 3.2 Characteristics of the rough surfaces.

Two different surfaces roughness, one synthetic sandgrain roughness 'S' and one replicated from a surface scan on a hydraulic turbine blade 'T', are used in the simulations. Figures 3.1(a) and (b) compare the roughness geometries and the power spectral density of their height fluctuations. Case S showed a prominent spectral peak at the separation length between neighboring grains in x and z, denoted by λ_s, while the T roughness resembled a fractal roughness with a spectral power decay of -2, without a dominant peak at a particular length scale. For further discussion regarding the height power spectral densities, see [2].

Parameters of the two rough surfaces are compared in Table 3.2. Both surfaces shared the same first-order (R_a) and similar second-order moments (k_{rms}) of height statistics, but quite different values of maximum peak-to-trough height (k_c, also called crest height), skewness (s_k) and effective slope (ES) in x or z. Both surfaces are positively skewed (i.e. peaky), with kurtosis values of around 3. Compared to S, the T roughness displayed sparser distribution of peaks, leading to a lower skewness value and milder effective slopes. The thickness of the RSL (i.e. y_R, defined as the layer in which $\langle \widetilde{u}^2 \rangle^{1/2}(y)/\langle \overline{u} \rangle(y) > 0.1$) is around 1.1 times of k_c in both cases. y_R varied mildly (within around 10%) throughout the transient process. The domain lengths in x and z are 12δ and 6δ, respectively, for cases SM and S, and both 12δ in case T to accommodate its large in-plane roughness length scales in both x and z. For case S, the spatial resolution of the grain geometry is 8 and 16 points per grain in x and z, respectively. For case T, there is no dominant roughness length scale. The Taylor micro-scale (λ_T) [64; 4] is thus used to quantify the length of an equivalent roughness element. λ_T is resolved by around 10 points in both x and z.

3.3 Summary of turbulence statistics

Some observations on flow statistics are summarized here to provide a context for the structural and other analyses reported in Section 3.4. For comprehensive discussions of the flows, see [2].
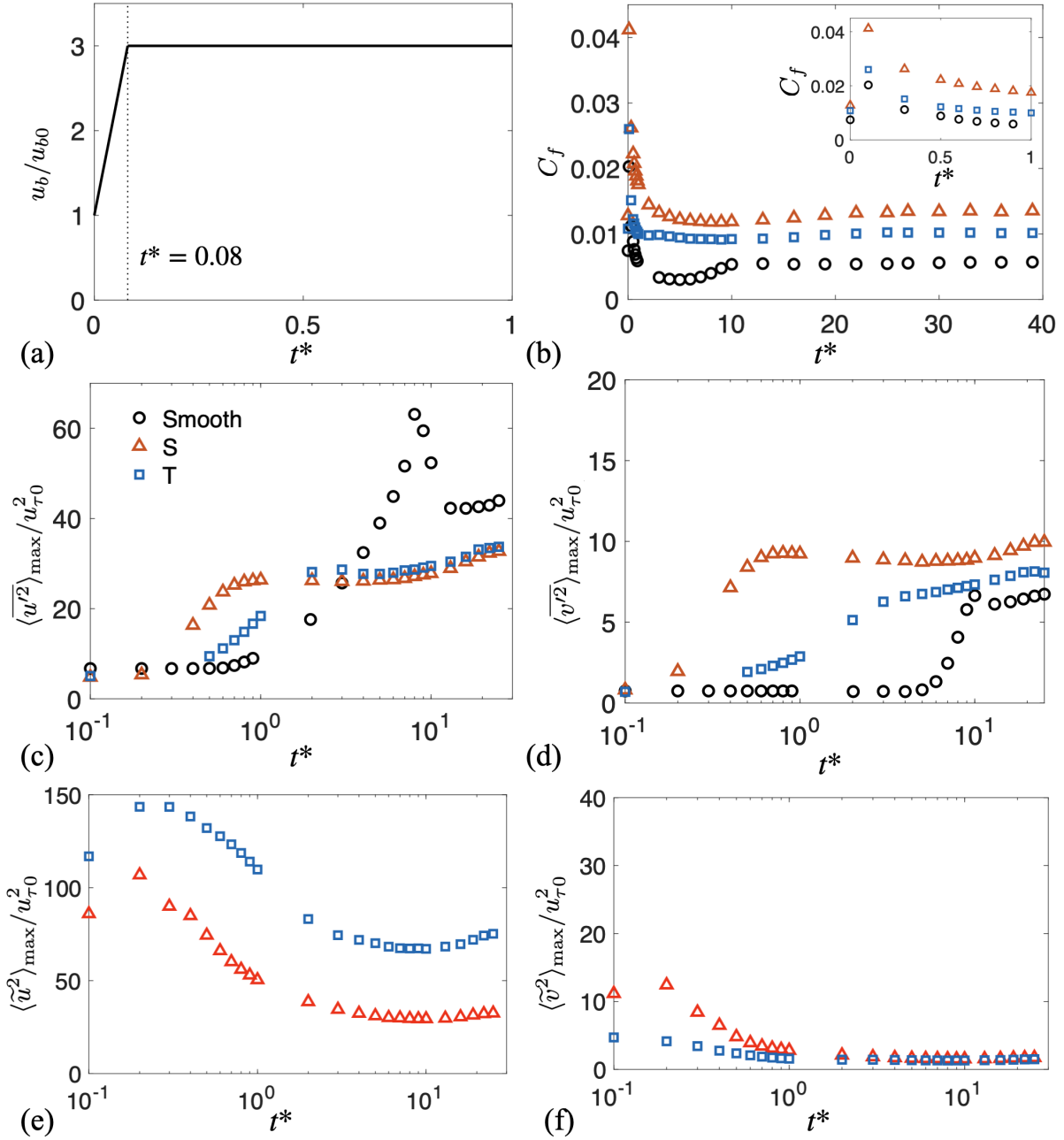
Figure 3.2 Flow statistics of the transient channels: (a) bulk velocity, (b) friction coefficient, and wall-normal maximum values of streamwise and vertical normal Reynolds stresses (c,d) and form-induced stresses (e,f). (b-f) are reproduced from [2] with permission.

3.3.1   Structural characteristics of turbulent velocity

(a)

(b)

(c)
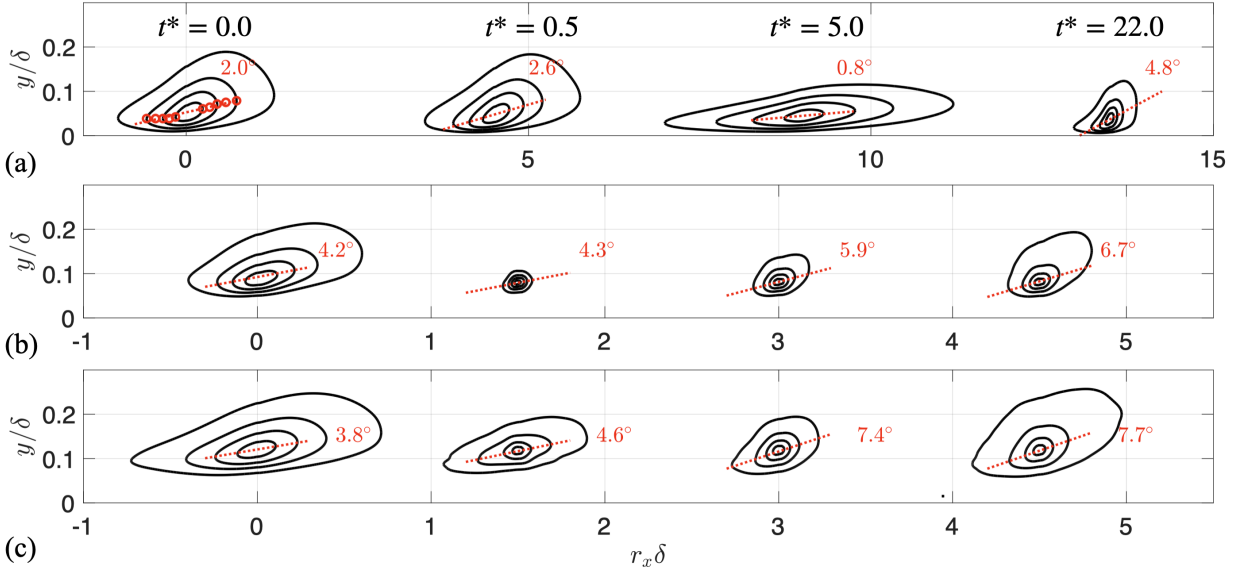
Figure 3.3 Contours of R_{11} at levels 0.3(0.2)0.9 in Cases SM (a), S (b) and T(c), at four time instances: $t^* = 0.0, 0.5, 5,$ and 22. $\cdots$ Lines fitted based on outermost points (an example is shown with ∘ in (a)) at contour levels 0.5(0.1)0.9, to show inclination angles (marked in red). For clarity, a shift of 4.5 and 1.5 units are used for smooth and rough cases, respectively.

Figure 3.2(a) showed the acceleration of u_b that is imposed in all cases. The friction coefficient $C_f = 2\tau_w(t)/(\rho u_{b0}^2)$ is compared in Figure 3.2(b). C_f underwent a sudden increase for all cases immediately following the u_b ramp-up, and decreased rapidly as the flow starts to recover. Figures 3.2(c-f) highlighted the differences in Reynolds and form-induced stress developments in the three cases.

On the smooth wall, turbulence undergoes reverse transition toward a quasi-laminar state, characterized by a dip of C_f below its long-time value and high Reynolds stress anisotropy (with TKE mostly resting in u'), caused by a delayed response of the TKE redistribution to the acceleration. On the rough walls, however, a clear dip of C_f is absent, and Reynolds stress anisotropy stayed almost unchanged. As opposed to the monotonic increase of u'_i fluctuations to a higher-Reynolds-number state, the $\widetilde{u}_i$ fluctuations displayed rapid augmentation following the u_b ramp-up and then decreased toward the long-time values. This variation of $\widetilde{u}_i$ intensity is shown to be a result of the variation of $\langle \overline{u} \rangle$ at the edge of the RSL; the ratio between the root-mean-square (RMS) of $\widetilde{u}_i$ and $\langle \overline{u} \rangle (y_R)$ is shown to be almost constant for each rough case.

3.4   Results

First, the two-point auto-correlation of the turbulent velocity u'_i centered at an elevation y_{ref} is calculated as

$$R_{11}(r_x, r_y, t) = \frac{\overline{\langle u'(x, y_{ref}, z, t) u'(x + r_x, y_{ref} + r_y, z, t) \rangle}}{\langle \overline{u'^2} \rangle (y_{ref}, t)}, \tag{3.2}$$

where r_x and r_y are separations in streamwise and wall-normal directions, respectively. The intrinsic averaging operator in the nominator on the right-hand-side of Equation (3.2) indicated that only contributions from products with both points ($\vec{x}$ and $\vec{x} + \vec{r}$) in the fluid domain are accounted for in calculating the correlation. Contours of R_{11} in the (x, y) plane are shown in Figures 3.3 for all cases at $t^* = 0.0, 0.5, 5$, and 22. In the smooth case, the correlation is centered at $y_{\mathrm{ref},0}^+ = u_{\tau 0} y_{\mathrm{ref}}/\nu = 10$, which corresponded to the peak elevation of the TKE production at $t^* = 0$, while in the rough cases $y_{\mathrm{ref}}/k_c = 1$, which is near the peak elevations of normal Reynolds stresses [2]. Following [18], the inclination angle θ is calculated using the best fitted line by the linear least square method, based on the points farthest away from the self-correlation point at $(r_x, r_y) = (0, 0)$, both upstream and downstream on the contour lines with levels from 0.5 to 0.9. These outermost points used for line fitting are shown in the R_{11} contours at $t^* = 0.0$ in Figure 3.3(a), as an example. The values of θ are listed in the figure. To compare quantitatively the size and inclination of the two-point correlations, Figure 3.4 showed temporal variations of the streamwise integral length (L_{11}) and θ in all cases. Here, L_{11} is calculated as the integral of R_{11} along r_x from $r_x = 0$ to the r_x value at which R_{11} first decreased below 0.3. A number of y_{ref} elevations (not shown) are used to evaluate the dependencies of both L_{11} and θ on y_{ref}; no significant differences in the comparison among cases and times are observed.

For case SM, in the reverse transition stage (shown at $t^* = 5$), L_{11} increased significantly, accompanied by a much reduced θ, before both quantities recover toward the long-time values at $t^* \approx 13$. The elongation of coherent u' motions (i.e. low speed streaks) is also observed for equilibrium accelerating turbulence such as the sink flow [79] and turbulent boundary layer subjected to FPG [47]. In both rough cases, on the other hand, L_{11} reduced rapidly, immediately after the step acceleration, reaching a minimum at $t^* \approx 0.4$ for case S and at a later time, $t^* \approx 2.0$, for case T. After then, L_{11} slowly increased toward the long-time values. During this time, an overall monotonic increase of θ is observed on the rough walls. The change in roughness texture only affected quantitative aspects of the large u' motions, but not their trends: the multiscale roughness yielded slower variations of both L_{11} and θ following the acceleration at $t^* = 0$.

Now focus on the initial ($t^* = 0$) and late-time states ($t^* = 22$). In the presence of sandgrain roughness, the x extent is shorter than that in the smooth case at both times. This is because the sandgrain elements are much smaller than δ; it imparts its length scale to the near-wall flow by breaking up long streaky motions near the wall. On the multiscale roughness, however, the initial x extent is closer to that in the sandgrain case, while at late times it approaches the smooth-wall values. This suggested that the streaks are broken up only by the sparsely distributed peaky elements, which are separated by large roughness scales. As the Reynolds number increased after the acceleration, the streaks appeared less affected, as the streamwise distances separating the peaky elements approached the order of magnitude of smooth-wall streak lengths, $o(10^3)\delta_\nu$.

41
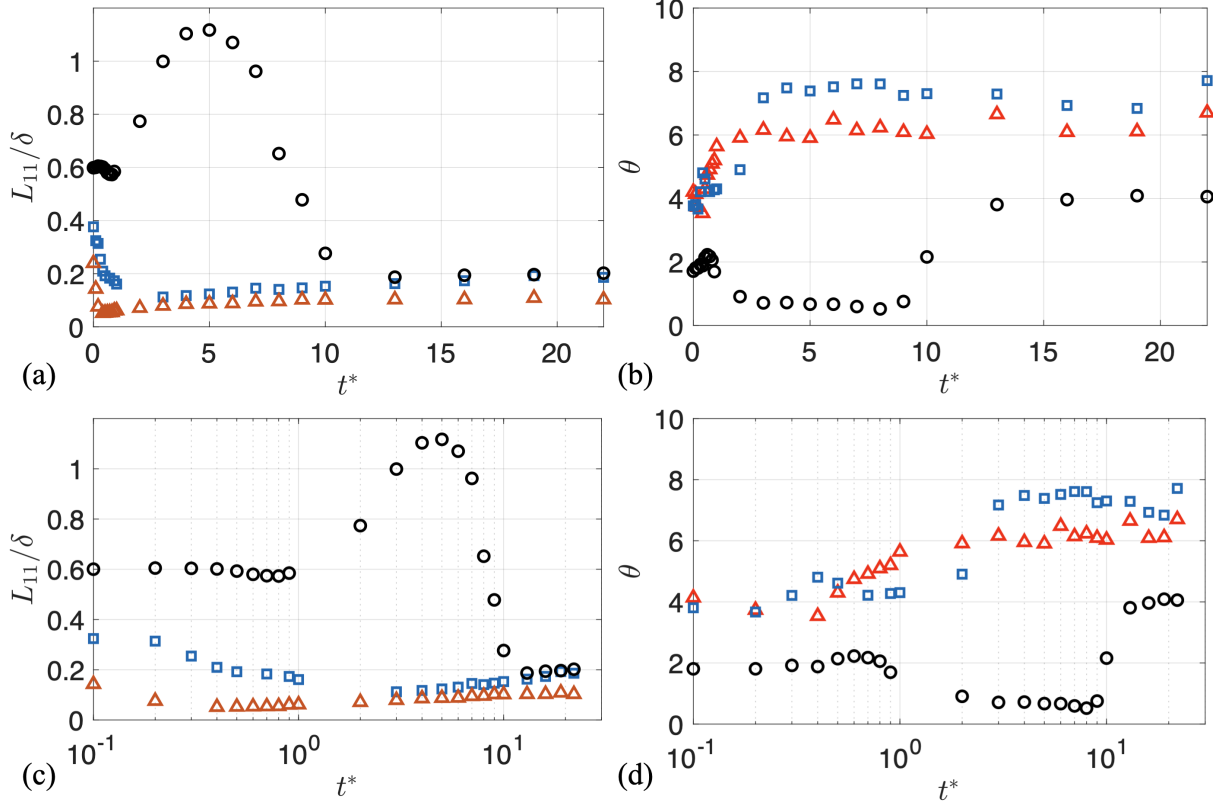
Figure 3.4 Temporal variation of streamwise integral length (a,c) and inclination angle (b,d) based on R_{11} in SM ($\circ$), S ($\triangle$), T ($\square$) cases. The correlations are centered at $y_{\text{ref,0}}^+ = 10$ for SM and $y_{\text{ref}}/k_c = 1$ for S and T. (a,c) show linear scalings of t^* and (c,d) show logarithmic scalings.

To characterize turbulent motions of all sizes, the premultiplied one-dimensional (1D) power spectra ($\kappa_1 E(\kappa_1)$) of u' and v' with streamwise wavenumber $\kappa_1 = 2\pi/\lambda_1$ (where λ_1 is the streamwise wavelength) are shown in Figures 3.5. First, a remark is given on the DNS spatial resolution, which is deemed sufficient if the wavenumber of the largest energy-containing motions and the highest physically "meaningful" wavenumber are two or more decades apart [92]. The highest meaningful wavenumber is the κ_1 value at which the effective resolution, quantified by an effective wavenumber $\kappa_{1,\text{eff}}^* = \kappa_{1,\text{eff}}\Delta x/\pi$ [93], reached its maxima. For the present second-order central-difference scheme, the effective wavenumber of the first derivative $\kappa_{1,\text{eff}}^* = \sin(\kappa_1^*\pi)/\pi$ [93] obtained a maximum at $\kappa_1 = \pi/(2\Delta x)$. Since the effective wavenumber droped for κ_1 higher than this value, the simulated fluid motions at scales smaller than $\pi/(2\Delta x)$ are not physically meaningful. Figures 3.5(a-c) showed that $\pi/(2\Delta x)$ is around two decades higher than the δ scale in all cases, satisfying the criterion of [92] for DNS spatial resolution.

42
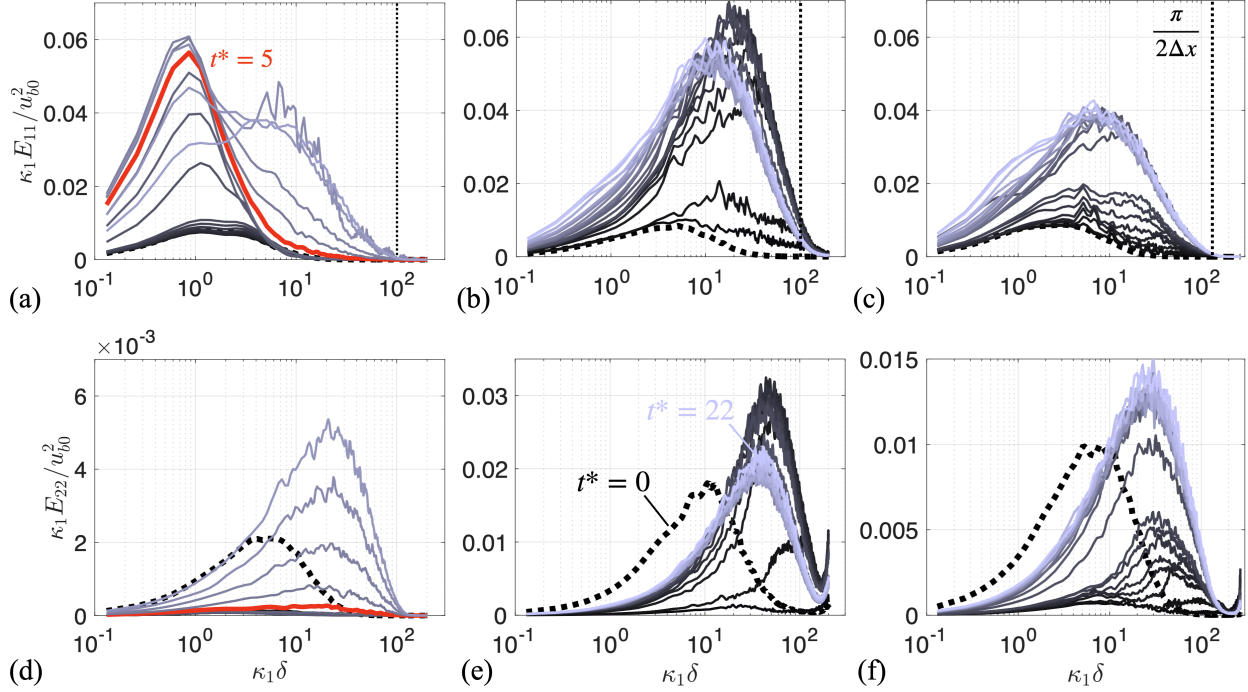
Figure 3.5 1D premultiplied power spectra of u' (a-c) and v' (d-f) at $t^* = 0$ (⋯) and a series of times (——, t^* values from 0.1 to 0.9 with step 0.1, from 1 to 9 with step 1, and from 10 to 22 with step 3, lighter colors at later times), in smooth-wall case (a,d) at $y^+ = 10$ and cases S (b,e) and T (c,f) at $y = k_c$. In (d-f), E_{22} at $t^* = 0$ is scaled by a factor of 15 for clarity. In (a-c), --- (vertical): highest physically meaningful wavenumber. In (a,d), the profile corresponding to $t^* = 5$ (discussed in text) is highlighted in red.

Figures 3.5(a,d) showed that, for the smooth-wall case, in the reverse-transition phase (e.g. at $t^* = 5$ marked in red) the energy of u' motions is concentrated at large scales of order δ, with only slight changes in the peak location of the v' spectrum. This is consistent with the streamwise elongation of turbulent coherent motions observed in a quasi-laminar flow [44; 58]. On the other hand, case S (Figures 3.5 (b,e)) does not show an increase of the low-wavenumber u' content. Instead, the peaks of both u' and v' power spectra shift monotonically toward the dominant length scale of the roughness geometry (i.e. distance between centers of neighboring grains, λ_s, shown in Figure 3.1(b) as $\kappa\lambda_s \approx 50$). One can infer that the v' associated with the new turbulence generated around the sandgrain roughness had a characteristic streamwise length of the grain separation, and that the u' motions are of lengths two to three times as long, which probably reflects channeling phenomena between grains. In comparison to the sandgrains, the T roughness (Figures 3.5 (c,f))—characterized by a wide spectrum of length scales up to around 6δ—led to a large portion of u' being distributed in the scales between $o(\delta)$ and $o(0.1\delta)$ during the transient process. One similarity can be seen between case T and the smooth case: both cases showed an amplification of the large-scale u' content at early times (though to a lesser extent in case T), Suggesting that, similar to the smooth case, streamwise-elongated eddies are also present around T roughness during the response to

43

acceleration.

3.4.1 Time scales of mean-flow strain rates

The previous section showed that time-variation of the structure of near-wall turbulence depended on the in-plane scales of roughness, with flow over the multiscale T roughness displaying some similarities with that on a smooth wall in terms of velocity coherence length and spectra. Past studies on smooth-wall turbulence attributed the observed streamwise elongation of inclined near-wall turbulent eddies to the stretching due to mean shear, which is quantified using a time-scale ratio (also called "shear rate parameter"), between the turbulence time scale and the time scale of the mean shear. For a transient channel, the time-scale ratio is

$$S^* = \frac{\overline{S}(y,t)\, q^2(y,t)}{2\epsilon(y,t)}, \tag{3.3}$$

where

$$\overline{S}(y,t) = 2(\overline{S}_{ij}\overline{S}_{ij})^{1/2}, \tag{3.4}$$

$$\overline{S}_{ij}(y,t) = \frac{1}{2}\left(\frac{\partial\langle\overline{u}_i\rangle}{\partial x_j} + \frac{\partial\langle\overline{u}_j\rangle}{\partial x_i}\right), \tag{3.5}$$

q^2 is twice the TKE, and ϵ is the TKE dissipation rate. q^2/ϵ represented roughly the time required for the energy of an energy-containing eddy to fully break down to motions in the dissipative subrange through the energy cascade process. [94] showed that, for homogeneous turbulence under a strong uniform mean shear, the turbulent eddies are distorted by the mean flow so rapidly that they are simply stretched, other than passing down the effect into smaller-scale eddies through the cascade. In other words, the turbulence time scale is much larger than that of the mean shear, reflected by $S^* \gg 1$. [88] showed that high S^* values between 30 and 40 imposed in initially homogeneous turbulence (without presence of a wall) can produce turbulent velocity and vorticity anisotropies similar to those observed near the wall in a channel flow. [58] demonstrated that in the region of quasi-laminar flow in a strongly accelerated smooth-wall boundary layer, near-wall S^* values reached up to around 60, compared to a value around only 10 on a rough wall where reverse transition is prevented. In the logarithmic region of the flow, S^* is around 4 to 5, a result of locally equilibrium turbulence.

The y profiles of S^* in all cases are compared in Figure 3.6. Here, the only non-zero component of the $\overline{S}_{ij}$ tensor is the 12 component, $\partial\langle\overline{u}\rangle/\partial y$. In the smooth case, high magnitudes of S^* near 70 are achieved at $t^* \approx 5$ near the wall, expected for the reverse transition process. In the presence of roughness, the wall-normal peak of $S^*(y)$ occured near the roughness crest, where the y gradient of $\langle\overline{u}\rangle$ is the strongest. The S^* peak values stayed between 5 and 15 throughout the transient, much lower than those in the smooth case, suggesting that the rough-wall DA flow is not strong enough to linearly reshape turbulent eddies. Far from the wall ($y/\delta > 0.1$, or $y^+ > 100$ herein), S^* values are

44

at around 5 at all times, regardless of wall condition. In case T near $y = 0$, one observed significant fluctuations of S^* values. This is probably due to fluctuations in the y-gradient of the roughness geometry function (or fluid area fraction), $\Phi(y)$, in case T, through its involvement in the intrinsic averaging process, $\langle \theta \rangle = 1/(\Phi A_o) \int_{A_f} \theta \mathrm{d}A$ (where A_o is the total planar area). See details of Φ in the Appendix. Using superficial averaging, however, would mask these fluctuations as $\langle \cdot \rangle_s = \Phi \langle \cdot \rangle$ and $\Phi \approx 0$ near the wall.
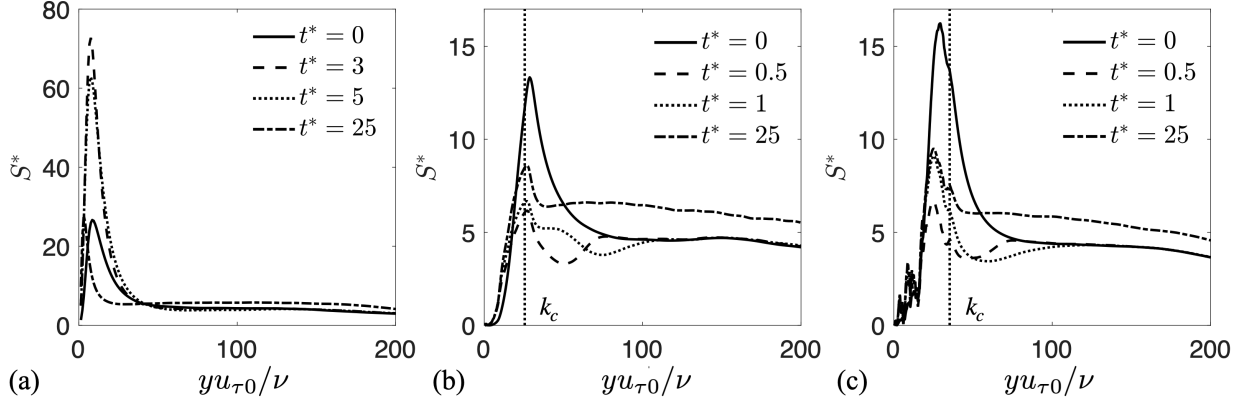
Figure 3.6 Variation of S^* for (a) SM , (b) S , and (c) T cases in time. In (b) and (c), vertical dotted lines indicate roughness crest height.

The discussions above, as well as those in [58], focus on the ratio between global (space-averaged) time scales of turbulence and double-averaged mean strain, instead of the local values. However, in rough-wall cases the strongly heterogeneous $\widetilde{u}_i$ inside the RSL may yield local time scale ratios much higher than the global value. In particular, Figure 3.2 showed that, within a short time after the impulse acceleration (at $t^* \approx 0.3$), the peak of $\langle \widetilde{u}^2 \rangle$ reached one order-of-magnitude higher than that of $\langle \overline{u'^2} \rangle$. This is expected to yield strong local gradients of form-induced velocity inside the RSL, which is quantified next.

We defined a time-scale-ratio tensor, S_{ij}^{*f}, to quantify the various strain rate components of $\widetilde{u}_i$. It is similar to the definition of S^*, but based on the form-induced velocity instead of the DA one,

$$S_{ij}^{*f}(y,t) = \left\langle \left| \frac{\widetilde{S}_{ij}\, q^2(x,y,z,t)}{\epsilon(x,y,z,t)} \right| \right\rangle, \tag{3.6}$$

where $\widetilde{S}_{ij}$ is the rate-of-strain tensor of $\widetilde{u}_i$,

$$\widetilde{S}_{ij}(x,y,z,t) = \frac{1}{2}\left(\frac{\partial \widetilde{u}_i}{\partial x_j} + \frac{\partial \widetilde{u}_j}{\partial x_i} \right), \tag{3.7}$$

and the superscript "f" indicated that the time-scale ratio is calculated using the form-induced velocity. Note that, different from the S^* definition in Equation (3.3), local values of three-dimensional ensemble-averaged q^2 and ϵ are used here to evaluate the local time scale ratio. S_{ij}^{*f} components are negligible for the smooth-wall flow.

45
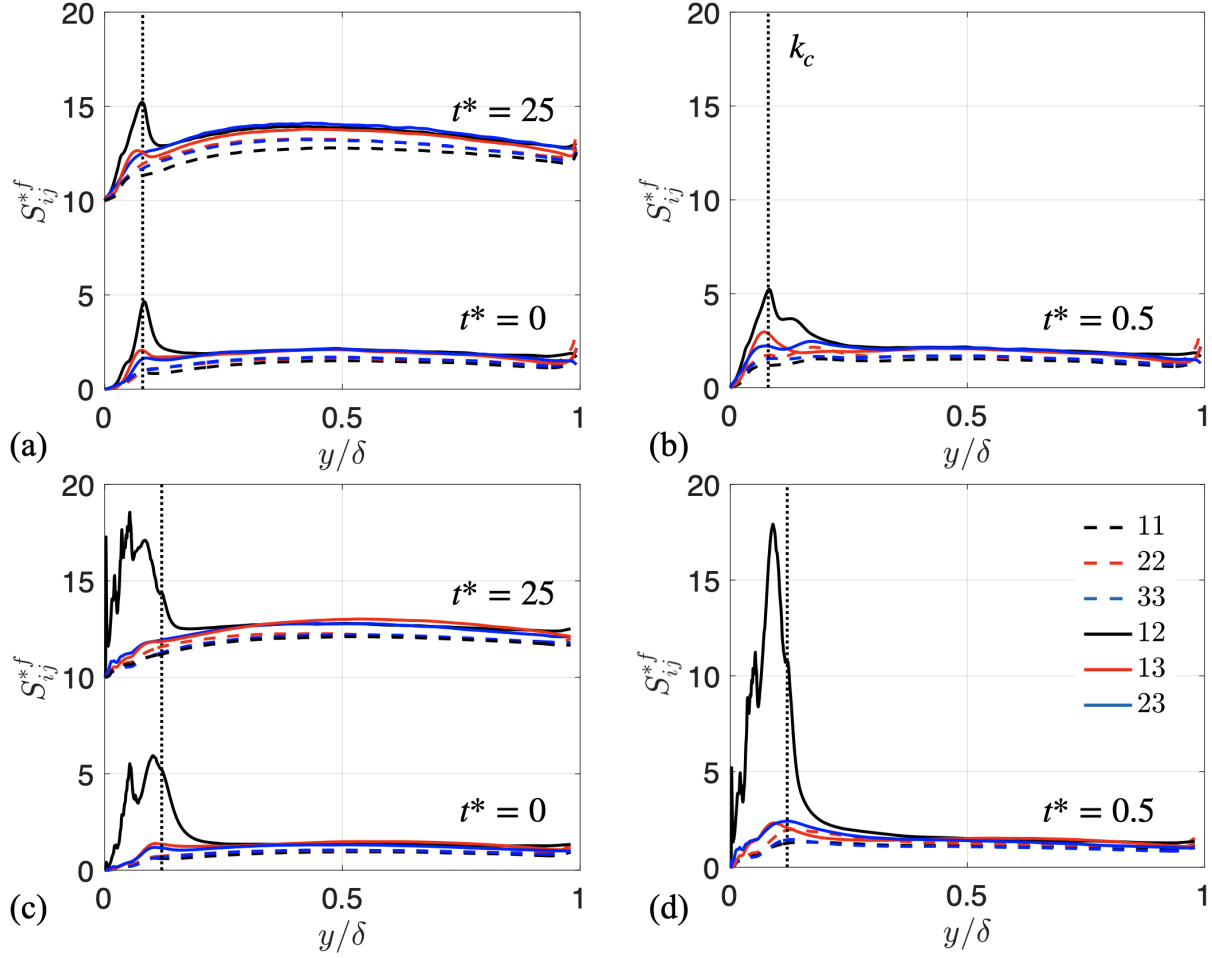
Figure 3.7 Time-scale ratios of $\widetilde{u}_i$ strain rates for (a-b) S and (c-d) T cases at three times: steady state $t^* = 0$ and long-time state $t^* = 25$ (a,c), as well as a transient state $t^* = 0.5$ (b,d). Profiles corresponding to $t^* = 25$ are offset upward by 10 units for clarify. Vertical dotted lines indicate roughness crest height.

Wall-normal profiles of all independent components of the S_{ij}^{*f} tensor in both rough cases are compared in Figures 3.7. The r.m.s. values of $\widetilde{S}_{ij}$ are used in the Equation (3.6) to calculate S_{ij}^{*f}. The regions of negative $\widetilde{S}_{ij}$ (indicating contraction of time-mean coherent motions) are expected to be limited to small regions near the small wavelength rough peaks, indicating a lower contribution to the overall r.m.s values. Among all, the 12 component is the dominant component for both cases, at all times. Within the 12 component, we found that $\partial \widetilde{u}/\partial y$ is significantly larger than $\partial \widetilde{v}/\partial x$, as $\widetilde{u}$ is the dominant form-induced velocity component. Overall, the plane-averaged form-induced strain rate is similar or weaker compared to the strain rate of $\langle \overline{u_i} \rangle$ during the transient process, with the exception of the 12 component in case T at early stage of the transient (shown at $t^* = 0.5$), which increased to around 18 below the crest elevation. This is roughly 2.5 times the shear rate of $\langle \overline{u_i} \rangle$ at this time (Figure 3.6c). The higher plane-averaged form-induced time-scale ratio on T roughness than on S can be attributed to a stronger $\partial \widetilde{u}/\partial y$, resulting from more intense $\widetilde{u}$ on T

roughness than on S (Figure 3.2e), together with almost identical RSL thicknesses (Table 3.2). In addition, the comparison between the time-scale ratios at the initial and long-time states ($t^* = 25$) in Fig. 3.7(a,c) showed that they are similar, with the main difference being slightly higher values of S_{ij}^{*f} of all components in the outer region at $t^* = 25$ than those at $t^* = 0$. This is probably due to more intense high- and low-momentum pathways (as discussed by, for example, [23] and [95]) in the outer region under the higher Reynolds number. These pathways are discussed, for the present roughnesses and at a Reynolds number similar to the present long-time state, by [87]. On the T roughness, despite the much lower $\widetilde{u}_i$ strain rates than on the smooth wall in the spatial-average
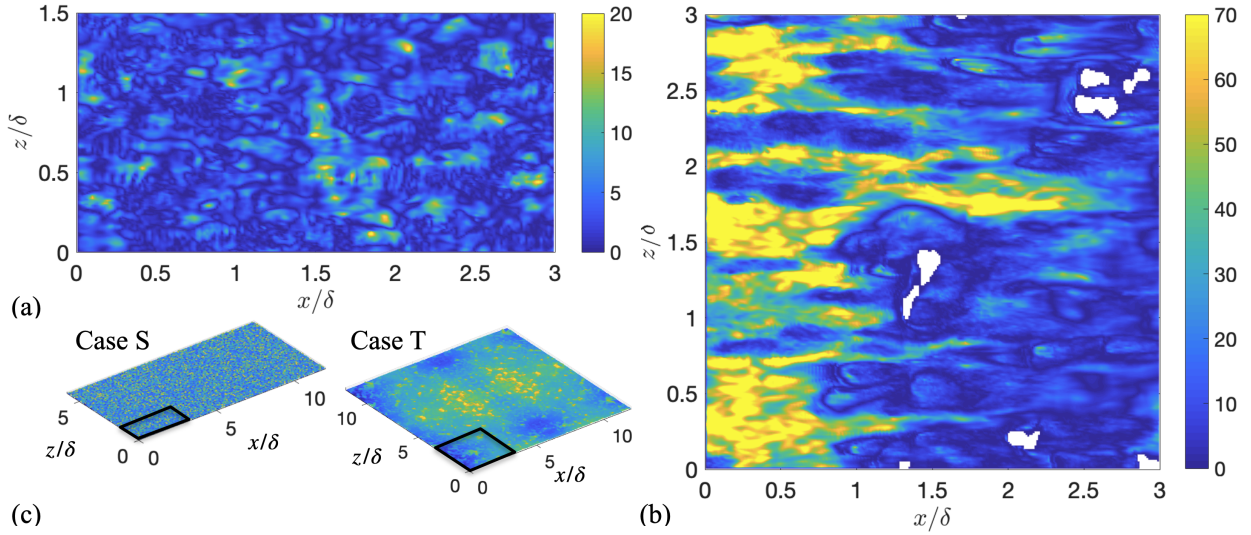
Figure 3.8 Contours of $\widetilde{S}_{12}q^2/\epsilon$ at $t^* = 0.5$, at respective peak elevations of $S_{12}^{*f}(y)$ profiles for cases S (a, at $y/k_c = 1$) and T (b, at $y/k_c = 0.75$), zoomed in to the regions shown in the full height maps in (c).

sense as seen by comparing Figures 3.6(a) and 3.7(d), locally the time scale ratio can achieve a level similar to that on the smooth-wall, due to heterogeneous nature of this roughness. Figure 3.8 compares wall-parallel contours of local contribution to S_{12}^{*f} on both rough walls at $t^* = 0.5$. The y elevations of the contours are selected as the respective peak elevations of the average time-scale ratios in the two cases according to Figure 3.7. Only a portion of the domain is shown for clarity. In case S, local time-scale ratio rarely exceeds 20, and thus the augmented form-induced straining during the transient process acted mainly to promote turbulence production. However, in case T high time-scale ratios are achieved locally in the regions between roughness peaks, with a large area of flow reaching a ratio of 60, similar to the values on a smooth wall.

To quantitatively compare the time-scale ratios in the two rough cases, the cumulative distribution functions (CDF) of $\widetilde{S}_{12}q^2/\epsilon$ in the whole (x, z) domain at the same y elevations are compared in Figure 3.9. For case T, around 20% of the fluid domain is subjected to local time-scale ratios higher than 30 (i.e. level seen in smooth-wall fully developed channels near the wall) and 5%
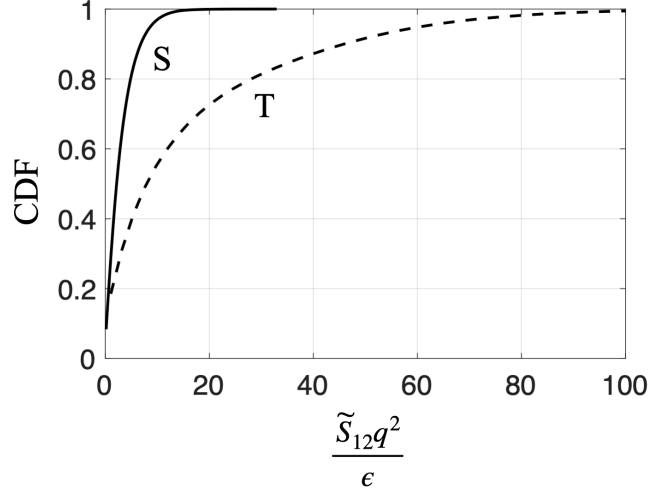
Figure 3.9 Cumulative distribution functions of local time-scale ratios of $\widetilde{S}_{12}$ shown in Figures 3.8(a,b).

corresponded to ratios higher than 60. Therefore, in the presence of large roughness length scales (with case T as an example), it is possible that strong positive values of $\partial \widetilde{u}/\partial y$ became locally important in early stage of the transient as it led to streamwise elongation of inclined turbulent eddies (indicated by R_{11} contours in figure 3.3c) near the wall. This is consistent with the changes in integral length scale shown in Figure 3.4 and in the u' spectra shown in Figure 3.5. Also, addition of S^* to $S_{ij}^{*f}(y,t)$ is expected to further increase the magnitude and occurrence of the positive values of $\partial \widetilde{u}/\partial y$, further emphasizing the above findings.

3.4.2 Sources of turbulent pressure fluctuations

Beside the more widely studied form-induced production, we suggested a second mechanism through which the form-induced velocities modified the Reynolds stress balance: indirect augmentation of TKE redistribution (i.e. Π in Equation 2.8) by intensifying turbulent pressure fluctuations, p'. One supporting evidence is that both form-induced velocity intensities and the TKE redistribution to v' through pressure-strain term increased rapidly at early times in the rough cases, as compared to a slow increase of TKE redistribution on a smooth wall [2].

The following is a selective summary of current understanding of how roughness affects p'. Based on DNS of rough-wall channel flows, [96] observed that roughness augmented pressure fluctuations throughout the boundary layer, and that the RSL thickness defined based on p' RMS is thicker that those based on u'_i or vorticity RMS. [97] characterized the wall-pressure spectrum and analyzed its scaling based on high-Reynolds-number experimental data. [98] showed with large-eddy simulations that roughness geometry and distribution modify wall-pressure fluctuations. Specially, intense pressure fluctuations occur on the front surface of roughness, instead of the back surfaces, suggesting that instantaneous impinging flow structures are more important than vortex shedding to wall-pressure RMS and generation of self noise. [35] examined the two p' source terms that are identified as the dominant ones in fully developed smooth-wall flows: the 12 component
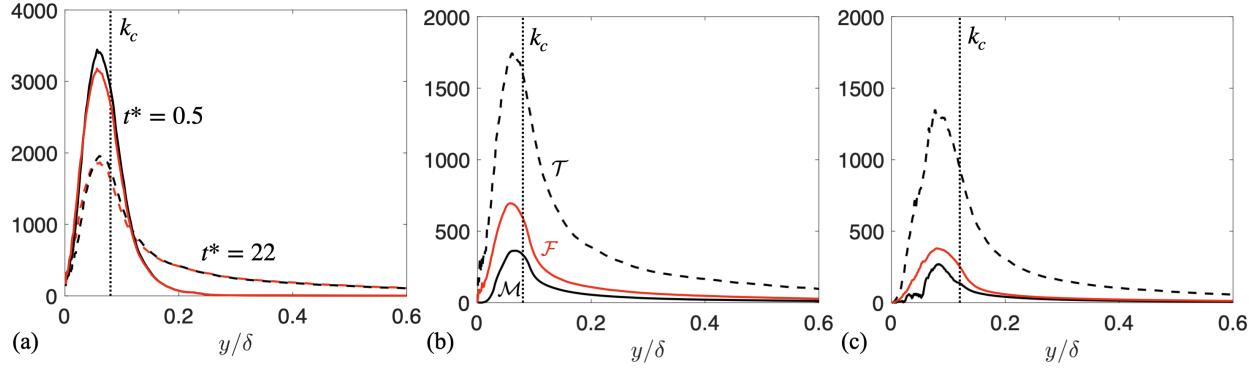
Figure 3.10 (a) RMS of the left-hand-side (red) and right-hand-side (black) of p' Poisson's equation (Equation 3.8) at $t^* = 0.5$ (——) and 22 (- - -) for case S. (b,c) Steady-state RMS of source terms in cases S (b) and T (c), evaluated at $t^* = 22$. All quantities are normalized using u_{b0} and δ.

of the mean shear term ("MS12" therein) and the 23 component of the turbulent-turbulent term, and concluded that the MS12 term is a more important source between the two on the rough wall. They also explained the links between these terms and local structure of the mean and turbulent velocities.

Due to non-zero $\widetilde{u}_i$ in rough-wall flows, an additional term (represented by $\mathcal{F}$) appears in the Poisson's equation of p',

$$\frac{1}{\rho}\nabla^2 p' = \mathcal{M}(x_i, t) + \mathcal{T}(x_i, t) + \mathcal{F}(x_i, t), \tag{3.8}$$

where the source terms are

$$\mathcal{M} = -2\frac{\partial \langle \overline{u_i} \rangle}{\partial x_j}\frac{\partial u'_j}{\partial x_i}, \tag{3.9}$$

$$\mathcal{T} = -\frac{\partial^2}{\partial x_i \partial x_j}\left(u'_i u'_j - \overline{u'_i u'_j}\right), \quad \text{and} \tag{3.10}$$

$$\mathcal{F} = -2\frac{\partial \widetilde{u}_i}{\partial x_j}\frac{\partial u'_j}{\partial x_i}. \tag{3.11}$$

Here $\mathcal{M}$ is the source due to gradients of double-averaged velocity (i.e. the 'mean shear term'), $\mathcal{T}$ is the turbulent-turbulent term, and $\mathcal{F}$ is the source due to the gradients of $\widetilde{u}_i$. It is unclear how these terms compare, since, to our knowledge, quantitative comparison of all terms had not been reported in the context of rough-wall flows.

In the following, we compare the magnitude of each source term as a function of time, for all cases. First, to estimate the accuracy of the source term calculation in the context of the immersed boundary method, the RMS of the left-hand-side and right-hand-side of Equation (3.8) are compared at various time instances in Figure 3.10(a), taking case S as an example. The RMS is calculated based on plane averaging using one snapshot at each time (i.e., without ensemble averaging) as $(\cdot)_{\text{rms}} = \langle (\cdot)^2 \rangle_s^{1/2}$, where $(\cdot)$ represented a local instantaneous flow quantity. The

49
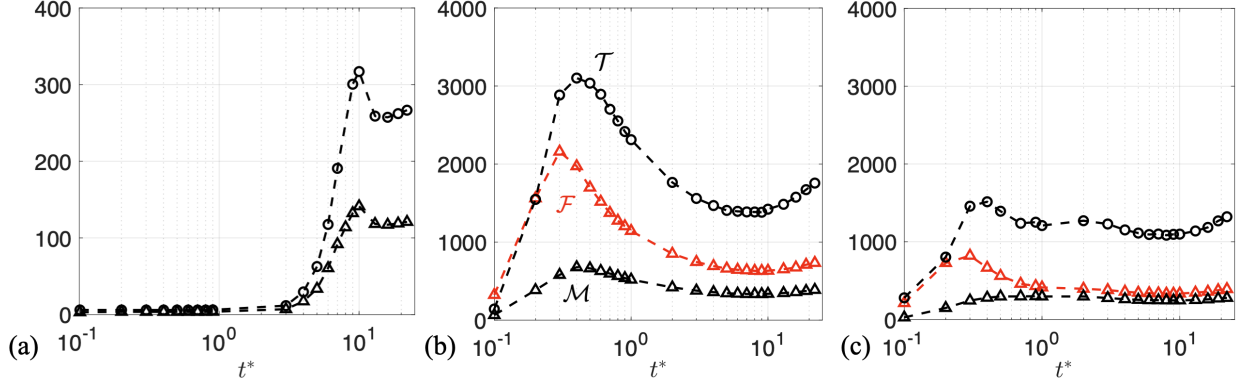
Figure 3.11 Temporal variations of RMS of p' source terms at their respective wall-normal peak elevations for the smooth case (a) and at $y = 0.7k_c$ for cases S (b) and T (c).

difference between the two sides of the equation is shown to be up to 5-8% of the local RMS values. This difference is attributed to discretization error of the finite difference scheme used to calculate the terms in Equation (3.8) and to the exclusion of grid cells that are cut by the fluid-solid interfaces when calculating these terms.

The y-profiles of the RMS of all terms near the new steady state ($t^* = 22$) are compared in Figure 3.10(b,c) between the two rough cases. Here both ensemble and plane averaging are used in calculating the RMS, obtained as $(\cdot)_{\mathrm{rms}} = \overline{\langle(\cdot)^2\rangle_s}^{1/2}$. [35] observed that the $\mathcal{M}_{12}$ term is more important than the $\mathcal{T}_{23}$ term, in connection with the presence of maximum $\partial\langle\overline{u}\rangle/\partial y$ inside the RSL and the $\partial v'/\partial x$ augmented by roughness. Surprisingly, the results here show that the least important source is $\mathcal{M}$ in both rough cases, when all components of all term are considered in the calculation. This is probably due to the relatively weak $\partial\langle\overline{u}\rangle_i/\partial x_j$ compared to the form-induced shear $\partial\widetilde{u}_i/\partial x_j$, as well as strong gradients of all u'_i components in the RSL. In addition, $\mathcal{T}$ is shown here to be the dominant source term regardless of roughness texture. All terms reach a peak slightly below the roughness crest. This is because that the peaks of form-induced stresses [40], Reynolds stresses, and DA mean shear [9; 99; 100] all reach their respective peak values near the roughness crest. In case T, the peaks of the source terms are located lower (toward the middle of the RSL), because of the rarer attainment of the maximum crest height by local roughness peaks due to the presence of large surface scales.

Next, the RMS values of each of the three source terms at a y elevation are evaluated for all times in Figure 3.11. For the smooth-wall case, as the peak elevations of different terms are not the same and vary with time, the source terms are evaluated at the instantaneous peak location of each term. In the rough-wall cases, however, all terms are evaluated at $y = 0.7k_c$, near the peak elevations of all source terms, independent of time. In the rough cases, the $\mathcal{M}$ term is the least important one not only at steady states, but also during the transient, as turbulence and form-induced velocities in the RSL adjust to the accelerated mean velocity rapidly. All terms increase instantly following the

50
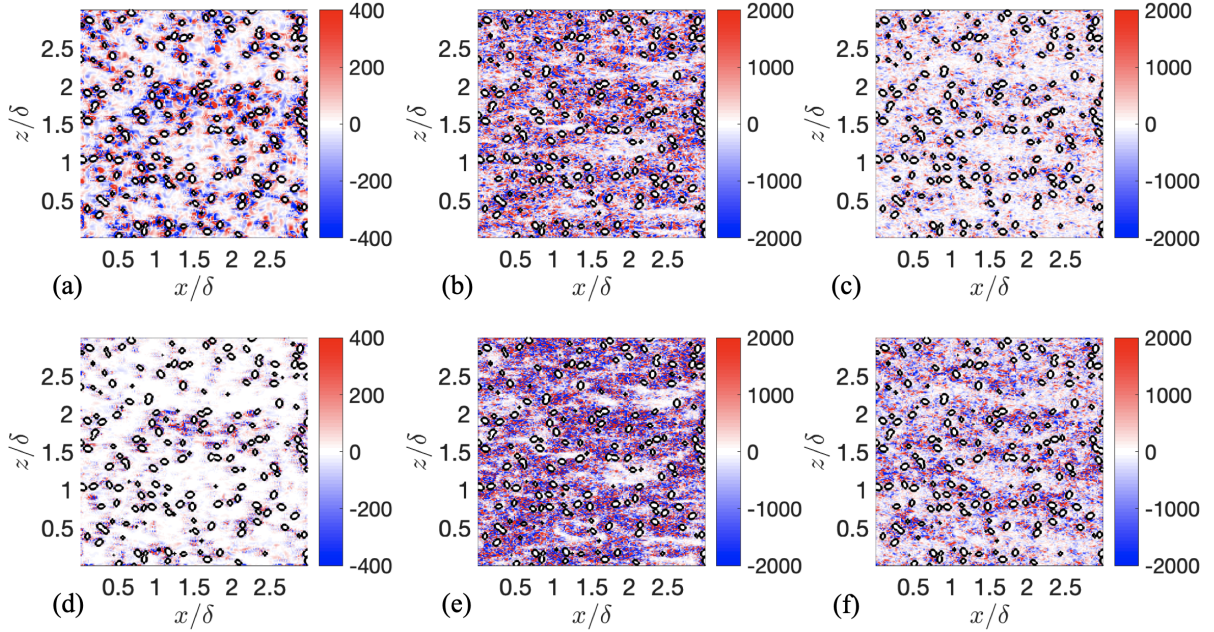
Figure 3.12 Contours of $\mathcal{F}$ (a-c) and $\mathcal{T}$ (d-f) at $y = 0.7k_c$ for cases S, at $t^* = 0.1$ (a,d), 0.5 (b,e), and 10 (c,f). Black contour lines mark fluid-solid interfaces. All quantities are normalized based on u_{b0} and δ. 1/8 of the domain is shown.

step acceleration on rough walls. Specifically, $\mathcal{F}$ becomes particularly significant in the early stage, due to the intensification of $\widetilde{u}_i$ (Figures 3.2(e,f)). The $\mathcal{T}$ term increased synchronously with $\mathcal{F}$, probably due to the intensification of TKE associated with stronger form-induced production. On the smooth wall, due to the absence of roughness and $\widetilde{u}_i$, the $\mathcal{T}$ term is not augmented immediately following the bulk acceleration. Instead, the turbulence is "frozen", signified by the persistence of source terms at the initial-state levels till $t^* \approx 3$. The decorrelation between mean flow acceleration and the developments of $\mathcal{M}$ and $\mathcal{T}$ terms are also observed in a smooth-wall boundary layer subject to strong spatial acceleration [44]. These results confirmed that characteristics of the form-induced velocity as contained in $\mathcal{F}$ are important for the p' evolution. They also suggested that the $\widetilde{u}_i$ distribution determines how turbulence responses to strong acceleration (with more evidence to be shown next).

Spatial distributions of $\mathcal{F}$ and $\mathcal{T}$ terms in both rough cases are compared in Figures 3.12 and 3.13, at three time instances: $t^* = 0.1$, $t^* = 0.5$, and $t^* = 10$. In both cases, regions with strong $\mathcal{F}$ and those with strong $\mathcal{T}$ are well correlated at all three time instances, as shown in Table 3.3 by the single-point cross-correlation between the two sources of values around 0.5 to 0.6. This suggested that early generation of new turbulence depends primarily on form-induced production. In other words, it appears that $\widetilde{u}_i$ strain rates form not just an important source of p', but also the origin of the other important source, $\mathcal{T}$.

In addition, comparison between Figures 3.12 and 3.13 highlighted the effect of roughness texture on the rate of increase of p'. First, focus on the largest source term, $\mathcal{T}$. At early times this

51
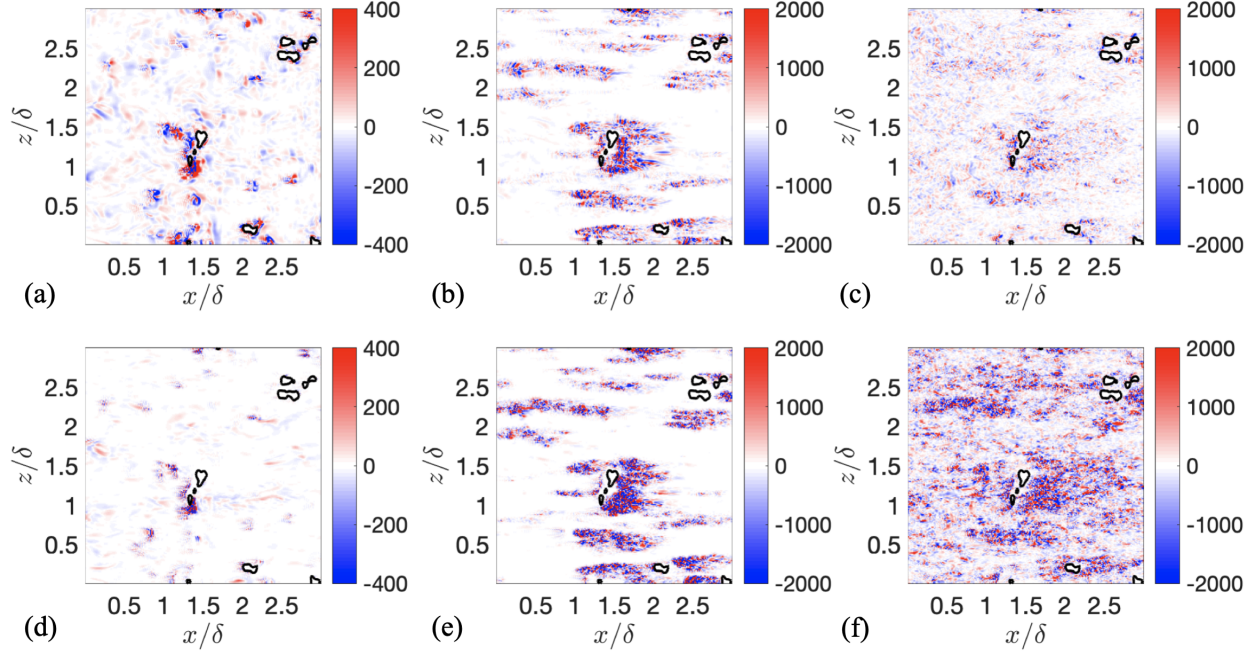
Figure 3.13 Contours of $\mathcal{F}$ (a-c) and $\mathcal{T}$ (d-f) at $y = 0.7k_c$ for cases T, at $t^* = 0.1$ (a,d), 0.5 (b,e), and 10 (c,f). Black contour lines mark fluid-solid interfaces. All quantities are normalized based on u_{b0} and δ. 1/16 of the domain is shown.

term takes high magnitudes in the vicinity of peaky roughness elements (e.g. see Figures 3.12(e) and 3.13(e)). In case S, the peaky elements associated with the tips of the grains are densely distributed, while in case T the roughness peaks are sparser, separated by large roughness scales. As a result, at early times ($0 < t^* < 0.3$) the rate of increase of $\mathcal{T}$ in case T is slower compared to that in case S, as shown in Figure 3.11. In addition, Figure 3.11 showed that, in case S, after $\mathcal{F}$ reached its peak in time at $t^* \approx 0.3$ and started to decrease toward the steady state, the $\mathcal{T}$ term followed the same trend and decreased from its peak (another evidence of the importance of form-induced production of TKE). In comparison, in case T the $\mathcal{T}$ term displayed only a slightly decrease following the decline of $\mathcal{F}$ at $t^* \approx 0.3$. Examination of Figure 3.13(e,f) explained that this almost constant $\mathcal{T}$ level in case T for $t^* > 0.3$ is due to a combination of both the weakening of local $\mathcal{T}$ values (due to a decrease in $\mathcal{F}$) and the delayed activation of other regions in producing intense turbulent fluctuations.

Case	$t^* = 0.1$	$t^* = 0.5$	$t^* = 10$
S	0.52	0.56	0.56
T	0.53	0.48	0.50

Table 3.3 Single-point cross-correlation between $\mathcal{F}$ and $\mathcal{T}$ contours shown in Figs. 3.12 and 3.13. The correlation is defined as $\langle |\mathcal{F}| \cdot |\mathcal{T}| \rangle / [\langle \mathcal{F}^2 \rangle^{1/2} \cdot \langle \mathcal{T}^2 \rangle^{1/2}]$.

To further characterize the $\mathcal{F}$ term, individual components $-2(\partial \widetilde{u}_\alpha / \partial x_\beta)(\partial u'_\beta / \partial x_\alpha)$ are compared in Figure 3.14. For case T, the 12 term $-2(\partial \widetilde{u} / \partial y)(\partial v' / \partial x)$ is significantly higher than other terms at all times. This is because that the large roughness scales induced significant $\widetilde{u}$ in the
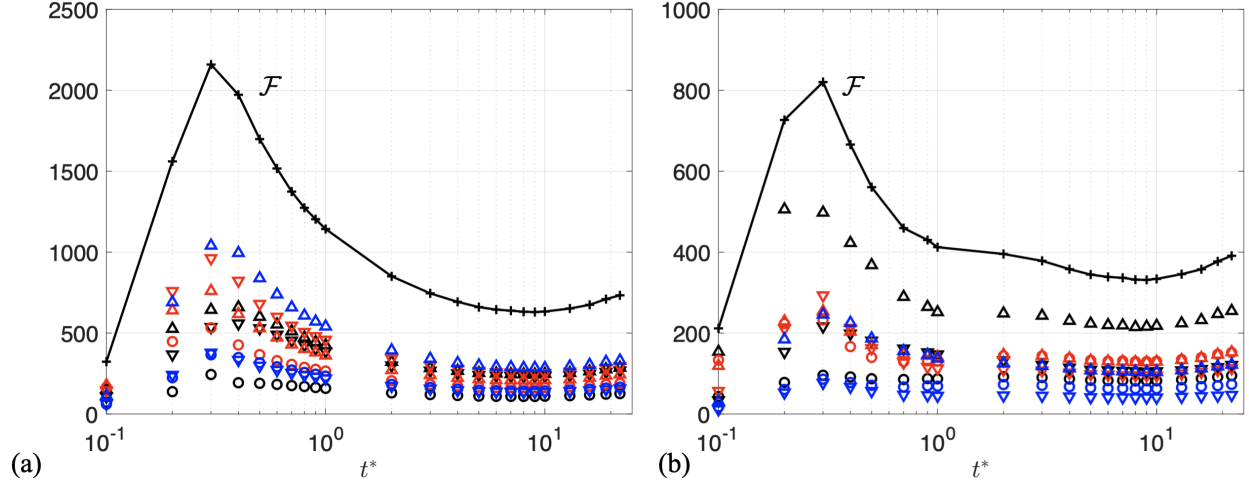
Figure 3.14 Temporal variations of the RMS of individual terms in $\mathcal{F}$ for cases S (a) and T (b). Symbols: + sum of all terms, $\bigcirc$ 11, $\triangle$ 12, $\triangledown$ 13, $\bigcirc$ 21, $\triangle$ 22, $\triangledown$ 23, $\bigcirc$ 31, $\triangle$ 32, $\triangledown$ 33.

RSL [40]. In case S, however, the 32 and 23 terms are the largest ones, while other terms are also significant. The difference between the two cases highlighted the dynamical importance of $\widetilde{v}$ and $\widetilde{w}$ around densely distributed roughness, versus that of $\widetilde{u}$ in the case of a multiscale roughness.

3.5 Conclusions

This work evaluated various pathways through which the form-induced velocity $\widetilde{u}_i$ affected turbulent flows in equilibrium and non-equilibrium states, based on DNS data of transient turbulent half channels in response to a three-fold step acceleration of bulk velocity at time $t^* = 0$. Two roughness geometries—a densely distributed synthesized sandgrain roughness (case S) and a multiscale turbine-blade roughness (case T)—are imposed on the channel wall; a baseline smooth-wall case (case SM) is also compared. The two roughness geometries shared similar first and second moments of roughness height fluctuations, but differ in in-plane scales.

Analyses of two-point turbulent velocity correlations in the transient flow showed that, opposed to the smooth-wall cases where energy-containing motions are elongated in x and decrease in inclination angle as signatures of the reverse transition process, on the rough walls the streamwise coherence decreases rapidly after the acceleration and the inclination angle increases sharply. Energy spectra, on the other hand, highlight a difference between the rough cases: while in case S the spectral peaks of u' and v' motions monotonically shift toward characteristic scales of the sandgrains, in case T the u' motions are initial augmented at large scales; the latter suggests local streamwise elongation of velocity streaks similar to the smooth-wall case to some extent.

We show that the dependence of turbulent structure on the in-plane scales of roughness described above may be explained by the local time-scale ratio between the $\widetilde{u}_i$ straining and turbulence. Although both strain rate of double-averaged velocity $\langle \overline{u}_i \rangle$ and the spatial-averaged local strain rate of $\widetilde{u}_i$ yielded much smaller time-scale ratios compared to values on a smooth wall, $\widetilde{u}_i$ is shown to give local time-scale ratios above 60 in case T at early times, in large areas between sparse peaks of

roughness. These values are similar to the level reached when the turbulence is relaminarized on a smooth wall. This result indicated that, in the presence of in-plane roughness scales of order δ, $\partial \widetilde{u}/\partial y$ may be important during the transient response and result in linear stretching of turbulent eddies.

Besides the additional form-induced production known to be important in transient channel flows [2], evidence of a second mechanism through which the form-induced velocity indirectly affected the Reynolds stress balance by augmenting p' is presented. We compared all three p' source terms in the roughness sublayer and found that, surprisingly, the least important one at all times is the source due to $\langle \overline{u_i} \rangle$ shear. Both the source due to $\widetilde{u_i}$ gradients and that due to u_i' are important, with the spatial distribution of the latter correlated with the former, probably due to the production of TKE from $\widetilde{u_i}$ shear.

This work provided evidences that the form-induced velocity inside the roughness sublayer is important for turbulence statistics and structure in wall-bounded turbulent flows. $\widetilde{u_i}$ gradients form an important source of p' in an equilibrium flow, while in a non-equilibrium accelerating flow they generate significant amount of TKE in the vicinity of roughness peaks and reshaped turbulent eddies in the regions between peaks.

CHAPTER 4
DATA-DRIVEN PREDICTIONS OF THE ROUGHNESS SUBLAYER FLOW

4.1 Introduction

Chapters 2 and 3 demonstrated the influence of roughness geometry on the turbulence evolution in a type of non-equilibrium wall turbulence and the important role played by the form-induced velocity ($\widetilde{u_i}$) in shaping the turbulence response, including evolution of turbulent eddies and Reynolds stress transport. The next question is to understand how roughness texture affects the form-induced stress. [40] studied the form-induced velocity distribution on rough surfaces with different length scales. They showed the occurrence of both positive and negative values of $\widetilde{u}$ to be dependent on the wavelengths of the surface. Additionally, the long-wavelength surface components in a multiscale surface led to lower occurrences of intense $\widetilde{v}$ and $\widetilde{w}$, leading to negligible form-induced shear stress unlike on a homogeneous sandgrain surface. Studies on regular arrays of cubes and on gravel-bed roughness by [101] and [37], respectively, observed large magnitudes of $\widetilde{u}$ and $\widetilde{v}$ leading to strong negative form-induced shear stress near re-circulation regions. These studies, among others, showed the dependencies of various components of the form-induced velocities on the roughness texture. However, past analyses were typically done for single types of rough surfaces only. The current work is focused on expanding the understanding to a wide range of rough surfaces.

Instead of analyzing the 3D $\widetilde{u}_i(x, y, z)$ field itself, it is proposed to address, in this chapter, low-dimension quantities that are essential for the transport of $\widetilde{u}_i$. The budget equation for the wake kinetic energy (WKE, i.e. $\langle \widetilde{u}_i \widetilde{u}_i \rangle / 2$) [36; 37; 38], in a periodic half-channel flow reads

$$-\langle \widetilde{u}_i \widetilde{v} \rangle \frac{\partial U_i}{\partial y} + \left\langle \widetilde{u_i' u_j'} \frac{\partial \widetilde{u}_i}{\partial x_j} \right\rangle_s - \frac{1}{2} \frac{\partial \langle \widetilde{u}_i \widetilde{u}_i \widetilde{v} \rangle_s}{\partial y} - \frac{\partial \left\langle \widetilde{u}_i \widetilde{u_i' v'} \right\rangle_s}{\partial y} \tag{4.1}$$

$$-U \left\langle \frac{\partial \widetilde{P}}{\partial x} \right\rangle + \frac{\partial \left\langle \widetilde{P} \widetilde{v} \right\rangle_s}{\partial y} + \nu \left\langle \widetilde{u}_i \nabla^2 \widetilde{u}_i \right\rangle_s = 0. \tag{4.2}$$

The two sources of production of $\widetilde{u}_i$ fluctuations are: (i) the production due to the mean shear (i.e. $\partial U / \partial y$, with $U \equiv \langle \widetilde{u} \rangle_s$), as shown by the first term on the left-hand-side in Equation (4.1), and (ii) the work of pressure drag of roughness (i.e. $-\langle \partial \widetilde{P} / \partial x \rangle$) against the mean velocity U, as shown by the fifth term on the left-hand-side. Therefore, understanding how both $U(y)$ (and $\partial U / \partial y$ by extension) and the pressure drag depend on the roughness geometry is essential in understanding how the roughness geometry controls WKE development and, in turn, the turbulence response in non-equilibrium flows.

First, past studies on the modeling of $U(y)$ based on roughness geometry are summarized below. [85] provided analytical derivation of $U(y)$ profiles for 2D, steady rough-wall turbulent flows based on the flow conditions, roughness geometrical function $\phi(y)$ (i.e. porosity) and the relative submergence of roughness. Specifically, roughness with constant ϕ produced an exponential

velocity profile, while a linear velocity profile is applicable to roughness with monotonically increasing $\phi(y)$. Another study by [100] over varying height, aspect ratio and distribution of rectangular-prism roughness elements predicted an exponential $U(y)$ profile with an attenuation factor obtained based on wake interaction within rough surfaces. [75] proposed a composite $U(y)$-profile model based on observations of the $U(y)$ of four different rough surfaces: sandgrain roughness, half ellipsoids, 2D wavy surface and a random surface generated with spatial Fourier modes. The composite model consists of a zero-velocity layer near the wall, combined with an upper layer with $U(y)$ prescribed based on a polynomial expression, which smoothly blends the zero-velocity layer and the logarithmic layer. The model coefficients are determined by fitting to DNS data of the four rough surfaces. The model is successfully integrated into channel-flow RANS simulations that did not resolve the RSL. However, the composite model has limited application as it is fitted and tested for a few surfaces only. Recent study on spatially developing flat-plate boundary layers under acceleration and deceleration [3] showed that $U(y)$, when appropriately normalized by U_R, becomes self-similar inside the RSL regardless of pressure gradients, as far as the flow is attached and under high k^+. This is shown in Figure 4.1, where y_R is the roughness sublayer thickness and U_R is the mean velocity at $y = y_R$. This is an important finding as it indicates that a $U(y)$ model developed for equilibrium flows may be directly applicable to a subset of non-equilibrium flows.

Next, the problem of modeling the pressure drag based on the roughness topography can be reduced to the modeling of the topographical dependencies of the equivalent sandgrain height (k_s, as defined in Section 1.2.1) instead. A detailed explanation of the relation between k_s and the logarithmic shift in the mean velocity profile can be found in the Section 1.2.1. This logarithmic shift measures the higher total drag on a rough wall than on a smooth wall, which is mostly pressure drag under sufficiently high k_s^+.

A large body of literature explored the modeling of k_s for fully rough flows based on the roughness topography alone. However, there is no universal formula of k_s for arbitrary roughness geometries. Recent reviews are provided by [69] and [68]. In most of these studies, empirical correlations are developed based on single or a small number of surface features (slope, height fluctuation intensity, skewness, etc.) and fitted to k_s data of a few surfaces [102; 103; 104; 105]. So far, the most advanced existing approach is based on machine learning (ML), e.g. [4] enabled by large k_s-geometry datasets. In the work of [4], 45 datasets with different roughness geometries
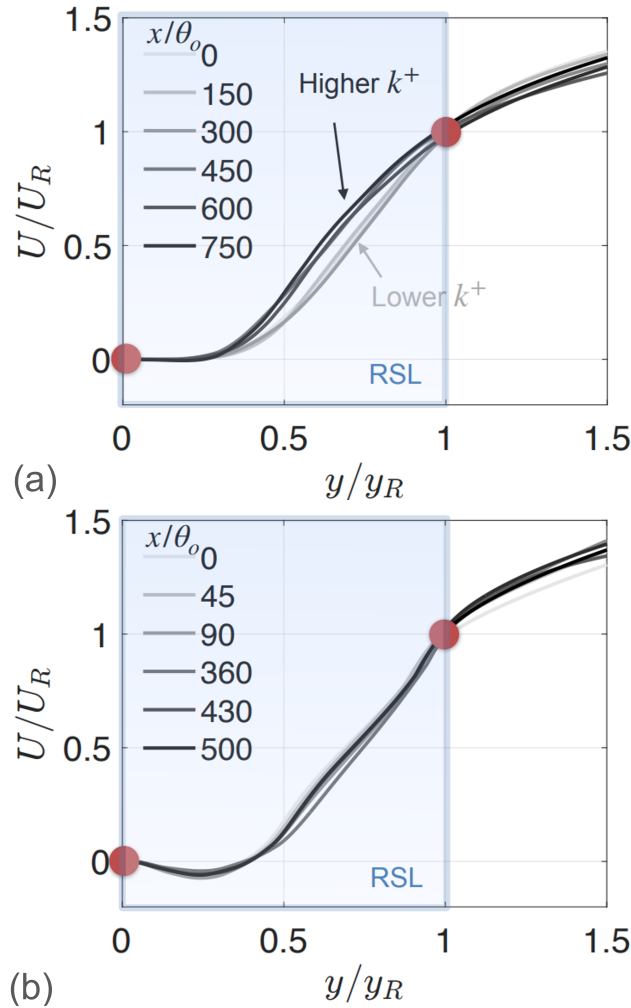
Figure 4.1 Wall-normal profiles of double-averaged velocity inside the RSL of spatially accelerating (a) and suction-blowing (and separating, b) boundary layer flows [3], showing self-similarity of mean velocity regardless of pressure gradients, when normalized by U_R.

are used to train deep neural network (DNN) and Gaussian process regression models that contained more than 10 surface features as inputs. The ML model is shown to give significantly better overall k_s predictions for a large range of surfaces than existing empirical correlations refitted on these surfaces. [106] optimized the training of neural networks with the help of Particle Swarm Optimized Backpropagation technique to predict k_s for 86 surfaces. The data included 2D and 3D roughness type with both regular and irregular arrangements. The roughness types include sandgrain, grit-blasted, truncated cone and multiscale roughness. With the help of roughness height statistics (r.m.s. of height fluctuations, skewness and kurtosis) and effective slope, the optimized algorithm had a prediction accuracy compared to other existing empirical models with a mean absolute percentage error of 28.1%. In addition, feature sensitivity analysis showed r.m.s. of height fluctuations to be the most important feature followed by skewness, effective slope and kurtosis.

The limitation of ML models is, to a large extent, controlled by the generality of the datasets.

[107] showed that the DNN model of [4], as is, yielded large errors in a test with larger datasets containing types of roughnesses not well represented during the ML model development. However, after it is retrained on all data (including new ones), the DNN model outperformed physics-based or empirical k_s correlations. Currently, the largest collection of k_s data on different rough surfaces is the Southampton Roughness Database (`https://roughnessdatabase.org`). As data is important for k_s prediction and can be costly to obtain, insights are needed on limitations of currently available data and on the minimum set of important features affecting k_s (which allows reduction of inputs and thereby data needs for ML training, as well as gaining fundamental knowledge).

This chapter aimed to establish relations between geometrical features of roughness and (i) the double-averaged mean velocity profile $U(y)$ near the wall, as well as (ii) the equivalent sandgrain height k_s, for a wide range of roughnesses. For the k_s prediction, the complete Southampton Roughness Database will be used; the database is not directly applicable to $U(y)$ prediction, however, as $U(y)$ profiles are typically not reported; a subset of that database will be used instead.

Specific objectives include (1) extracting the important roughness features influencing U and k_s, and (2) using the above information to build data-driven regression models to predict $U(y)$ and k_s for a wide range of equilibrium, rough-wall turbulent channel flows, based on existing and new DNS datasets of half-channel flows over rough surfaces. Since the datasets and detailed algorithms used are different for the predictions of $U(y)$ and k_s, the chapter is divided into two parts: Section 4.2 focused on roughness features important for $U(y)$ and its prediction based on these features, while Section 4.3 employed similar approaches (though varying in details) to k_s prediction and analyses. In Section 4.2, Section 4.2.1 surveyed the roughness datasets used for training the regression models, Section 4.2.2 introduced the machine learning methodologies, and Section 4.2.3 identified the important roughness features and summarized the performance of the chosen algorithms. Similar outline followed in Section 4.3 for k_s prediction and analyses. Conclusions are provided in Section 4.4.

4.2 Prediction of double-averaged mean velocity profiles in RSL

For the $U(y)$ prediction, only the RSL region is considered. The RSL is typically defined as the layer in which $\widetilde{u}$ is not negligible compared to U (e.g. $\langle \widetilde{u}^2 \rangle^{1/2}/U > 0.1$, similar to [86]). Under such definition, the sublayer thickness (y_R) is usually slightly higher than the crest height (for example, see [2; 108]. In this work, U in the region $y/k_c = 1$ is examined, as k_c is an approximate estimate of the RSL thickness. Using k_c instead of the exact y_R removes the uncertainty of RSL-thickness identification brought by the threshold value.
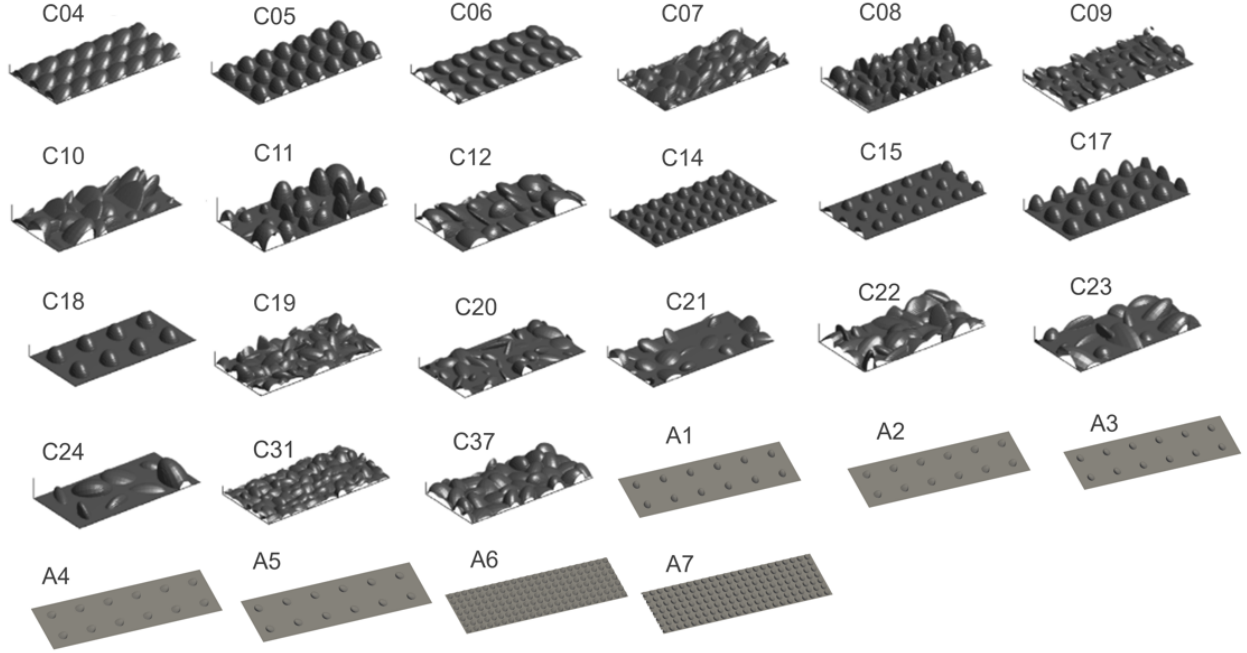
Figure 4.2 Visualization of rough surfaces used in DNS simulations to generate data for $U(y)$ prediction. Cases 'Cxx' are from [4] with a portion (δ and 0.5δ in x and z, respectively) of the domain shown. Cases 'Ax' are newly generated surfaces used for additional simulations herein, with the complete domain shown (3δ and δ in x and z, respectively). Cases A1-A5 are similar to C18, but with varying I_x. Cases A6 and A7 are similar to C05, with varying I_x.

4.2.1 RSL flow datasets

A total of 21 half-channel flows with different wall roughness topographies are used in training the regression techniques for the prediction of $U(y)$. The surfaces are shown in Figure 4.2. They included a subset of the cases simulated by [4], indicated as 'Cxx' (using the same case number as in [4]). Seven additional surfaces (A1 to A7) are synthesized to investigate the effects of element inclination angle and porosity. All surfaces are used in DNS simulations of turbulent half-channel flows with friction Reynolds Number $Re_\tau = 1000$ and domain dimensions $(L_x, L_y, L_z) = (3\delta, \delta, \delta)$, in streamwise, wall normal and spanwise directions, respectively, where δ is the half-channel height. L_x and L_z satisfy the rough-wall minimal-span channel constraints defined by [109] and [110]. All the cases are considered to fall in the fully rough regime based on the values of $k_c^+ \gg 1$, where k_c is the roughness crest height measured from the trough and + denotes normalization by wall units (u_τ and δ_v). The rough surfaces are formed by distributed ellipsoidal sandgrains similar to those of [1]. The distribution, inclinations and size of the ellipsoids are systematically varied. Both regular arrangement (with every element having the same rotation and size) and random arrangements (with random orientations and random size) are included.

Based on the literature regarding the effect of roughness texture on mean momentum (predominantly in terms of the hydrodynamic drag, k_s) , a list of surface features are considered as relevant for affecting the RSL mean velocity profile. Readers are referred to [69] for a comprehensive

summary of dependency of k_s on different roughness features. They included the average peak-to-trough height (k_t), effective slope (ES_x), various moments of local height fluctuations from the mean height (Ra, k_{rms}, s_k, and k_u), roughness-element inclination angle (I_x), porosity (P_o), and spatial correlation length (R_{lx}). They are defined as,

$$ES_x = \frac{1}{A_1} \int_{x,z} \left| \frac{\partial k}{\partial x} \right| dA, \tag{4.3}$$

$$k_{rms} = \left[\frac{1}{A_1} \int_{x,z} (k')^2 dA \right]^{1/2}, \tag{4.4}$$

$$s_k = \frac{1}{A_1 k_{rms}^3} \int_{x,z} (k')^3 dA, \tag{4.5}$$

$$k_u = \frac{1}{A_1 k_{rms}^4} \int_{x,z} (k')^4 dA, \tag{4.6}$$

$$I_x = \tan^{-1} \left\{ \frac{1}{2} s_k \left(\frac{\partial k}{\partial x} \right) \right\}, \tag{4.7}$$

$$P_o = \frac{1}{A_1 k_c} \int_0^{k_c} A_2 dy, \quad \text{and} \tag{4.8}$$

$$R_{lx} = r_x |_{R_x = 0.37}, \tag{4.9}$$

where $k(x, z)$ is the distribution of roughness height (with $k = 0$ at the roughness trough), $A_1(y)$ is the total planar area at a y elevation, $A_2(y)$ is the fluid area, $k' = k - \overline{k}$ is the local height fluctuation from the mean height, $\overline{k} = 1/A_1 \int_{x,z} k dA$, and $R_x(r_x) = \int_{x,z} k'(x, z) k'(x + r_x, z) \, dA / (k_{rms}^2 A_1)$ is the two-point correlation of k' with streamwise separation r_1. The exact threshold of $R_x = 0.37$ is used to remain consistent with the correlation-length calculations used in the Southampton Roughness Database. The features with dimension of length (e.g. k_{rms}, R_{lx} and k_t) are normalized by the first moment of k', $R_a = 1/A_1 \int_{x,z} |k'| dA$. The list of features analyzed are similar to those studied by [4], except for (i) the additional two-point characteristics, R_{lx}, and (ii) considering only the streamwise characteristics for the features that are directional-dependent (i.e. slope, inclination and correlation length) for an arbitrary roughness. The latter change is made to reduce the number of model inputs in light of the limited train-test data available.

To allow the ML scheme to efficiently detect the y-pattern of the velocity profile, the y values (normalized by k_c) at which U values are evaluated, $y/k_c \in [0, 1]$, are also used as input variables along with the surface and flow features mentioned above. The DNS used refined y mesh near
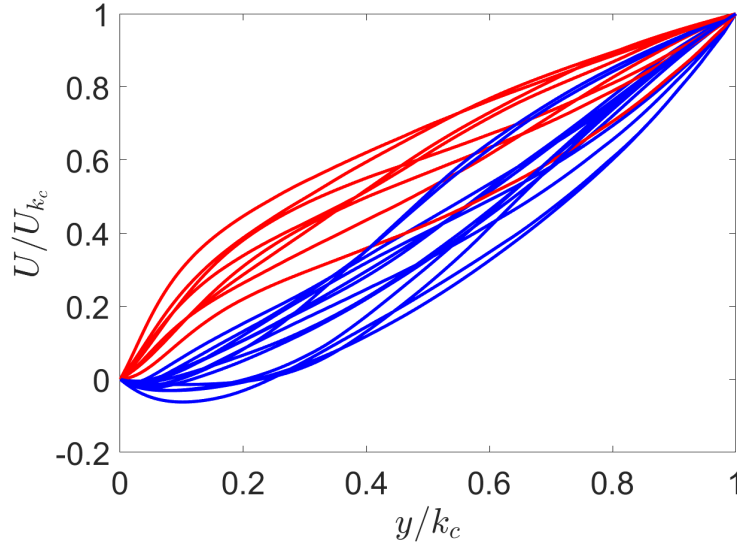
Figure 4.3 Mean velocity profile as a function of wall normal distance (y) in all cases.

$y = 0$. To remove bias of datasets due to more data originating from the finer-resolution region near $y = 0$, the $U(y)$ profiles are interpolated to an equally-spaced y grid in the layer $y/k_c \in [0, 1]$. Figure 4.3 showed the $U(y)$ profiles of all cases in the datasets. The normalization of $U(y)$ leads to all profiles crossing the point $(1, 1)$; on the other hand, at $y = 0$ (i.e. trough elevation) $U = 0$ due to the no-slip condition. The profiles in blue are those that display near-wall flow reversal (i.e. $U < 0$). These cases corresponded to surfaces with relatively dense distribution of rough elements with steep slopes. The rough surfaces in the datasets are surveyed in Figure 4.4 in terms of the values of three features that are generally considered the most crucial for the roughness effects on hydrodynamic drag by the literature (see reviews by [69; 68; 107]: k_{rms}/Ra, S_k and ES_x. The optimum number of clusters for data classification is chosen based on varying the number of clusters from 1 to 7 and selecting the one with the highest silhouette score. Silhouette score is a measure of how well a data point is represented by one cluster in comparison to its nearest cluster. The two classes corresponded well with the two types of flows distinguished in Figure 4.3 based on whether or not mean-flow reversion occurred inside the RSL. Blue circles corresponded to surfaces with mean-flow reversions as shown in Figure 4.3 (as blue curves therein). It is shown here that they are likely characterized by higher ES_x and lower s_k. On the other hand, red circles represented surfaces without mean-flow reversions, corresponding to overall lower ES_x and higher s_k. Also, it is shown that almost all present surfaces are characterized by $s_k > 0$. In other words, very few 'pitty' surface is included. Figure 4.4 highlighted the need for U-profile data on pit-dominated surfaces, as well as those with mild skewness and high r.m.s. (e.g. surfaces with similar peak and dip geometries), and high skewness and low r.m.s (e.g. sparse distribution of peaky elements).

Besides the geometry-based features mentioned above, an additional flow-based feature is also
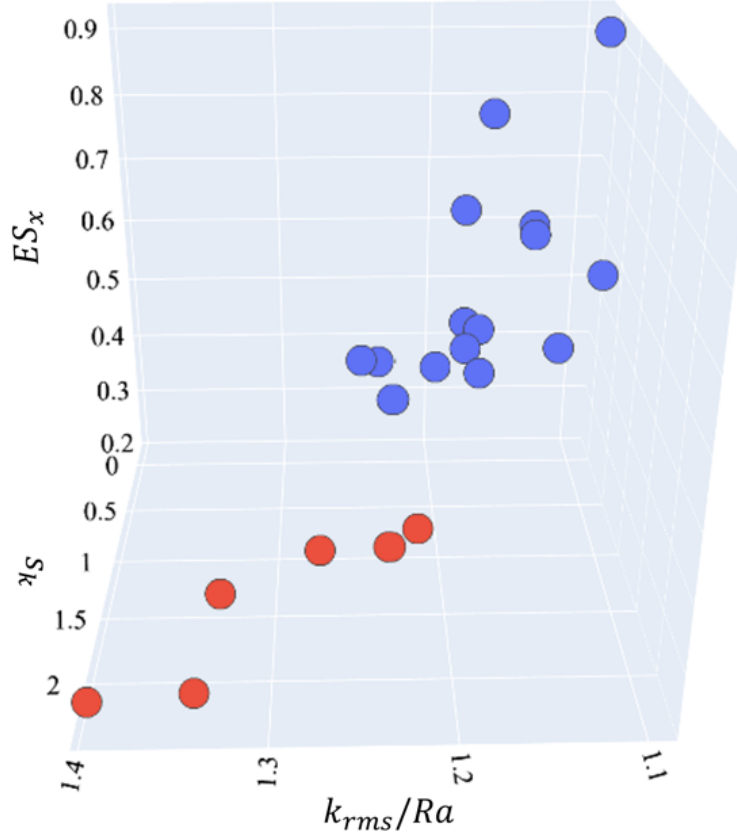
Figure 4.4 Clustering of rough surfaces in (k_{rms}, ES_x, s_k) space.

proposed, to examine whether inclusion of some degree of flow information significantly improves U or k_s prediction. Given the importance of the sheltering phenomenon in roughness drag generation (i.e. the reduction of drag generated by a roughness element due to its location inside the wake of an upstream element; see, for example, [10; 100], the additional feature estimated the significance of the sheltering phenomenon.
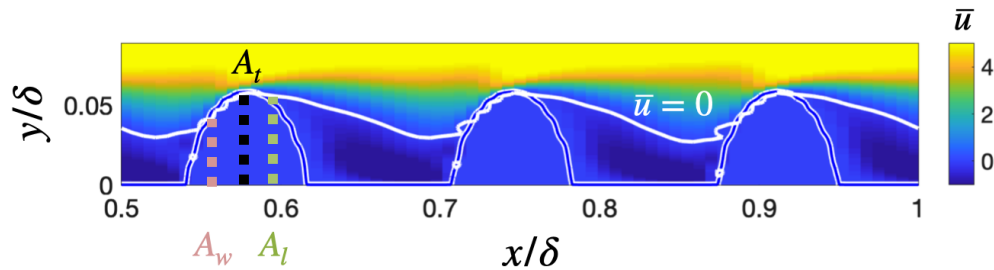
Figure 4.5 Illustration of the quantification of sheltering, defined as regions with $\overline{u} \leq 0$. Contour shows $\overline{u}^+$. Vertical dotted lines indicate locations used to calculate various frontal areas: leeward sheltered frontal area (A_l), windward frontal shelter frontal area (A_w) and total frontal area (A_t). It is termed the sheltering parameter and is defined as

$$\alpha = \frac{\sum A_l - \sum A_w}{\sum A_t},\qquad(4.10)$$

where A_l and A_w are the leeward and windward frontal areas, respectively, of one roughness element and A_t is the total frontal area of the element. These areas are illustrated in Figure 4.5.

Summation is then performed for each area across all roughness elements. The sheltered region of rough surface is defined as that of the surface on which the time-averaged u velocity is zero or negative. In the limiting case of fully sheltered roughness elements, $A_l = A_w$, rending $\alpha = 0$. Therefore, α is a measure of the inverse of sheltering.

4.2.2 ML techniques

The problem solved is a multi-output regression one from R^n to R^m, where n is the number of roughness features plus the number of grid points of y in the RSL and m is the number of discrete $U(y)$ values. For the prediction of $U(y)$, both the non-dimensional input and output data are further scaled by removing the mean and dividing by the standard deviation to uniformize the range of dataset.

As a part of feature selection, the correlation between each set of two out of all feature are calculated and shown in Figure 4.6. The diagonal plots show instead the p.d.f. of the distribution of each individual feature. Significant correlations are found for the pairs of (P_o, s_k), (k_{rms}, k_u) and (s_k, k_u). The strong correlation within the pairs (P_o, s_k) and (k_{rms}, k_u) as highlighted in the black box may be explained by the fact that all surfaces are peaky ones (i.e. surfaces characterized by $s_k > 0$ and formed by predominantly peaky elements with $k' > 0$ instead of pits with $k' < 0$) in the datasets. The strong correlation between s_k and k_u may be attributed to database limitations. Based on the correlations, seven input features from the initial list of ten are considered as independent features describing the differences of present surfaces and are used to train the algorithm: R_{lx}, s_k, ES_x, k_t, k_{rms}, α, and I_x.

The rough surfaces are randomly divided into two sets: 85% data (18 cases) for training and 15% (3 cases) for testing. Gaussian Process Regression (GPR)—a non-parametric, probabilistic prediction machine learning technique—is used. Two other regression techniques, KernelRidge and Decision Tree Regressor are also used for comparison; in comparison, GPR is shown (in Appendix 9) to give the lowest L_∞ error (defined by Equation (4.11)). Also, GPR had the capability of identifying non-polynomial shapes of $U(y)$, which can be important in a multi-output regression problem as the current one. The functioning of the algorithm is dependent on its hyper parameters that include different kernels (quadratic or exponential squared), over-fitting/under-fitting penalty parameter and the number of iterations. These parameters are fine-tuned using the present datasets, by running the algorithm for $N = 1300$ times over different training-testing combinations for the chosen input feature combination. The optimal set of hyper parameters are chosen based the maximum L_∞ error across all flow cases. The optimized GPR algorithm used an exponential squared kernel (i.e. radial basis function) to fit the data. It used 200 iterations to reach convergence while fitting the data. After considering various values for over-fitting/under-fitting penalty parameter in the range $(10^{-3}, 10^3)$, a value of 10^{-2} is found to offer the best performance. Along with GPR, principal component analysis (PCA) (which will be introduced in the next section)

63

is also used to identify the minimum required number of input features needed for $U(y)$ prediction.

The error of the mean velocity prediction using GPR is measured by two norm metrics,
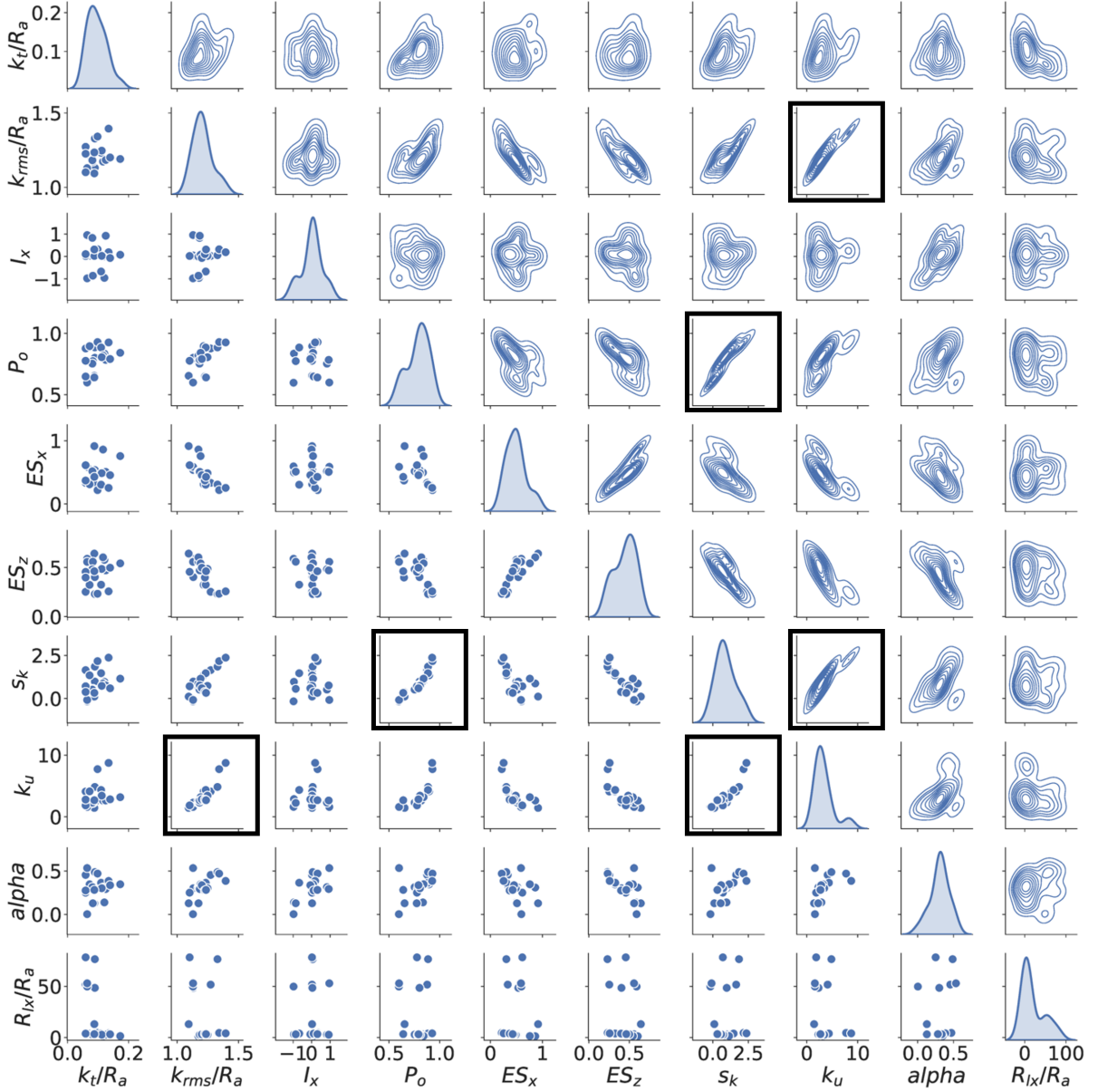
Figure 4.6 Pair plots of roughness features used as inputs.

$$L_\infty = \max_{y^* \in [0,1]} |U^*_{DNS}(y^*) - U^*_{GPR}(y^*)| \quad \text{and} \qquad (4.11)$$

$$L_2 = \int_0^1 [U^*_{DNS}(y^*) - U^*_{GPR}(y^*)]^2 dy^*, \qquad (4.12)$$

where $U^* = U/U_{k_c}$ and $y^* = y/k_c$ are the dimensionless mean velocity and elevation. U_{DNS} and U_{GPR} are, respectively, the velocity extracted from DNS and that predicted by GPR. The respective averages of L_∞ and L_2 (calcualted across both train and test data) for the $N = 1300$

random combinations of train-test split are used as the overall prediction errors. The values of parameters for all surfaces and the code for regression analysis are made publicly available (`https://github.com/Mangavelli94/Prediction-of-wake-velocity-using-ML`).

4.2.3 Results
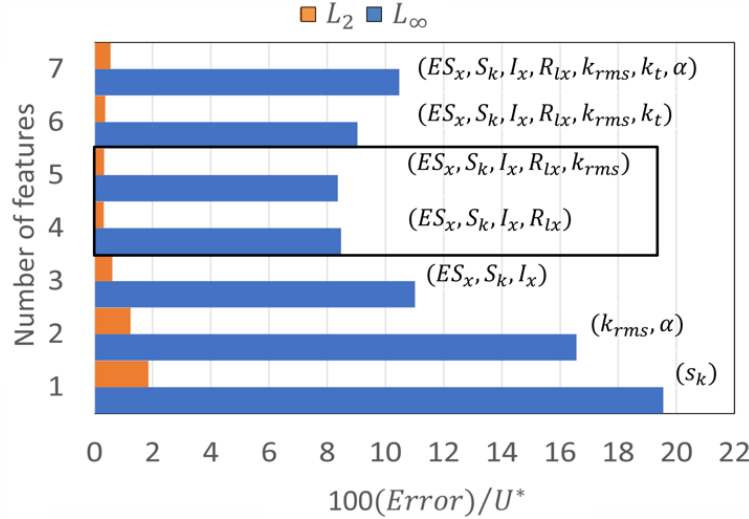
Figure 4.7 Dependence of the prediction error norms (L_2 in orange and L_∞ in blue) on the number of features used as ML inputs. For each number of features, the set of features that yield the minimum error among all combinations of the same number of features is listed.

Initially, the prediction of optimized GPR on training datasets with all input rough features is measured using L_∞. The prediction yielded $L_\infty < 0.1$ for all N random runs, indicating the ability of the chosen algorithm in successfully learning the different patterns in the training datasets. Next, to analyze how the number of roughness features used for GPR training and testing affects the performance of the ML prediction, subsets of the 7 features are tested. The number of features in these subsets are varied from 1 to 7, for each of which all possible combinations of features (out of the total 7) are evaluated for all N random train-test data splits. The minimum error norms and the 'best' feature combinations (associated with the minimum L_∞) as a function of the number of features are shown in Figure 4.7(a). Both L_∞ and L_2 showed a decrease with the number of features increasing from 1 to 5. This is expected as the complex dependency of the mean velocity profile on roughness geometry is not captured by only a very small number of inputs; increasing the number of inputs allowed capturing additional flow physics. Both norms reached a minima when four or five features are used for training and testing. When more than five features are used, the error is shown to slightly increase with the number of features. This is probably due to over-fitting, which is expected with 21 datasets only. The best 4-feature combination is found to be (R_{lx}, S_k, ES_x, I_x), while the best 5-feature one contained an additional k_{rms}. The finding suggested that R_{lx}, k_{rms} (or S_k), ES_x and I_x are the most important features from the total 10 initial ones and that they each contribute independently to the RSL mean velocity, for the present collection of rough surfaces. It

65

had been established that k_{rms}, S_k and ES_x are important rough-wall characteristics that controls the hydrodynamic drag imposed by a rough surface [68]. The present result suggested that these characteristics are also important for RSL mean velocity distribution. In addition, the streamwise inclination and two-point statistics (such as R_{lx}) appeared to be also important. Note that k_{rms} and S_k are expected to affect the flows differently and, as such, introducing an additional k_{rms} should significantly reduce L_∞ and L_2 errors, as opposed to the insignificant changes observed herein. This is due to limitations of the present database: the fact that (i) surfaces with $S_k < 0$ are not included and that (ii) k_{rms} and S_k are strongly correlated by chance.
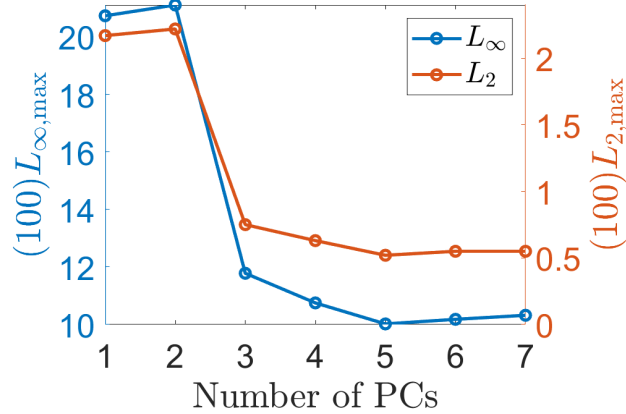
Figure 4.8 Dependence of $U(y)$ prediction error on the number of principal components used as ML inputs.

In order to verify the above analysis on the smallest number of features needed to model $U(y)$, another method, the principal component analysis (PCA), is used to reduce the dimensionality of the feature space to extract the uncorrelated principal components(PCs). These components are obtained using linear mapping of input features that best describes the variation of $U(y)$ in the datasets. Similarly, the number of principal components is allowed to vary from 1 to 7. The GPR algorithm is re-trained for N combinations of train-test split for varying number of principal components as inputs. The maximum value of error norms (calculated as the maximum value of errors for all rough cases) as a function of the number of principal components are shown in Figure 4.8. Both error norms decreased overall from 1 to 5 principal components, reaching a minimum at 5. This is consistent with the findings of the lowest errors observed for the use of 4 or 5 features for training/testing, as shown in Figure 4.7.

Now focus on the GPR algorithm trained with five principal components that yields the minimum L_∞ error. To provide insights on what features are the major contributors to each principal component (i.e. PC1 to PC5), Table 4.1 tabulated the weighted contribution, calculated as a product of squared correlation of the feature and the fraction of variance of its principal component. The correlation between a rough feature and a principal component measures how much a particular roughness feature influenced the principal component. To quantify the importance of each of the

five PCs, the fractions of variance for each of the 5 principal components are listed in the caption of Table 4.1. The fractions of variance in [PC1,PC2,PC3,PC4,PC5] are [0.5,0.22,0.16,0.06,0.025]. They quantified the amount of variance of input features captured by the corresponding principal component, which sums up to 1 for all five principal components. Most of the variance of input features is absorbed in the first three principal components (i.e. PC1 to PC3). Results suggested that R_{lx}, s_k, k_{rms} and ES_x captured the majority of the $U(y)$ variations. This is consistent with the observations made from Figure 4.7. In addition, k_t and I_x are also shown to play a role. Results of both analyses described above (i.e. feature elimination and PCA) demonstrated that each of the features R_{lx}, S_k, ES_x, I_x and k_{rms} independently affected $U(y)$ in the RSL.

	R_{lx}/R_a	k_{rms}/R_a	k_t	S_k	ES_x	I_x	α
PC1	0.00735	0.095	0.125	0.095	0.09	0.008	0.065
PC2	0.0726	0.0242	0.001078	0.0000792	0.000242	0.0638	0.0572
PC3	0.056	0.00912	0.00176	0.0128	0.0128	0.0624	0.00272
PC4	0.00192	0.00216	0.00018	0.0252	0.0276	0.00096	0.00138
PC5	0.00325	0.000975	0.00525	0.00005	0.0019	0.0035	0.00975

Table 4.1 Weighted correlations between individual features with individual principal components for the $U(y)$ datasets.
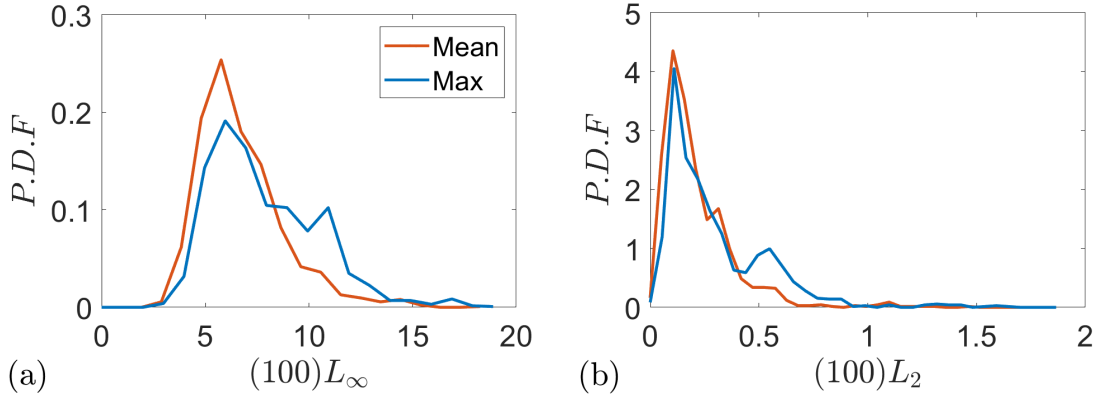
(a) $(100)L_\infty$ (b) $(100)L_2$

Figure 4.9 PDF of $U(y)$ prediction errors in all cases of the GPR algorithm developed with the optimal set of inputs: $(R_{lx}/R_a, s_k, ES_x, I_x, k_{rms})$: (a) $(100)L_\infty$, (b) $(100)L_2$.

The analyses above (Figures 4.7 and 4.8) discussed the error norms that are averaged across both train and test datasets and across all $N = 1300$ random train/test data splits (also called 'runs'). Below we discuss the distribution of the errors for test datasets only, across the 1300 runs, when the 5 most important input features identified above (R_{lx}, s_k, ES_x, k_{rms} and I_x) are used to train the model. Here, the exclusive use of test data gives an estimation of the model's performance for predicting $U(y)$ in flows with roughness not included in the training datasets. The probability density function (PDF) of the error norms (in terms of their maximum and mean values among the test datasets) are displayed in Figure 4.9 for L_∞ (a) and L_2 (b). Among the 1300 runs, only 26% of the runs yielded a maximum L_∞ higher than 0.1, with the peak of PDF at around $L_\infty = 0.06$.

Similarly, 22% of the runs gave maximum L_2 higher than 0.005, with the PDF peak at around 0.001. This result confirms that a majority of the test cases are well predicted.

Next, the sensitivity of the GPR prediction to the dataset size is tested by adding six more cases (by varying the P_o and I_x to include new surfaces that are sparser or varying within a wider range of inclination angles). These additional surfaces are shown in Figure 4.2 starting with 'A'. Among 2600 runs (i.e. 17% of all possibilities of picking 4 test cases from the total of 27 cases with different surfaces; not all possibilities are tested due to due to long computational time), the probabilities of the maximum of L_∞ being higher than 0.1 and the maximum of L_2 being higher than 0.005 increased to 31% and 23% from 26%, 22% respectively. The slight increase of the occurrences of high-error cases indicates that the current algorithm is only weakly sensitive to the addition of new datasets generated using the identified important features.
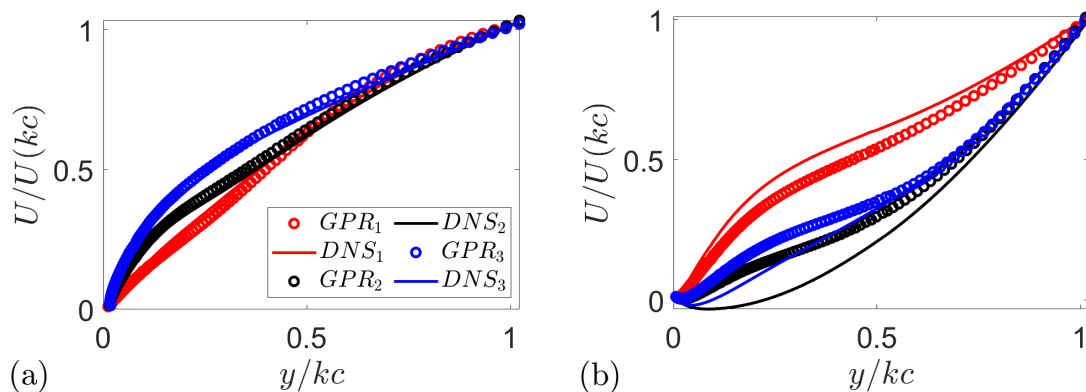
Figure 4.10 Examples of predicted mean velocity profiles compared to their DNS-extracted profiles: (a) low-error cases with L_∞ = 0.033 (red), 0.027 (blue) and 0.028 (black); (b) relatively high-error cases with L_∞ = 0.075 (red), 0.14 (blue) and 0.09 (black).

Figure 4.10 shows the performance of $U(y)$ predictions at different L_∞ errors. The DNS-extracted $U^*(y^*)$ and the GPR predictions of the three test cases are compared in the figure, for three representative runs that yielded different maximum L_∞ values of 0.03, 0.08 and 0.14, respectively. Figure 4.10(a) shows three cases where the predictions of GPR are very close to the DNS-extracted profiles, while Figure 4.10(b) shows another three cases where the errors are relatively larger. The errors appear to be significantly attributed to the velocity profile in the lower portion of the roughness sublayer, especially if a mean-flow reversal (i.e. $U(y) < 0$) layer is present. To analyze whether some surfaces consistently lead to higher prediction errors than other surfaces among the 1300 runs, the number of times a particular case having $L_\infty > 0.1$ (while being a test case) is shown in Figure 4.11(a). Note that all cases are used as test cases for similar total occurrences for this analysis, as almost all possible combinations of test cases are analyzed. It shows that C04, C06 and C14 have a higher frequency of $L_\infty > 0.1$. The corresponding DNS-extracted $U(y)$ profiles of these three cases are highlighted in Figure 4.11(b) in black and compared to other profiles.

(a)

(b)
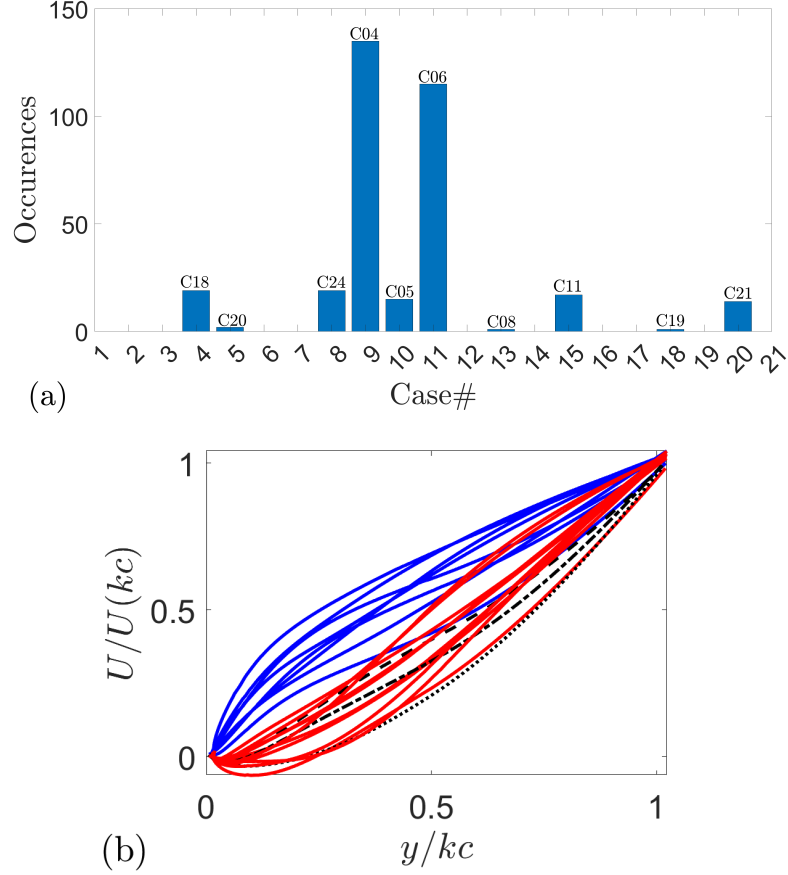
Figure 4.11 (a) Occurrences of each individual flow cases with $L_\infty > 0.1$, when the set of optimal input features are used. (b) DNS-extracted mean velocity distributions of all cases, with the three cases with the highest large-error occurrences in (a) highlighted in black: C04 (---), C06 (···), C14 (–·–).

Cases C04 and C06 are the only two surfaces with uniform streamwise inclination for all grains in the datasets, while in Case C14 rough elements are rather sparsely located. The under-representation of inclined and sparse surfaces in the database may explain the consistently higher prediction errors for these three surfaces.

4.2.4 Explanation of the importance of inclination and porosity

The spatial distribution of rough peaks is shown by the literature for equilibrium flows [40] and non-equilibrium flows in Chapter 3 to impact the formation and growth of $\widetilde{u}$. Hence, P_o (or R_{lx}) that characterizes the overall distance between rough peaks is studied in this section. Additionally, the observed importance of I_x on $U(y)$ is not well understood and is also studied here. Figure 4.12 and Figure 4.13 examine the iso-surfaces of $\bar{u}(x, y, z)$ with small magnitudes, which shows the wake region with a small positive value ($\bar{u}^+ = 1.0$) and the separated-flow region with a negative value ($\bar{u}^+ = -0.05$) around each roughness element, in a few cases with different element inclinations and distribution densities (i.e. porosity). Comparison between Figure 4.12(a) and Figure 4.12(b)

69
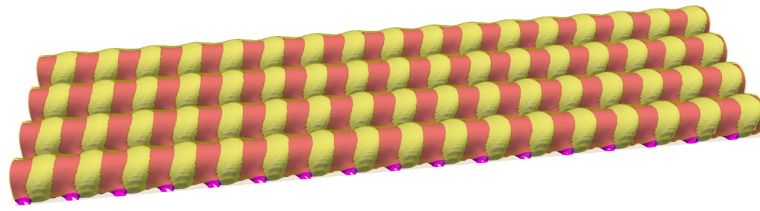
(a)
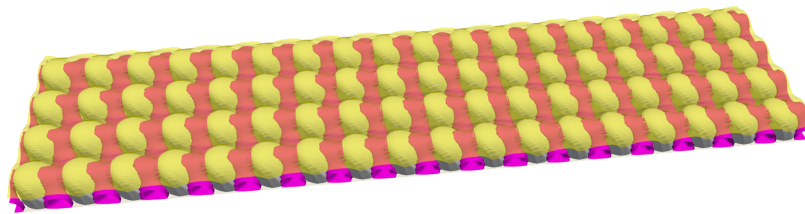
(b)

Figure 4.12 Effect of roughness-element inclination on $\overline{u}$ distribution in the RSL: (a) Case C04 with elements inclined toward the direction of flow and (b) Case C06 with elements inclined in the opposite direction of flow. Iso-surfaces of $\overline{u}^+ = 1.0$ and $\overline{u}^+ = -0.05$ are shown in yellow and magenta, respectively, overlaid on visualized rough surfaces.

shows that an inclination of roughness elements toward the direction of flow (C04) led to smaller re-circulation regions in the wake of roughness (shown by the magenta surfaces) compared to case C06 where the inclination is toward the opposite direction of the flow. The larger re-circulation regions in case C06 are because, in this case, the $\overline{u} = -0.05$ iso-surfaces grow wider (in z) downstream of each roughness element, as compared to case C04. Therefore, the RSL $U(y)$ profile takes lower values in C06 than in C04, which is shown in Figure 4.14(a) where case C06 shows a stronger re-circulation region closer to the wall. In addition, channeling regions of locally high-speed flows between streamwise ridges of roughness elements are seen here for all cases, similar to other studies in the literature for roughness of various geometries, such as irregular surfaces with Gaussian height distribution [111], sand grain roughness [112], pyramid roughness [113], among others. Around 70% of surfaces in the database are randomly distributed and/or rotated. Figure 4.13 compares two cases with the same roughness elements but different values of distribution density. The higher porosity in C18 (Figure 4.13(b)) leads to more significant fraction of the in-plane area

(a)

(b)
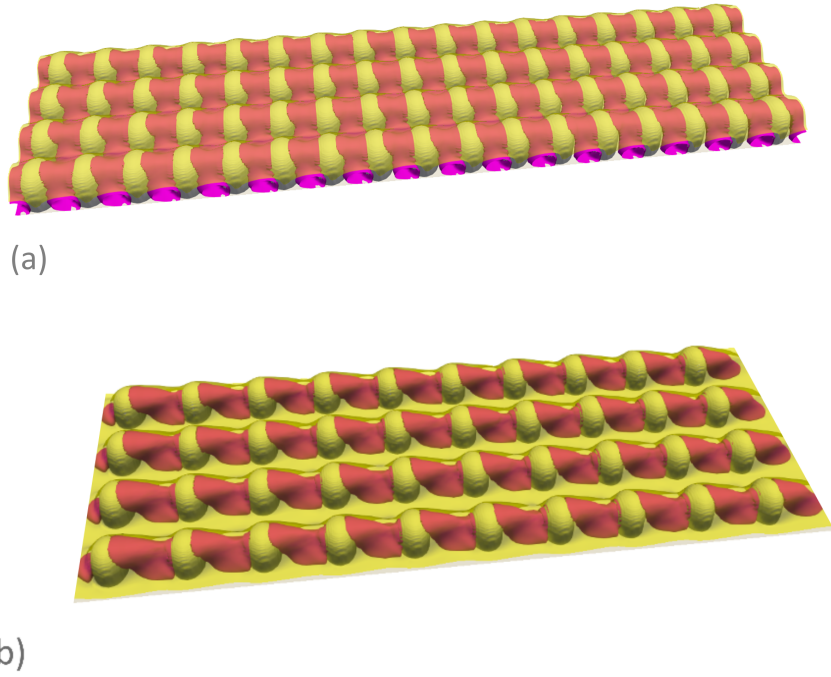
Figure 4.13 Effect of roughness porosity on $\overline{u}$: (a) C05 case with densely distributed elements, and (b) C18 case with the same k_c as C05 but a sparser distribution. Iso-surfaces of $\overline{u}^+ = 1.0$ and $\overline{u}^+ = -0.05$ are shown in yellow and magenta, respectively, overlaid on visualized rough surfaces.

(a)

(b)
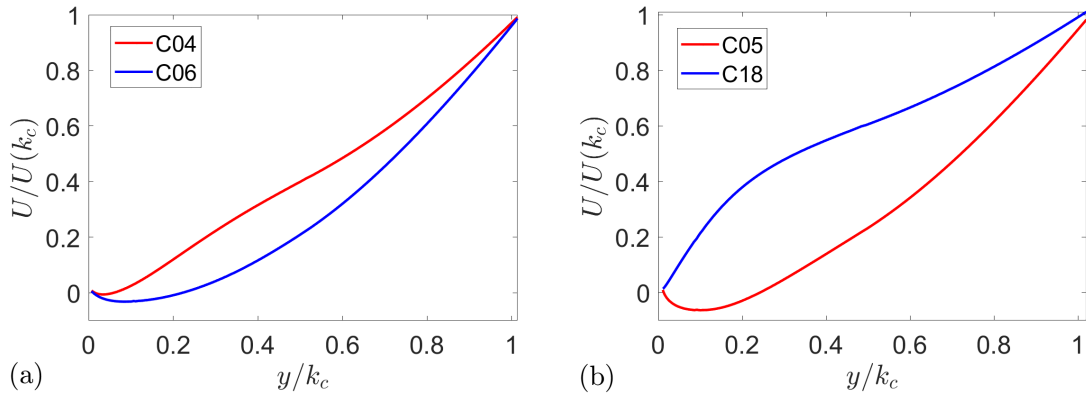
Figure 4.14 Mean velocity profiles for (a) the two cases with different I_x (shown in Figure 4.12) and (b) the two cases with different porosity values (shown in Figure 4.13).

covered by high-speed channeling flows. In addition, the larger streamwise separation between roughness elements reduces the fraction of the surface covered by the separation regions. In contrast, a more densely distributed roughness shown in Figure 4.13(a) displays separation regions growing along x and filling the streamwise distance between neighboring elements. These effects of porosity on $U(y)$ is shown in Figure 4.14(b), where near-wall reversal of the plane-average velocity occurs in C05 but not in C18.

71

For surfaces mentioned above, both I_x and parameters measuring the roughness peak distribution (such as R_{lx} and Po) are shown to affect the these separation regions. This suggests the importance of I_x and Po (as well as sparsity) on the prediction of $U(y)$. Systematic analyses with controlled surface variations is needed to understand the interplay between the effects of these features.

4.3 Prediction of k_s

4.3.1 Datasets and ML technique

For the prediction of k_s/R_a, additional data from the Southampton Roughness Database [114; 67; 103; 115; 116] are added to the database used by [4]. A total of 90 rough surfaces are included. A large portion of the additional datasets represent cuboid or bar roughness with constant or varying heights which are not well represented in the datasets of [4]. The uncertainty in the estimation of friction velocity is at most 1% for the present DNS cases. The uncertainty (for available data) in experimental datasets is $\leq 3\%$ [102]. A rough estimation based on $\Delta U^+ = (1/\kappa) \log_{10}(k_s^+) + C$ (where C is a constant), assuming that ΔU^+ is measured at a location with $U^+ = 10$, shows that a 1% higher u_τ estimate is equivalent to a 10% higher k_s. Though the calculation of k_s is not linearly correlated to friction velocity, the uncertainty is hypothesized to be in similar range.

The roughness features used as inputs consist of single-point height statistics: I_x, P_o, s_k, k_u, k_{rms}/Ra, ES_x and ES_z, where

$$ES_z = \frac{1}{A_1} \int_{x,z} \left| \frac{\partial k}{\partial z} \right| dA, \tag{4.13}$$

$$I_z = \tan^{-1} \left\{ \frac{1}{2} s_k \left(\frac{\partial k}{\partial z} \right) \right\}, \tag{4.14}$$

and two-point correlations of height fluctuations: R_{lx} defined in Section 4.2.1 and R_{lz} defined as

$$R_{lz} = r_z |_{R_z=0.37}, \tag{4.15}$$

where $R_z(r_z) = \int_{x,z} k'(x,z) k'(x, z + r_z) \, dA / (k_{rms}^2 A_1)$. The two coherence lengths are both normalized by Ra. The magnitude of I_z (i.e. $|I_z|$) is added, as the effect of spanwise inclination of roughness elements on the total drag is expected to be identical for inclinations toward positive or negative z directions. In addition, products of primary features and their second-degree polynomials: $(ES_x)(ES_z)$, $(ES_x)(s_k)$, $(ES_z)(s_k)$, $(ES_x)(k_u)$, $(s_k)(k_u)$, $(ES_z)(k_u)$, ES_x^2, ES_z^2 and s_k^2) are also included based on the importance of their primary features in characterizing rough surfaces in the dataset. Inclusion of these quantities are shown to improve the current algorithm. However, inclusion of R_{lx}^2, R_{lz}^2,etc. did not improve the algorithm significantly and they are not included. In total, 19 features are used.

Figure 4.15 shows the pair plots between all roughness features and the actual k_s/R_a values measured from physical or numerical experiments. Specifically, the diagonal plots show the
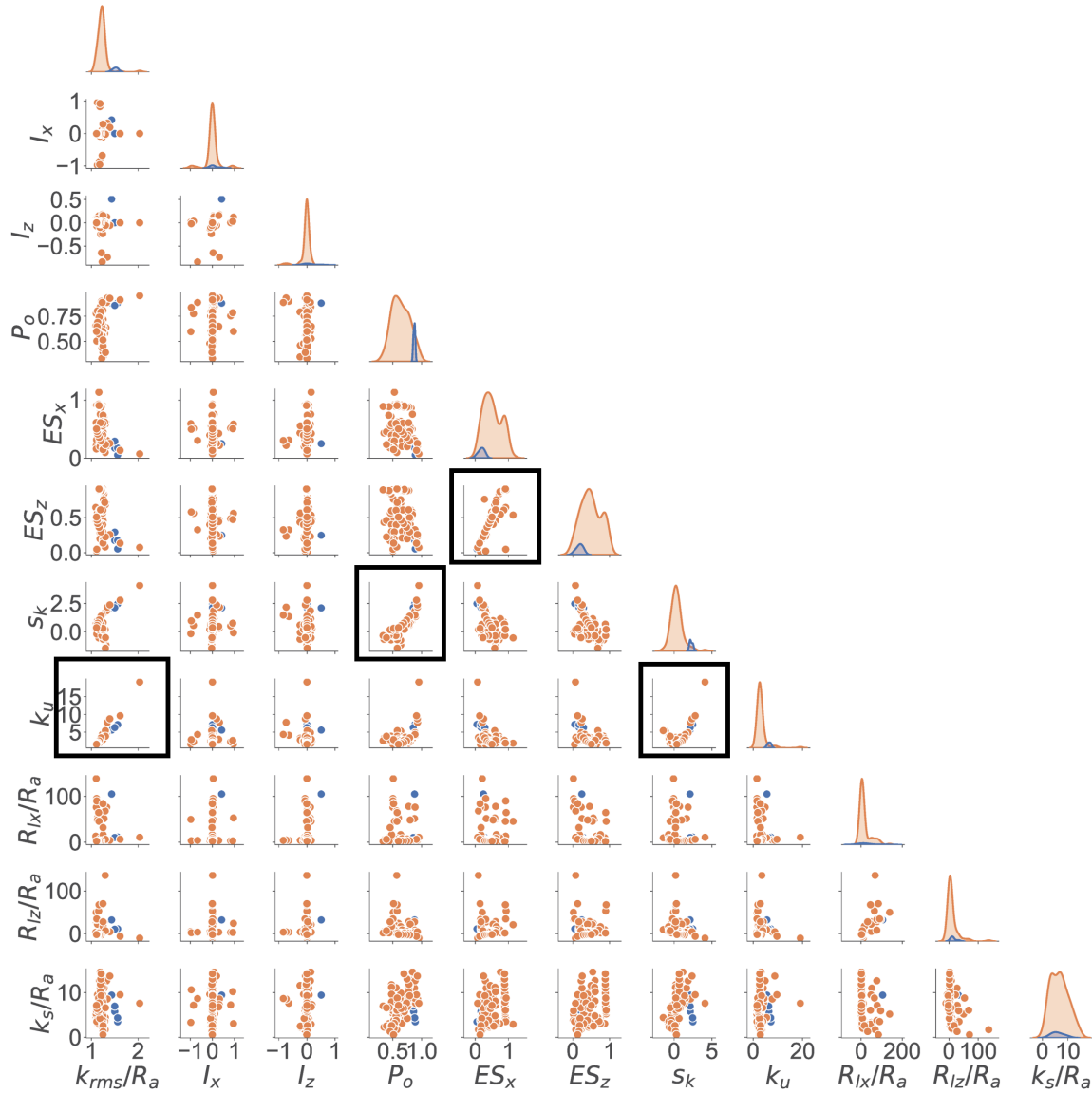
Figure 4.15 Pair plots of roughness features and k_s/Ra. Orange and blue circles denote roughness types: bar roughness and non-bar roughness, respectively.

probability density function of each single feature or k_s; the off-diagonal plots show correlations between each pair of two different roughness features or k_s. In general, the bar-type roughness tends to give higher skewness and k_{rms}/R_a values due to the ideal nature of the roughness-element geometry. Almost all features are shown to vary for a rather wide range, suggesting that the database is overall comprehensive for the features shown. Wider ranges may be explored in the future for I_z and k_u. The PDF of s_k shows that most surfaces are positively skewed (i.e. peaky), while a significant number of pitty surfaces (with $s_k < 0$) are also included.

It is shown in Figure 4.15 that some correlation exists within the feature pairs (P_o, S_k), (ES_x, ES_z), (k_{rms}, k_u), and (s_k, k_u), as highlighted in black boxes. The correlation between P_o and

S_k is possibly because most of the surfaces are peaky; in this case, a higher skewness indicates a sparser surface marked with higher porosity. The correlation between ES_x and ES_z is due to most surfaces being isotropic in x and z (i.e. with mostly mild inclinations in x and z, as shown by the PDFs of I_x and I_z). The correlation between k_{rms} and k_u is because both features characterize the intensity of k' fluctuations. Lastly, the correlation between s_k and k_u is an interesting observation, possibly due to more dominant peaks in sparser surfaces (i.e. higher s_k) contributed to significant k_u. In addition, the last row of plots show that k_s/R_a does not correlate perfectly with any single roughness feature.

The re-scaling of the input and output data is done similarly to that described in Section 4.2.2. The Neural Network (NN) used by [4] is re-calibrated and retrained for the two-fold larger database and the new set of inputs include both single- and two-point statistics. The hyperparameters of the algorithm that are optimized based on the datasets include the number of neural layers and their branches. Three layers are chosen with the numbers of branches in each of the three layer varying from 14 to 21, 10 to 16, and 4 to 10, respectively. The over/under-fitting penalty parameter is set to 0.2. The algorithm is trained over 250 iterations with a random selection of training and testing data and the one with the lowest L_∞ error (across both training and testing sets) is chosen. A larger number of iterations for algorithm optimization is tested. The maximum error (with the error defined as $|k_s - k_{s,pred}|/k_{s,pred}$, where k_s and $k_{s,pred}$ are the actual and predicted equivalent sandgrain height values, respectively) changes by less than around 1% only, when the number of iterations increases to 500 (while the optimization time increases by 3.5 times, from 7 hours to 24 hours). In every iteration, the training-to-testing-data ratio is maintained at 70/30. Additionally, PCA is used to perform dimensional reduction to identify the minimum number of independent input features needed for k_s prediction.

4.3.2 Results

Figure 4.16 shows the performances of the NN trained with the set of single-point surface statistical inputs used by [4] (denoted as NN_1) over the current dataset. Figure 4.16(a) compares the predicted and actual k_s values for all cases, with the percentage differences shown in Figure 4.16 (b). The maximum of percentage difference for all cases is around 75% and the mean error percentage is around 11%. In comparison, the maximum and mean values of such error reported by [4] for a database of 45 rough cases is around 30% and 10%, respectively. The lower errors reported there is attributed to the limitation of the datasets used therein, with a lack of regular cuboid or bar-type roughness, which are significantly different from multiscale surfaces or those consisting of non-bar elements, associated with the higher skewness, k_{rms} and porosity values shown in Figure 4.15. In comparison, Figure 4.17 shows the performance of the re-configured NN (denoted as NN_2) with hyperparemeters in the same range as the previous algorithm, but with the two additional two-point surface statistical inputs (R_{lx} and R_{lz}).

Initially, similar to the analysis of identifying whether the algorithm is trainable on the rough surface datasets in Section 4.2.3, the L'_∞ error for training datasets with all 19 rough features yielded

(a)   (b)
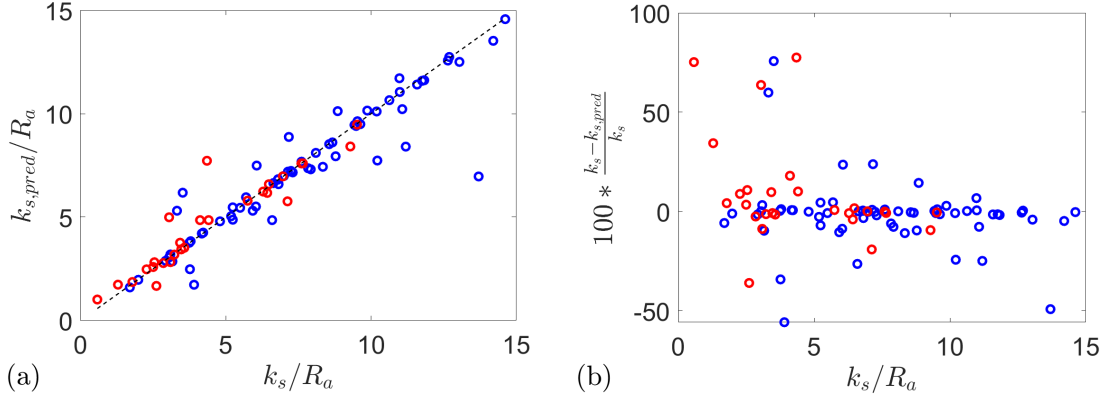
Figure 4.16 Performance of the re-calibrated NN with the same inputs as [4]. (a) Predicted values ($k_{s,pred}$) compared to actual values (k_s) of the equivalent sandgrain height. (b) Percentage error. Blue and red symbols denote numerical and experimental measurements, respectively.

(a)   (b)
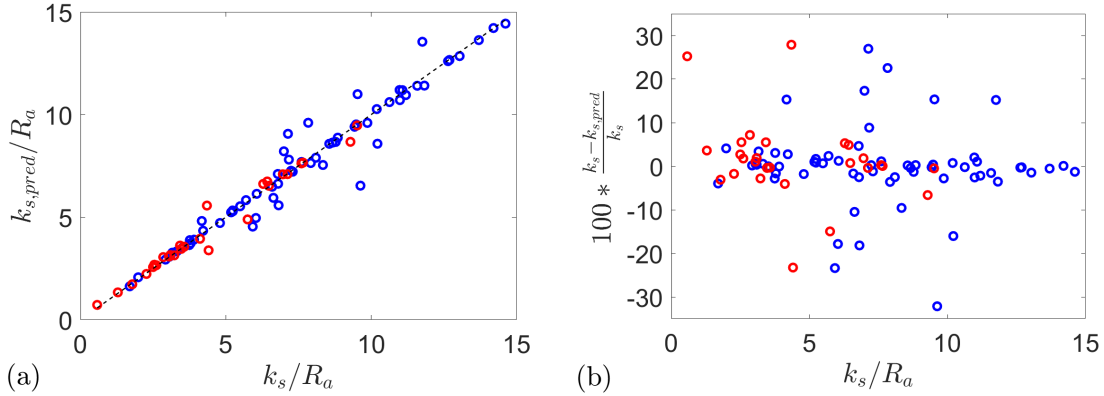
Figure 4.17 Performance of the new NN with additional inputs of correlation lengths. (a) Predicted values ($k_{s,pred}$) compared to actual values (k_s) of the equivalent sandgrain height. (b) Percentage error. Blue and red symbols denote numerical and experimental measurements, respectively.

values up to 0.1. Then, the maximum and mean percentage errors are calculated as shown in Figure 4.17(b). They are around 33% and 5%, respectively, reducing by almost a half from predictions based on single-point inputs alone. The comparison highlights the importance of including surface features that contain structural information of the surface topography besides single-point height characteristics.

To compare the error distribution of the predictions of the NN_1 and NN_2 networks, the error probability density functions (PDF) are shown in Figure 4.18. The higher probabilities of lower errors for NN_2 (with the PDF skewed to the left) confirms the overall better performance of the model with the additional R_{lx} and R_{lz} inputs. To compare the two PDFs quantitatively, the L_1 and L_2 norms are calculated for each algorithms as

$$L_1 = \frac{1}{n} \sum_{i=1}^{n} \frac{|k_{s,pred,i} - k_{s,i}|}{k_{s,i}}, \tag{4.16}$$

75

$$L_2 = \frac{1}{n}\sqrt{\sum_{i=1}^{n}\frac{|k_{s,pred,i} - k_{s,i}|^2}{k_{s,i}^2}}, \qquad (4.17)$$

where n is the total number of rough-wall flow cases. (L_1, L_2) for NN_1 are $(10.7, 2.2)$ and for NN_2 are $(5.3, 1.0)$, again confirming the better prediction of NN_2.
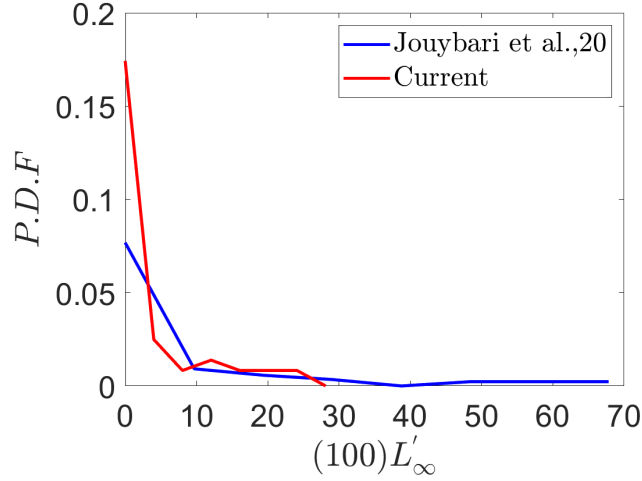
Figure 4.18 Comparison of error distributions of the NN predictions with (red) and without (blue) correlation lengths as inputs. $L'_\infty \equiv |k_{s,pred} - k_s|/k_s$.

The importance of correlation lengths is due to their direct representation of the overall distance between the roughness peaks in x and z. In Section 4.2, the formation of separation region around a roughness element and its downstream growth in the element wake is shown to be dependent on the distribution of roughness peaks. Since the total pressure drag is determined by the flow separation zones, parameters describing the roughness peak distribution such as R_{lx} and R_{lz} are expected to be important in determining k_s. Inclusion of additional flow cases in the datasets including varying peak element density for truncated cones [95], cuboidal roughness [115; 116], among others further necessitates the need to include the correlation lengths as inputs.

Next, the minimum set of important topographical features for accurate predictions of k_s is studied using principal component analysis (PCA). Instead using the 19 surface features as ML inputs, principal components of the roughness-feature space are identified and used directly as ML inputs to train the NN network. The number of principal components are systematically varied from 1 to 19 (i.e. up to the number of total surface features). Figure 4.19(a) shows the variation of

the L_∞-norm of the k_s prediction error, defined as

$$L_\infty = \max \frac{|k_{s,pred,i} - k_{s,i}|}{k_{s,i}}, \tag{4.18}$$

as a function of the number of principal components used. The error decreases with increasing number of principal components, as expected due to the inclusions or progressively richer
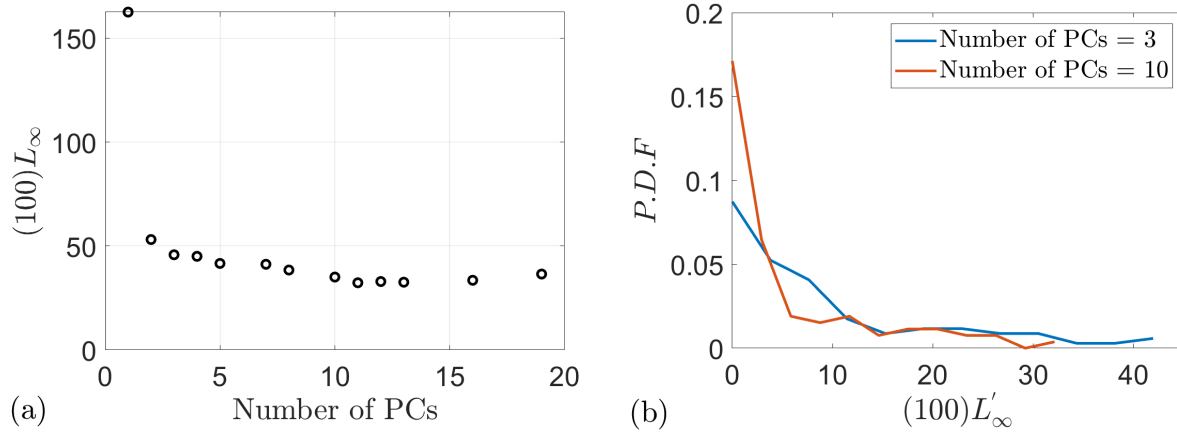
Figure 4.19 (a) Variation of k_s error norm with the number of principal components used as NN inputs. (b) Comparison between the PDFs of k_s percentage errors predicted with 3 and 10 principal components.

topographical information, roughly plateauing at 3 principal components and reaching a minima at around 10 components. This suggests that, while a large number of topographical features (such as k_{rms}, S_k, etc.) are relevant to drag generation, there are roughly three 'orthogonal features' only. Further increasing the number of principal components only slightly improve prediction. Figure 4.19(b) compares the PDFs of k_s percentage errors for the predictions with 3 and 10 principal components. PDF distributions of both errors are skewed to the left for both the PCA cases, indicating that most flow cases are successfully predicted with low errors. Predictions with 10 PCs give low errors in more cases.

To analyze the mapping between individual topographical features and the principal components, Tables 4.2 and 4.3 show the weighted contributions of the features to each of the identified principal components, for the PCA analyses with 3 and 10 PCs, respectively. The weighted contributions are calculated as the product between the fraction of variance (defined in Section 4.2.3) of the principal components and the squared correlation (also defined in Section 4.2.3). The fractional variance of the principal components for the analysis with 3 PCs are $(0.39, 0.23, 0.12)$, respectively, covering 74% of variance of the topographical features, whereas the first six principal components for the analysis with 10 PCs are $(0.39, 0.23, 0.12, 0.08, 0.05, 0.05)$, respectively, covering 92% of variance of the features. This explains the better overall prediction when using 10 principal components than that using 3.

In addition, Table 4.2 and Table 4.3 show that, regardless of the number of PCs, the significant contributors to the PCs (based on a weighted contribution ≥ 0.01) include: (i) k_{rms}/R_a, s_k and k_u, (ii) porosity, (iii) slope in both x and z, and (iv) correlation lengths. Secondary features (products and polynomial functions of slope and s_k, not shown) also contribute significantly. The fact that the NN predictions with 3 PCs are almost as good as those with more PCs (Figure 4.19(a)) suggests that these features form the minimal set of important features for k_s prediction. As the number of PCs increases from 3 to 10, the inclination angles in x and z are also added to the contributing features. As the PCA illustrates the dominant variations of the rough surfaces in the Southampton Roughness Database, the present findings suggest that almost all features studied herein are well varied in the database, although not much so for the element inclination angles. This is indeed the case as most studies on k_s-correlation development (e.g. [103; 19; 67; 69]) focused on surfaces with systematically varying single-point roughness height moments, slopes and element distribution density, while systematically varied inclination angles were less examined (the present work and [4]. Yet, the inclination angles are shown to affect the flow development in the roughness wake in Section 4.2.4 and consequently the total drag. This explains the better prediction results of the NN network with 10 PCs (where I_x and I_z contribute to the PCs) than that with 3 PCs (where I_x and I_z do not contribute to PCs). Future numerical/experimental datasets with wider range of inclinations are needed to improve the database for k_s prediction development.

Surface	k_{rms}/R_a	I_x	I_z	P_o	ES_x	ES_z	s_k	K_u	R_{lx}/R_a	R_{lz}/R_a
PC-1	0.02	0.0003	0.003	0.02	0.04	0.04	0.03	0.02	0.002	0.0003
PC-2	0.015	0.00002	0.00046	0.016	0.0058	0.01	0.015	0.019	0.011	0.011
PC-3	0.014	9.6E-08	0.0024	0.0085	0.0021	0.00036	0.0038	0.011	0.00038	1.2E-05

Table 4.2 Weighted correlations between individual features with individual principal components for the k_s datasets, when three principal components are used.

Surface	k_{rms}/R_a	I_x	I_z	P_o	ES_x	ES_z	s_k	K_u	R_{lx}/R_a	R_{lz}/R_a
PC-1	0.02	0.0003	0.0033	0.016	0.039	0.039	0.031	0.0208	0.0019	0.00031
PC-2	0.0155	0.00002	0.00046	0.016	0.0058	0.01	0.015	0.019	0.011	0.012
PC-3	0.014	9.6E-08	0.0024	0.0085	0.0021	0.00036	0.0038	0.011	0.00038	1.2E-05
PC- 4	0.00049	0.0028	0.00012	8.96E-07	0.0021	2.42E-05	0.00048	0.00070	0.032	0.030
PC-5	0.00034	0.0042	0.036	0.00048	4.2E-05	3.6E-05	0.00021	2.5E-05	0.00023	3.7E-06
PC-6	1.2E-05	0.044	0.0037	6.9E-05	4.1E-07	2.2E-06	3.7E-09	4.6E-05	0.0011	0.00086

Table 4.3 Weighted correlations between individual features with individual principal components for the k_s datasets, when ten principal components are used.

4.4 Conclusions and discussions

This chapter examines the dependence of factors important for roughness modeling and the dispersive-stress transport (i.e. roughness-sublayer mean velocity profile $U(y)$ and equivalent sandgrain height k_s) on the roughness features, as well as ML modeling based on a state-of-the-art rough-wall-flow datasets. First, for the prediction of $U(y)$, 21 DNS datasets are used. A data clustering analysis of the different rough surfaces shows two groups, which corresponds to two distinctive types of $U(y)$ with or without near-wall flow reversal. Values of the surface features demonstrate strong correlations among the pairs: (P_o, s_k), (k_{rms}, k_u) and (s_k, k_u), attributed to dataset limitation including the lack of pitty roughness. The observed correlations were used to guide the reduction of feature inputs, to avoid over-fitting due to the limited datasets. One of the novelties of the current work is the feature sensitivity analysis based on systematic elimination of surface features by GPR and dimensionality reduction based on PCA. They identified 5 independent surface features: $(R_{lx}, s_k, ES_x, k_{rms}, I_x)$ as the most important ones. Detailed studies of time-averaged velocity $(U(x, y, z))$ patterns shows that the formation and growth of local separation zones in the wake of roughness elements depend on the inclination and distribution of roughness elements, explaining the observed importance of (I_x) and R_{lx}. The current analyses also identified surfaces C04 and C06 (differing in I_x) and C14 (sparsely distributed roughness) to be difficult to model. Therefore, additional data with systematically varying inclination angles and sparsity (while keeping other features constant) are needed to make to improve $U(y)$ predictions.

Next, for the prediction of k_s, around 90 rough-wall-flow datasets from the Southampton Roughness Database are used. Compared to past ML k_s-prediction work [4], the present work uses significantly larger datasets with (with bar-type roughness and pitty surfaces that were not well represented) In addition, additional two-point statistical features of roughness (i.e. spatial correlation lengths) are used as inputs, due to their capability in describing roughness sparsity which affects downstream growth of local separation zones. Results show that the inclusion of correlation lengths significantly improves NN algorithm predictions, reducing L_1 and L_2 errors by a half compared to NN without these inputs. A PCA analysis shows that most of the surface variation is contained in three principal components only. Comparisons between PCA analyses with different numbers of principal components, as well as NN predictions based on these principal components as inputs, show that the minimal set of important features for k_s predictions is $(k_{rms}, s_k, k_u, ES_x, ES_x, R_{lx}, R_{lz})$ and some of their combinations, which are overall consistent with those observed for $U(y)$ prediction due to the common physics (e.g. local separation zones) affects both double-averaged velocity and pressure drag. It is also shown that the inclination angles affect k_s but are not widely varied in the database. Systematic variations of individual features (e.g. varying inclination angles of roughness elements of a given shape, varying correlation lengths while keeping porosity constant if possible) are needed to further understand effects of the features

on k_s and to improve the database.

The work in this chapter demonstrates the capability of ML algorithms in predicting quantities that are important for non-equilibrium turbulence modeling. For example, the predicted $U(y)$ profile can be used to model roughness-sublayer velocity in the framework of [75]. Results also demonstrate the limitation of current available datasets and offer insights for future efforts in systematic generation of rough-wall datasets. Future work based on the PCA analyses may explore explicit expressions of the few orthogonal features based on the large number of surface features used by the community, for effective feature reduction that will benefit roughness modeling. Additionally, the standard deviation feature of GPR that measures the regions of high prediction errors will be explored for $U(y)$ prediction. This will offer further insights into the sensitivity of $U(y)$ on various features and what surface features are not sufficiently explored in the present roughness database.

CHAPTER 5
CONCLUSIONS AND FUTURE WORK

5.1 Overall conclusions

Understanding the effect of roughness topography on the turbulent flow responses to temporal and/or spatial acceleration or deceleration is important in many engineering and environmental applications, such as flows in turbomachinery, around vehicles or sea-going vessels, around city canopies, etc. Rough surfaces seen in real-world applications are usually irregular and multiscale, adding an additional complexity in studying their effects. The current work aims to understand the effects of wall roughness in non-equilibrium transient wall turbulence and their modeling for a wide range of different roughness topographies.

In Chapter 2, direct numerical simulations of the half-channel turbulent flows are carried out to study the effects of roughness texture on turbulence response to a sudden increase of bulk velocity. The motivation is to quantitatively and qualitatively study the combined effect of the mean flow acceleration and roughness texture, especially for the multiscale roughness. Two rough surfaces: a homogeneous, densely distributed sandgrain roughness and a multiscale turbine-blade roughness are simulated, along with a smooth-wall baseline case. The rough-wall flows develop from a transitionally rough regime to a fully rough one during the transient. Immersed boundary (IB) method is used to impose non-slip/penetration boundary conditions at the rough surface, which is well-resolved by the grid. As seen in the existing literature of temporally and spatially accelerated flows, turbulence over a smooth wall undergoes a quasi-laminarization process, which is not observed in the presence of roughness. For rough cases, the rapid increase of hydrodynamic drag and roughness sublayer (RSL) turbulence intensities in their early stages is attributed to high turbulence production due to form-induced velocity gradients. This leads to a rapid increase in turbulence kinetic energy (TKE) and isotropization of the RSL Reynolds stresses. Moreover, the roughness geometry is shown to affect the recovery rate of the RSL turbulence. A slower recovery of TKE redistribution (due to a slower amplification of pressure fluctuations) is seen on the multiscale roughness, compared to the homogeneous one. This is associated with sparsely distributed roughness peaks, producing new turbulence which takes time to spread and cover the whole domain. For both rough cases, the outer-layer Reynolds stresses showed a slower recovery. Additionally, the friction velocity (u_τ) is shown to scale on the mean velocity at the upper edge of the roughness sublayer (U_R). Also, the wall-normal profiles of dispersive stresses (when normalized using U_R) are shown to be self-similar for both rough cases.

Motivated by the importance of form-induced fields in the dynamics of rough-wall turbulent flows, Chapter 3 examines the effects of form-induced quantities on turbulence structure and the TKE-redistribution process, important in determining non-equilibrium turbulence response, using the same DNS half-channel flow data of Chapter 2. Analyses of two-point turbulent velocity

correlations show a rapid decrease in streamwise coherence and increases of inclination angles in response to the acceleration in both rough cases, while the opposite is observed on the smooth wall. In the rough cases, coherent motions of turbulence undergo a reduction in their streamwise length (as shown by velocity spectra) in the homogeneous roughness case, whereas they are initially elongated in x on the multiscale rough wall, a phenomenon similar to the smooth-wall flow. This is further verified by the higher local time-scale ratio (i.e. 'frozen' turbulence, with respect to the time scale of the form-induced velocity shear) and their occurrence in large areas between sparsely distributed peaks of the multiscale roughness. Furthermore, in addition to the form-induced production of TKE as often discussed in the literature, a new pathway in which the form-induced velocity affects the Reynolds stress transport through augmenting pressure fluctuations is identified. Analyses of the pressure Poisson equation shows that both sources due to $\widetilde{u_i}$ gradients and u_i' gradients are important, with the spatial distribution of the latter correlated with the former, probably due to the production of TKE as a result of the form-induced fields. Results highlight the importance of $\widetilde{u_i}$ in the dynamics of non-equilibrium turbulent flows.

To better understand how the transport of form-induced stresses depend on the roughness texture, Chapter 4 analyzes and models the surface dependence of two quantities that are important for the production of form-induced stresses (i.e. WKE): $U(y)$ in RSL and a parameter measuring the pressure drag, k_s. A second objective is to model $U(y)$ for different roughness topography to be used for non-equilibrium turbulence modeling. For the prediction of $U(y)$, 21 DNS datasets of rough surfaces made up with ellipsoid elements in the fully rough regime are used. Data classification analysis using clustering technique based on rough features shows two patterns in $U(y)$, with and without mean-flow reversal. Feature sensitivity analysis by manual elimination of inputs of the GPR algorithm identifies 5 features as the minimum set of important features in the prediction of $U(y)$: R_{lx}, I_x, ES_s, k_{rms} and s_k. The optimized GPR algorithm with these features as inputs gives overall very good predictions of velocity profiles in all cases, with a maximum error of 8%. Upon analyzing the iso-contours of 3D time-averaged velocity patterns, the formation and growth of local mean separation zones downstream of roughness elements is shown to be dependent on roughness rotation (I_x) and its peak distribution (measured by R_{lx} or porosity), explaining the dependence of U on these features.

For the analysis and prediction of k_s, the datasets of [4] is expanded to include cuboidal-type roughness, multiscale roughness and a significant amount of pitty surfaces ($s_k < 0$). Additional two-point features (i.e. correlation lengths) are added to the list of inputs for the first time, to incorporate spatial information such as separation of local peaks. This addition significantly improves the NN algorithm by reducing both L_1 and L_2 errors by a half. A sweep of NN predictions with different numbers of principal components (in the surface feature space) as inputs shows the minimal set of important features for k_s prediction to be ($k_{rms}, s_k, k_u, ES_x, ES_x, R_{lx}, R_{lz}$) and some

of their combinations. These features are overall consistent with those important ones for $U(y)$ prediction, due to similar flow physics involved (i.e. local separation zones) in determining mean velocity and drag. I_x, I_z are only shown to be important with addition of new principal components (that contained remaining 20% of the variance of input features), indicating insufficient variation of inclination angles in the available datasets. Addition of more datasets with varying inclination angles while keeping the shape constant and repeating this for different shape of rough surfaces will aid better prediction of k_s.

To summarize, this work studied the response of mean and turbulent fields in non-equilibrium wall turbulence dependent on roughness texture. The major contributors to the different mean-momentum and Reynolds stress transports on rough surfaces as compared to a smooth wall are identified. Qualitative estimation and quantitative prediction of their dependencies on roughness texture are carried out, which also identifies a set of surface features that are important for dynamics in accelerated turbulent flows. The identification of the important features will aid future generation of additional rough surfaces to complement the datasets for better understanding and modeling rough-wall flows. In addition, the mean-flow scaling relations and self-similarity discovered for non-equilibrium accelerated turbulence provide significant insights for physics-based modeling of rough-wall non-equilibrium flows in general.

5.2   Future work

First, identification of the important features in Chapter 4 will (1) aid in future generation of regression models that can be integrated into computationally inexpensive RANS solvers, and (2) offer guidance in generation of new rough surfaces to deepen the understanding of the roughness texture effects and increase the accuracy and universality of roughness models. As these new datasets are added, data classification techniques that can identify patterns in the datasets, similar to clustering in $U(y)$, can then be explored. This will survey the datasets for comprehensiveness and may provide better strategies in splitting datasets into training-testing sets in ML algorithm development. In addition, a more systematic analysis is required to understand individual effects of the surface features, by synthesizing rough surfaces with variation of one feature at a time. This is important for white box modeling using the identified important rough features and understanding their influence on the wake field. A larger representation of multiscale roughness is also needed (e.g. power-law roughness) to expand the roughness database. Future work based on the PCA analyses may explore explicit expressions of the few orthogonal features based on the large number of surface features used by the community, for effective feature reduction that will benefit roughness modeling.

Next, future work is needed to expand the roughness models to non-equilibrium flows in general, including accelerating or decelerating flows (in time or in space) over rough surfaces. As an extension of this work, a recent study [3] compared non-equilibrium flat-plate turbulent

boundary layers under spatial acceleration and deceleration (including both attached and separating flows). The mean-flow (u_τ, U, $\langle \widetilde{u_i}\widetilde{u_j} \rangle$, etc.) scaling on U_R was found to apply also in the spatially varying flows therein. For example, $U(x,y)/U_R(x)$ inside the RSL was found self-similar in the attached flow with sufficiently high k^+, regardless of acceleration. This means that the current $U(y)$ model developed for canonical channel flows may be applicable also to non-equilibrium flows. However, a knowledge gap exists for non-equilibrium rough-wall flows under low k^+ (e.g. in APG/decelerating flows close to separation point), where the above mean-flow quantities may depend also on k^+ and pressure gradient/acceleration. Future investigations are needed on understanding the dependencies of the mean flow and turbulence in flows with low k^+ values. To do so, simulation/experimental measurements are needed in temporally/spatially-varying wall-bounded turbulent flows under systematically varying roughness geometry, k^+ and acceleration. This is a future endeavor needed to fully understand effects of roughness in non-equilibrium wall turbulence.

BIBLIOGRAPHY

[1]   A. Scotti, "Direct numerical simulation of turbulent channel flows with boundary roughened with virtual sandpaper," *Phys. Fluids*, vol. 18, pp. 031701–1—4, 2006.

[2]   S. C. Mangavelli, J. Yuan, and G. J. Brereton, "Effects of surface roughness topography in transient channel flows," *J. Turbul.*, vol. 22, pp. 434–460, 2021.

[3]   J. Yuan, S. C. Mangavelli, and G. Brereton, "Roughness sublayer in non-equilibrium wall-bounded turbulence," *Bulletin of the American Physical Society*, 2023.

[4]   M. Aghaei Jouybari, J. Yuan, G. J. Brereton, and M. S. Murillo, "Data-driven prediction of the equivalent sand-grain height in rough-wall turbulent flows," *J. Fluid Mech.*, vol. 912, pp. A8–1—23, 2021.

[5]   R. Grenier, P. Oryschuk, and P. Léveillé, "Components surface deterioration and effect on performance," Tech. Rep. T032700 0323A, CEATI, 2007.

[6]   E. A. Murphy, J. M. Barros, M. P. Schultz, K. A. Flack, C. N. Steppe, and M. A. Reidenbach, "Roughness effects of diatomaceous slime fouling on turbulent boundary layer hydrodynamics," *Biofouling*, vol. 34, no. 9, pp. 976–988, 2018.

[7]   J. Nikuradse, "Strömungsgesetze in rauhen rohren," *VDI-Forsch.*, 1933.

[8]   C. F. Colebrook, "Turbulent flow in pipes with particular reference to the transition region between smooth- and rough-pipe laws," *J. Inst. Civ. Eng.*, vol. 11, pp. 133–156, 1939.

[9]   M. R. Raupach, R. A. Antonia, and S. Rajagopalan, "Rough-wall boundary layers," *Appl. Mech. Rev.*, vol. 44, pp. 1–25, 1991.

[10]   J. Jiménez, "Turbulent flows over rough walls," *Annu. Rev. Fluid Mech.*, vol. 36, pp. 173–196, 2004.

[11]   M. R. Raupach and A. S. Thom, "Turbulence in and above plant canopies," *Annu. Rev. Fluid Mech.*, vol. 13, pp. 97–129, 1981.

[12]   J. Finnigan, "Turbulence in plant canopies," *Annu. Rev. Fluid Mech.*, vol. 32, pp. 519–571, 2000.

[13]   H. S. Shafi and R. A. Antonia, "Anisotropy of the reynolds stresses in a turbulent boundary layer on a rough wall," *Exp. Fluids*, vol. 18, pp. 213–215, 1995.

[14]   P.-Å. Krogstad, R. A. Antonia, and L. W. B. Browne, "Comparison between rough-and smooth-wall turbulent boundary layers," *J. Fluid Mech.*, vol. 245, pp. 599–617, 1992.

[15]   M. P. Schultz and K. A. Flack, "The rough-wall turbulent boundary layer from the hydraulically smooth to the fully rough regime," *J. Fluid Mech.*, vol. 580, pp. 381–405, 2007.

[16]   G. J. Kunkel, J. J. Allen, and A. J. Smits, "Further support for Townsend's Reynolds number similarity hypothesis in high Reynolds number rough-wall pipe flow," *Phys. Fluids*, vol. 19, pp. 055109–1—6, 2007.

[17]   K. A. Flack, M. P. Schultz, and J. S. Connelly, "Examination of a critical roughness height for outer layer similarity," *Phys. Fluids*, vol. 19, p. 095104, 2007.

[18]   R. J. Volino, M. P. Schultz, and K. A. Flack, "Turbulence structure in rough-and smooth-wall

boundary layers," *J. Fluid Mech.*, vol. 592, pp. 263–293, 2007.

[19] K. A. Flack and M. P. Schultz, "Review of hydraulic roughness scales in the fully rough regime," *J. Fluids Eng.*, vol. 132, pp. 041203–1—10, 2010.

[20] P.-Å. Krogstad and R. A. Antonia, "Surface roughness effects in turbulent boundary layers," *Exp. Fluids*, vol. 27, no. 5, pp. 450–460, 1999.

[21] R. J. Volino, M. P. Schultz, and K. A. Flack, "Turbulence structure in a boundary layer with two-dimensional roughness," *J. Fluid Mech.*, vol. 635, pp. 75–101, 2009.

[22] P. Passalacqua, F. Porté-Agel, E. Foufoula-Georgiou, and C. Paola, "Application of dynamic subgrid-scale concepts from large-eddy simulation to modeling landscape evolution," *Water Resour. Res.*, vol. 42, pp. W06D11–1–11, 2006.

[23] R. Mejia-Alvarez and K. T. Christensen, "Wall-parallel stereo particle-image velocimetry measurements in the roughness sublayer of turbulent flow overlying highly irregular roughness," *Phys. Fluids*, vol. 25, pp. 115109–1–24, 2013.

[24] C. Vanderwel and B. Ganapathisubramani, "Effects of spanwise spacing on large-scale secondary flows in rough-wall turbulent boundary layers," *J. Fluid Mech.*, vol. 774, p. R2, 2015.

[25] J. Yang and W. Anderson, "Numerical study of turbulent channel flow over surfaces with variable spanwise heterogeneities: Topographically-driven secondary flows affect outer-layer similarity of turbulent length scales.," *Flow, Turb. Combust.*, vol. 100, pp. 1–17, 2018.

[26] H. Bai, Kevin, N. Hutchins, and J. Monty, "Turbulence modifications in a turbulent boundary layer over a rough wall with spanwise-alternating roughness strips," *Physics of Fluids*, vol. 30, no. 5, p. 055105, 2018.

[27] R. Mittal and G. Iaccarino, "Immersed boundary methods," *Annu. Rev. Fluid Mech.*, vol. 37, no. 1, pp. 239–261, 2005.

[28] S. Leonardi, P. Orlandi, R. J. Smalley, L. Djenidi, and R. A. Antonia, "Direct numerical simulations of turbulent channel flow with transverse square bars on one wall," *J. Fluid Mech.*, vol. 491, pp. 229–238, 2003.

[29] P. Orlandi and S. Leonardi, "Direct numerical simulation of three-dimensional turbulent rough channels: parameterization and flow physics," *J. Fluid Mech.*, vol. 606, pp. 399–415, 2008.

[30] M. Kanda, "Large-eddy simulations on the effects of surface geometry fo building arrays on turbulent organized structures," *Bound.-Lay. Meteorol.*, vol. 118, pp. 151–168, 2006.

[31] S.-H. Lee and H. J. Sung, "Direct numerical simulation of the turbulent boundary layer over a rod-roughened wall," *J. Fluid Mech.*, vol. 584, pp. 125–146, 2007.

[32] J. H. Lee, H. J. Sung, and P.-Å. Krogstad, "Direct numerical simulation of the turbulent boundary layer over a cube-roughened wall," *J. Fluid Mech.*, vol. 669, pp. 397–431, 2011.

[33] I. P. Castro, A. Segalini, and P. H. Alfredsson, "Outer-layer turbulence intensities in smooth- and rough-wall boundary layers," *Journal of Fluid Mechanics*, vol. 727, pp. 119–131, 2013.

[34] M. Aghaei Jouybari, G. J. Brereton, and J. Yuan, "Turbulence structures over realistic and

synthetic wall roughness in open channel flow at $Re_\tau = 1000$," *J. Turbul.*, vol. 20, pp. 723–749, 2019.

[35] R. Ma, K. Alamé, and K. Mahesh, "Direct numerical simulation of turbulent channel flow over random rough surfaces," *Journal of Fluid Mechanics*, vol. 908, 2021.

[36] M. R. Raupach and R. H. Shaw, "Averaging procedures for flow within vegetation canopies," *Bound.-Lay. Meteorol.*, vol. 22, pp. 79–90, 1982.

[37] E. Mignot, E. Bartheleemy, and D. Hurther, "Double-averaging analysis and local flow characterization of near-bed turbulence in gravel-bed channel flows," *J. Fluid Mech.*, vol. 618, pp. 279–303, 2009.

[38] J. Yuan and U. Piomelli, "Roughness effects on the Reynolds stress budgets in near-wall turbulence," *J. Fluid Mech.*, vol. 760, p. R1, 2014.

[39] O. Coceal, T. G. Thomas, I. P. Castro, and S. E. Belcher, "Mean flow and turbulence statistics over groups of urban-like cubical obstacles," *Bound.-Lay. Meteorol.*, vol. 121, pp. 491–519, 2006.

[40] J. Yuan and M. Aghaei-Jouybari, "Topographical effects of roughness on turbulence statistics in roughness sublayer," *Phys. Rev. Fluids*, vol. 3, p. 114603, 2018.

[41] E. Mignot, E. Barthélemy, and D. Hurther, "Turbulent kinetic energy budget in a gravel-bed channel flow," *Acta Geophysica*, vol. 56, pp. 601–613, 2008.

[42] R. Narasimha and K. R. Sreenivasan, "Relaminarization in highly accelerated turbulent boundary layers," *J. Fluid Mech.*, vol. 61, pp. 417–447, 1973.

[43] C. Bourassa and F. O. Thomas, "An experimental investigation of a highly accelerated turbulent boundary layer," *J. Fluid Mech.*, vol. 634, pp. 359–404, 2009.

[44] U. Piomelli and J. Yuan, "Numerical simulations of spatially developing, accelerating boundary layers," *Phys. Fluids*, vol. 25, pp. 101304–1—21, 2013.

[45] W. Schoppa and F. Hussain, "Coherent structure generation in near-wall turbulence," *J. Fluid Mech.*, vol. 453, pp. 57–108, 2002.

[46] J. Jiménez and A. Pinelli, "The autonomous cycle of near-wall turbulence," *J. Fluid Mech.*, vol. 389, pp. 335–359, 1999.

[47] R. J. Volino, "Non-equilibrium development in turbulent boundary layers with changing pressure gradients," *J. Fluid Mech.*, vol. 897, pp. A2–1–48, 2020.

[48] Y. Na and P. Moin, "The structure of wall-pressure fluctuations in turbulent boundary layers with adverse pressure gradient and separation," *J. Fluid Mech.*, vol. 377, pp. 347–373, 1998.

[49] M. Skote and D. S. Henningson, "Direct numerical simulation of a separated turbulent boundary layer," *J. Fluid Mech.*, vol. 471, pp. 107–136, 2002.

[50] W. Cheng, D. I. Pullin, and R. Samtaney, "Large-eddy simulation of separation and reattachment of a flat plate turbulent boundary layer," *J. Fluid Mech.*, vol. 785, pp. 78–108, 2015.

[51] W. Wu and U. Piomelli, "Effects of surface roughness on a separating turbulent boundary

layer," *J. Fluid Mech.*, vol. 841, pp. 552–580, 2018.

[52] R. Vinuesa, R. Örlü, and P. Schlatter, "Characterisation of backflow events over a wing section," *J. Turbul.*, vol. 18, no. 2, pp. 170–185, 2017.

[53] Z. Harun, J. P. Monty, R. Mathis, and I. Marusic, "Pressure gradient effects on the large-scale structure of turbulent boundary layers," *J. Fluid Mech.*, vol. 715, pp. 477–498, 2013.

[54] C. S. Vila, R. Vinuesa, S. Discetti, A. Ianiro, P. Schlatter, and R. Örlü, "Separating adverse-pressure-gradient and reynolds-number effects in turbulent boundary layers," *Physical Review Fluids*, vol. 5, no. 6, p. 064609, 2020.

[55] S. He and J. D. Jackson, "A study of turbulence under conditions of transient flow in a pipe," *J. Fluid Mech.*, vol. 408, pp. 1–38, 2000.

[56] S. He and M. Seddighi, "Turbulence in transient channel flow," *J. Fluid Mech.*, vol. 715, pp. 60–102, 2013.

[57] R. B. Cal, B. Brzek, T. Johansson, and L. Castillo, "The rough favourable pressure gradient turbulent boundary layer," *J. Fluid Mech.*, vol. 641, pp. 129–155, 2009.

[58] J. Yuan and U. Piomelli, "Numerical simulation of a spatially developing accelerating boundary layer over roughness," *J. Fluid Mech.*, vol. 780, pp. 192–214, 2015.

[59] S. He and M. Seddighi, "Transition of transient channel flow after a change in Reynolds number," *J. Fluid Mech.*, vol. 764, pp. 395–427, 2015.

[60] C. D. Ghodke and S. V. Apte, "DNS study of particle-bed–turbulence interactions in an oscillatory wall-bounded flow," *J. Fluid Mech.*, vol. 792, pp. 232–251, 2016.

[61] C. D. Ghodke and S. V. Apte, "A numerical investigation to study roughness effects in oscillatory flows," in *Proceedings of the ASME 2017 Fluids Engineering Division Summer Meeting*, 2017.

[62] L. Djenidi, M. Kamruzzaman, and L. Dostal, "Effects of wall suction on a 2d rough wall turbulent boundary layer," *Experiments in Fluids*, vol. 60, no. 3, pp. 1–11, 2019.

[63] E. Napoli, V. Armenio, and M. De Marchis, "The effect of the slope of irregularly distributed roughness elements on turbulent wall-bounded flows," *J. Fluid Mech.*, vol. 613, pp. 385–394, 2008.

[64] J. Yuan and U. Piomelli, "Estimation and prediction of the roughness function on realistic surfaces," *J. Turbul.*, vol. 15, pp. 350–365, 2014.

[65] L. Chan, M. MacDonald, D. Chung, N. Hutchins, and A. Ooi, "A systematic investigation of roughness height and wavelength in turbulent pipe flow in the transitionally rough regime," *J. Fluid Mech.*, vol. 771, pp. 743–777, 2015.

[66] J. A. Van Rij, B. Belnap, and P. Ligrani, "Analysis and experiments on three-dimensional, irregular surface roughness," *J. Fluids Eng.*, vol. 124, no. 3, pp. 671–677, 2002.

[67] M. Thakkar, A. Busse, and N. D. Sandham, "Surface correlations of hydrodynamic drag for transitionally rough engineering surfaces," *J. Turbul.*, vol. 18, pp. 138–169, 2017.

[68] D. Chung, N. Hutchins, M. P. Schultz, and K. A. Flack, "Predicting the drag of rough

surfaces," *Annu. Rev. Fluid Mech.*, vol. 53, pp. 439–471, 2021.

[69] K. A. Flack and D. Chung, "Important parameters for a predictive model of k_s for zero pressure gradient flows," in *AIAA SCITECH 2022 Forum*, 2022.

[70] R. D. Sanhueza, I. Akkerman, and J. W. Peeters, "Machine learning for the prediction of the local skin friction factors and nusselt numbers in turbulent flows past rough surfaces," *International Journal of Heat and Fluid Flow*, vol. 103, p. 109204, 2023.

[71] P. A. Durbin, "Reflections on roughness modelling in turbulent flow," *Journal of Turbulence*, vol. 24, no. 1-2, pp. 3–13, 2023.

[72] A. Busse and N. D. Sandham, "Parametric forcing approach to rough-wall turbulent channel flow," *Journal of Fluid Mechanics*, vol. 712, pp. 169–202, 2012.

[73] S. Wu, K. T. Christensen, and C. Pantano, "Modelling smooth-and transitionally rough-wall turbulent channel flow by leveraging inner–outer interactions and principal component analysis," *Journal of Fluid Mechanics*, vol. 863, pp. 407–453, 2019.

[74] X. Yang and C. Meneveau, "Large eddy simulations and parameterisation of roughness element orientation and flow direction effects in rough wall boundary layers," *Journal of Turbulence*, vol. 17, no. 11, pp. 1072–1085, 2016.

[75] G. J. Brereton, M. Aghaei Jouybari, and J. Yuan, "Towards modeling of turbulent flow over surfaces of arbitrary roughness," *Phys. Fluids*, vol. 33, pp. 065121–1—13, 2021.

[76] J. Yuan, J. Nicolle, U. Piomelli, and A.-M. Giroux, "Modelling roughness and acceleration effects with application to the flow in a hydraulic turbine," *IOP Conf. Series: Earth and Environmental Science*, vol. 22, p. 022016, 2014.

[77] R. Dutta, J. Nicolle, A.-M. Giroux, and U. Piomelli, "Evaluation of turbulence models on roughened turbine blades," in *IOP Conf. Series: Earth and Environmental Science*, vol. 49, p. 062007, 2016.

[78] R. J. Volino, W. J. Devenport, and U. Piomelli, "Questions on the effects of roughness and its analysis in non-equilibrium flows," *Journal of Turbulence*, vol. 23, no. 8, pp. 454–466, 2022.

[79] J. Yuan and U. Piomelli, "Numerical simulations of sink-flow boundary layers over rough surfaces," *Phys. Fluids*, vol. 26, pp. 015113–1—015113–28, 2014.

[80] A. Keating, U. Piomelli, K. Bremhorst, and S. Nešić, "Large-eddy simulation of heat transfer downstream of a backward-facing step," *J. Turbul.*, vol. 5, p. N20, 2004.

[81] R. D. Moser and P. Moin, "The effects of curvature in wall-bounded turbulent flows," *J. Fluid Mech.*, vol. 175, pp. 479–510, 1987.

[82] P. S. Jackson, "On the displacement height in the logarithmic velocity profile," *J. Fluid Mech.*, vol. 111, pp. 15–25, 1981.

[83] S. B. Pope, *Turbulent Flows*. Cambridge, U.K.: Cambridge Univ. Press, 2000.

[84] H. M. Nagib and K. A. Chauhan, "Variations of von Kármán coefficient in canonical flows," *Phys. Fluids*, vol. 20, pp. 15180–1–10, 2008.

[85] V. Nikora, K. Koll, I. McEwan, S. McLean, and A. Dittrich, "Velocity distribution in the roughness layer of rough-bed flows," *J. Hydr. Engng*, vol. 130, pp. 1036–1042, 2004.

[86] D. Pokrajac, L. J. Campbell, V. Nikora, and I. Manes, C. adn McEwan, "Quadrant analysis of persistent spatial velocity perturbations over square-bar roughness," *Exp. Fluids*, vol. 42, pp. 413–423, 2007.

[87] J. Yuan and G. J. Brereton, "Structure of turbulent flows on heterogeneous irregular rough surfaces," in *Proceedings of 11th International Symposium of Turbulence and Shear Flow Phenomena (TSFP-11)*, 2019.

[88] M. J. Lee, J. Kim, and P. Moin, "Structure of turbulence at high shear rate," *J. Fluid Mech.*, vol. 216, pp. 561–583, 1990.

[89] T. B. Nickels, "Inner scaling for wall-bounded flows subject to large pressure gradients," *J. Fluid Mech.*, vol. 521, pp. 217–239, 2004.

[90] E. R. van Driest and C. B. Blumer, "Boundary layer transition-freestream turbulence and pressure gradient effects," *AIAA J.*, vol. 1, pp. 1303–1306, 1963.

[91] S. Mangavelli and J. Yuan, "Effects of form-induced velocity in rough-wall turbulent channel flows," *Journal of Turbulence*, vol. 24, no. 1-2, pp. 14–35, 2023.

[92] J. Fröhlich, C. P. Mellen, W. Rodi, L. Temmerman, and M. A. Leschziner, "Highly resolved large-eddy simulation of separated flow in a channel with streamwise periodic constrictions," *J. Fluid Mech.*, vol. 526, pp. 19–66, 2005.

[93] J. H. Ferziger, M. Perić, and R. L. Street, *Computational methods for fluid dynamics*. Berlin: springer, 2002.

[94] J. C. R. Hunt, "A review of the theory of rapidly distorted turbulent flows and its applications," *Fluid Dyn. Trans*, vol. 9, pp. 121–152, 1978.

[95] K. M. Womack, R. J. Volino, C. Meneveau, and M. P. Schultz, "Turbulent boundary layer flow over regularly and irregularly arranged truncated cone surfaces," *J. Fluid Mech.*, vol. 933, p. A38, 2022.

[96] K. Bhaganagar, G. N. Coleman, and J. Kim, "Effect of roughness on pressure fluctuations in a turbulent channel flow," *Phys. Fluids*, vol. 19, pp. 028103–1—4, 2007.

[97] T. Meyers, J. B. Forest, and W. J. Devenport, "The wall-pressure spectrum of high-Reynolds-number turbulent boundary-layer flows over rough surfaces," *J. Fluid Mech.*, no. 768, pp. 261–293, 2015.

[98] Q. Yang and M. Wang, "Boundary-layer noise induced by arrays of roughness elements," *J. Fluid Mech.*, vol. 727, pp. 282–317, 2013.

[99] O. Coceal, A. Dobre, T. G. Thomas, and S. E. Belcher, "Structure of turbulent flow over regular arrays of cubical roughness," *J. Fluid Mech.*, vol. 589, pp. 375–409, 2007.

[100] X. Yang, J. Sadique, R. Mittal, and C. Meneveau, "Exponential roughness layer and analytical model for turbulent boundary layer flow over rectangular-prism roughness elements," *J. Fluid Mech.*, vol. 789, pp. 127–165, 2016.

[101] O. Coceal, T. G. Thomas, and S. E. Belcher, "Spatial variability of flow statistics within

regular building arrays," *Bound.-Lay. Meteorol.*, vol. 125, pp. 537–552, 2007.

[102] K. A. Flack, M. P. Schultz, J. M. Barros, and Y. C. Kim, "Skin-friction behavior in the transitionally-rough regime," *Int. J. Heat Fluid Flow*, vol. 61, pp. 21–30, 2016.

[103] P. Forooghi, A. Stroh, F. Magagnato, S. Jakirlic, and B. Frohnapfel, "Toward a universal roughness correlation," *J. Fluids Eng.*, vol. 139, pp. 121201–1–12, 2017.

[104] Y. Kuwata and Y. Kawaguchi, "Direct numerical simulation of turbulence over systematically varied irregular rough surfaces," *Journal of Fluid Mechanics*, vol. 862, pp. 781–815, 2019.

[105] A. J. Musker, "Universal roughenss functions for naturally-occuring surfaces," *Trans. Can. Soc. Mech. Eng.*, no. 1, pp. 1–6, 1980-1981.

[106] H. Ma, Y. Li, X. Yang, and L. Ye, "Data-driven prediction of the equivalent sand-grain roughness," *Scientific Reports*, vol. 13, no. 1, p. 19108, 2023.

[107] X. Yang, W. Zhang, J. Yuan, and R. F. Kunz, "In search of a universal rough wall model," *J. Fluids Eng.*, vol. to be submitted, 2023.

[108] E. Florens, O. Eiff, and F. Moulin, "Defining the roughness sublayer and its turbulence statistics," *Experiments in fluids*, vol. 54, pp. 1–15, 2013.

[109] D. Chung, L. Chan, M. MacDonald, N. Hutchins, and A. Ooi, "A fast direct numerical simulation method for characterising hydraulic roughness," *J. Fluid Mech.*, 2015.

[110] M. MacDonald, D. Chung, N. Hutchins, L. Chan, A. Ooi, and R. García-Mayoral, "The minimal-span channel for rough-wall turbulent flows," *J. Fluid Mech.*, vol. 816, pp. 5–42, 2017.

[111] A. Busse and T. O. Jelly, "Influence of surface anisotropy on turbulent flow over irregular roughness," *Flow, Turbulence and Combustion*, vol. 104, pp. 331–354, 2020.

[112] W. Wu, U. Piomelli, and J. Yuan, "Turbulence statistics in rotating channel flows with rough walls," *Int. J. Heat Fluid Flow*, vol. 80, pp. 108467–1–13, 2019.

[113] J. Hong, J. Katz, and M. P. Schultz, "Near-wall turbulence statistics and flow structures over three-dimensional roughness in a turbulent channel flow," *J. Fluid Mech.*, vol. 667, pp. 1–37, 2011.

[114] J. M. Barros, M. P. Schultz, and K. A. Flack, "Measurements of skin-friction of systematically generated surface roughness," *International Journal of Heat and Fluid Flow*, vol. 72, pp. 1–7, 2018.

[115] T. Medjnoun, C. Vanderwel, and B. Ganapathisubramani, "Characteristics of turbulent boundary layers over smooth surfaces with spanwise heterogeneities," *Journal of Fluid Mechanics*, vol. 838, pp. 516–543, 2018.

[116] T. Medjnoun, E. Rodriguez-Lopez, M. Ferreira, T. Griffiths, J. Meyers, and B. Ganapathisubramani, "Turbulent boundary-layer flow over regular multiscale roughness," *Journal of Fluid Mechanics*, vol. 917, p. A1, 2021.
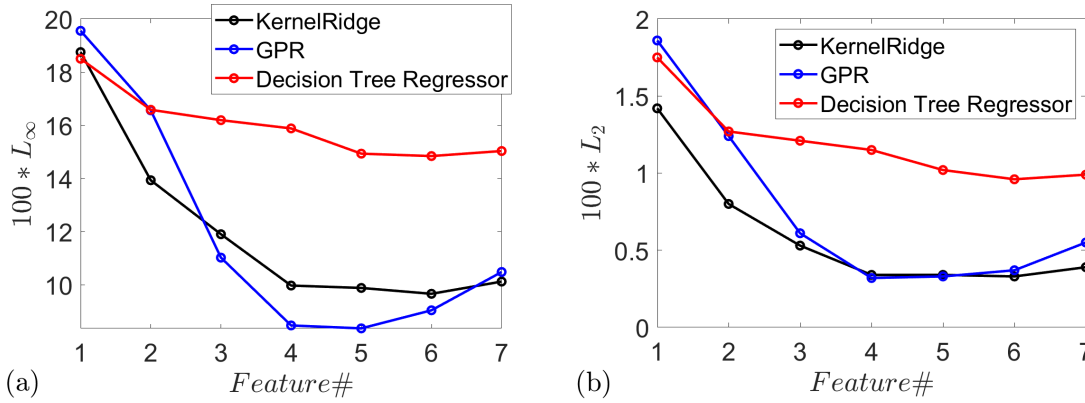
A.1 Comparison between different ML methods

Figure A.1 Comparison of different ML methods in $U(y)$ prediction with different numbers of roughness features used as inputs, based on (a) L_∞ and (b) L_2.

Figure A.1 compares the performances of different machine learning techniques on $U(y)$ prediction, based on the L_∞ and L_2 values (quantified as the maximum value among all cases and averaged throughout all $N = 1300$ runs). Different numbers of features used for training are evaluated, similar to the procedure used for Figure 4.7(a). Two other regression methods: Kernel Ridge (KR) and Decision Tree Regressor (DTR) are compared with GPR used herein. Both GPR and KR (with third-degree polynomial) give overall similar predictions, with the error norms decreasing with increasing number of features, reaching a minima at 4 or 5 features. This consistency across different methods provides confidence in the findings in Chapter 4. However, DTR gives significantly higher errors. GPR is finally selected as the method used in Chapter 4, while another method may also be used.

A.2 Predictions with other sizes of test datasets

In the $U(y)$ prediction in Chapter 4, 15% of the datasets are used as test data. To analyze whether a change of this percentage affects the GPR prediction, the errors of the optimal GPR predictions obtained with larger percentages (up to 50%) of data used as test data are shown in Figure A.2(a). It is shown that L_∞ and L_2 error norms (the maximum values across all flow cases) both increase sharply when more than 24% of the data are used as test data. This is due to the lack of sufficient representation of different roughness types in the training set as a consequence of limited data availability.

To provide more details, Figure A.2(b) shows that the percentages of the total datasets with relatively high errors (i.e. $L_\infty > 0.1$ and $L_2 > 0.005$) increase with the size of the test datasets. It is therefore concluded that, for the present available data, the applicability of the model is up to test data being up to 24% of total datasets.
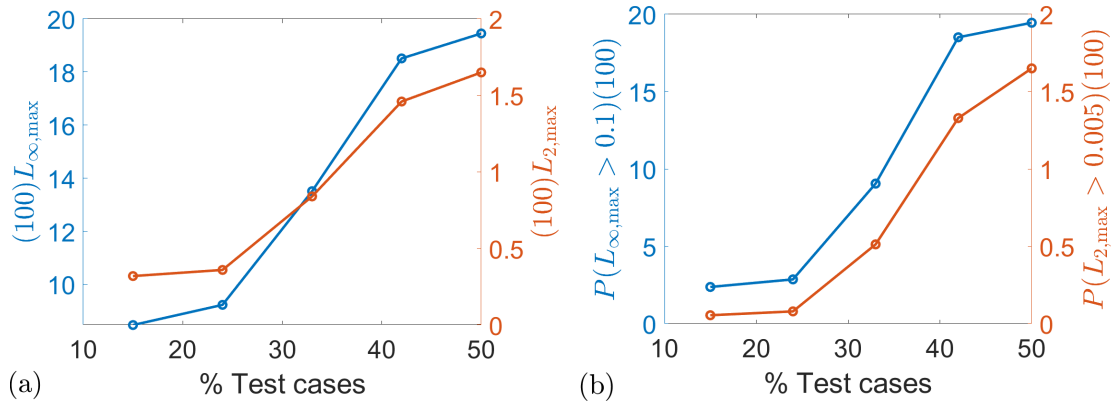
Figure A.2 Variation of percentage errors (a) and percentage of cases with errors larger than a threshold (b) with the test-cases (as a percentage of all datasets).